Dual-Band Beam Scanning Antenna for the Satellite Ka-Band Based on Rotary Transmit Arrays

João Leandro Câmara Serra

Thesis to obtain the Master of Science Degree in

Electrical and Computer Engineering

Supervisors: Prof. Carlos António Cardoso Fernandes

Prof. Sérgio de Almeida Matos

Examination Committee

Chairperson: Prof. José Eduardo Charters Ribeiro da Cunha Sanguino

Supervisor: Prof. Carlos António Cardoso Fernandes

Members of the Committee: Prof. Rafael Ferreira da Silva Caldeirinha

January 2021

Declaration:

I declare that this document is an original work of my own authorship and that it fulfils all the requirements of the Code of Conduct and Good Practices of the Universidade de Lisboa.

Acknowledgements

First, I wish to thank my supervisors, Prof. Carlos Fernandes and Prof. Sérgio Matos, for their valuable help, guidance and time, without which this thesis work would have never been done.

To Mr. João Felício, I am grateful for his experimental advices throughout the project and help in performing the necessary measurements with the prototype.

Mr. Carlos Brito, as always, was a fundamental part of this project for manufacturing the prototype to whom I am much grateful.

My thanks are due to Mr. Jorge Farinha who helped as well during the manufacturing process.

I would like to thank Instituto de Telecomunicacões (IT), UIDB/50008/2020, and project ADAM3D: PTDC/EEITEL/30323/2017, for financing all the needed material used in this thesis, and for the usage of IT laboratories, software and hardware equipment.

I thank God for my family, my teachers and my friends who made this work possible.

Resumo

O aumento do número de aplicações para antenas com varrimento de feixe tem motivado o desenho de soluções compactas, leves e baratas com ganho elevado. Neste trabalho é proposta uma antena dual-band insensível a polarização com feixe móvel usando um sistema rotativo (configuração de Risley Prism) de dois transmit arrays (TAs) para terminais terrestres pequenos em ligações bidirecionais móveis Ka-band.

A combinação do conceito de Risley Prism com TAs tem sido explorada como uma solução eficaz para alcançar ganhos elevados e grandes amplitudes de varrimento de feixe. Em trabalhos anteriores, as antenas Risley Prism TA operam apenas numa banda de frequências. Neste trabalho é apresentado pela primeira vez uma implementação dual-band deste conceito para duas bandas distintas (20/30 GHz) e uma nova abordagem à implementação do conceito de Risley Prism é proposta para melhorar o desempenho da antena.

Um conjunto de 29 células unitárias dual-band phase-delay finas é desenhado com um coeficiente de transmissão melhor que $-1\ dB$ e capaz de representar todas as combinações de fase nas duas bandas. As lentes têm diâmetro $148\ mm$, espessura $3.233\ mm$ e são separadas por uma camada de ar de $5\ mm$ de espessura. O ganho simulado é $25.6\ dBi$ para $f_1 \approx 20\ GHz$ e $27.7\ dBi$ para $f_2 \approx 30\ GHz$, um SLL de $-14.4\ dB$ nas duas bandas para $\theta_{max} \approx 0°$. A amplitude de varrimento é $[-50°, 50°]$ com uma atenuação de varrimento melhor que $-3\ dB$ e $SLL < -10\ dB$. Um protótipo está a ser fabricado e será testado.

Palavras-Chave: Transmit Array, K/Ka-band, Dual-band, Varrimento de Feixe, Risley Prism

Abstract

The increasing interest in applications involving beam steering antennas has motivated the design of compact, low-profile, lightweight, and low-cost solutions presenting high gain. A polarization-insensitive dual-band beam scanning antenna using a rotary system (Risley Prism configuration) with two transmit arrays (TAs) is proposed in this thesis work for small ground terminals in mobile broadband access in bi-directional Ka-band satellite applications.

The combination of the Risley prism concept with TAs is being widely investigated as a cost-effective antenna solution to achieve high gain and wide beam scanning at microwave and millimeter waves. In previous designs the Risley Prism TA antenna operates at single frequency band. This work presents for the first time a dual-band implementation of this concept for two widely separated bands (20/30 GHz) and proposed a novel approach to implement the Risley Prism concept to improve the scanning performance.

A set of 29 thin dual-band phase-delay unit cells is developed with transmission coefficient better than $-1\ dB$ at both bands, that covers all the required 20 and 30 GHz phase combination. The TAs have a diameter $148\ mm$, thickness $3.233\ mm$ and air gap separation of $d = 5\ mm$. Full-wave simulated gain is $25.6\ dBi$ gain at $f_1 \approx 20\ GHz$ and a $27.7\ dBi$ at $f_2 \approx 30\ GHz$ and $SLL = -14.4\ dB$ at both bands for $\theta_{max} \approx 0°$. The scanning range is $[-50°, 50°]$ with a scan loss lower than $-3\ dB$ and $SLL < -10\ dB$. A prototype is being built and measured.

Keywords: Transmit Array, K/Ka-band, Dual-band, Beam Scanning, Risley Prism

Table of Contents

List of Figures

List of Tables

List of Abbreviations

HAP – High Altitude Platforms

HTS – High Throughput Satellites

LHCP – Left-Hand Circular Polarization

PD – Phase-delay

PR – Phase-rotation

PSS – Phase Shifting Surface

PO/GO – Physical Optics/Geometrical Optics

RHCP – Right-Hand Circular Polarization

RLSA – Radial Line Slot Antenna

RPP – Reduced Phase-Pair

SOTM – Satellite-on-the-move

TA – Transmit array

TRP – Total radiated power

List of Notations

a_i – Intermediate metal square ring dimension in layer i

c – Light speed in vacuum

d – Air gap thickness

D_{max} – Antenna directivity along the main lobe direction

$\boldsymbol{E}$ – Electric field

$\boldsymbol{E_a}$ – Tangential electric field component

e – Antenna efficiency

e_a – Antenna aperture efficiency

$\boldsymbol{F}$ – Electric radiation vector

$\boldsymbol{F_m}$ – Magnetic radiation vector

F_1 – Real focus distance from TA_1

F_2 – Virtual focus distance from TA_1

G – Power Gain

$\boldsymbol{H}$ – Magnetic field

$\boldsymbol{H_a}$ – Tangential electric field component

h – Unit cell dielectric layer thickness

h_i – Unit cell metal layer thickness

k_0 – Free-space wavenumber

$\boldsymbol{J_{ms}}$ – Equivalent electric surface current

$\boldsymbol{J_s}$ – Equivalent electric surface current

l_i – Interior metal square ring dimension in layer i

P – Unit cell width

S – Scattering matrix

SLL – Sidelobe Level

T_f^i – Transmission amplitude of cell i at frequency f

t – Unit cell total thickness

U – Radiation intensity

$w_{a,i}$ – Exterior metal square ring width in layer i

$w_{in,i}$ – Interior metal square ring width in layer i

$w_{out,i}$ – Intermediate metal square ring width in layer i

α_0 – Offset elevation angle

Γ_f^i – Reflection coefficient of cell i at frequency f

δ – Material loss angle

$\varepsilon_{eq,f}^i$ – Equivalent relative electric permittivity of cell i at frequency f

ε_r – Material relative electric permittivity

ε_0 – Vacuum electric permittivity

Θ – Maximum scanning elevation angle

θ – Elevation scanning angle

θ_{in} – Unit cell incidence angle relative to the normal

θ_{max} – Main lobe elevation angle

θ_{RP} – Theoretical elevation angle for a Risley Prism

λ_0 – Free-space wavelength

$\mu_{eq,f}^i$ – Equivalent relative magnetic permeability of cell i at frequency f

μ_r – Material relative magnetic permeability

μ_0 – Vacuum magnetic permeability

ξ – Differential rotation angle

σ – Feed beamwidth

φ – Azimuth scanning angle

φ_{max} – Main lobe azimuth angle

ϕ – Mean rotation angle

ϕ_f^i – Phase delay of cell i at frequency f

ϕ_f^{ref} – Phase delay reference at frequency f

$\phi_{in,i}$ – Phase delay distribution of the incident wave over TA_i

$\phi_{lens,i}$ – Phase delay distribution of TA_i

$\phi_{out,i}$ – Phase delay distribution of the wave radiated by TA_i

ψ_i – Rotation angle of the phase progression axis of TA_i relative to the $\hat{\boldsymbol{x}}$ axis

1 Introduction

1.1 Motivation and Objectives

In the last decade, there has been an increasing interest regarding applications involving beam scanning antennas: satellite-on-the-move (SOTM), point-to-multipoint, tracking, etc. In satellite communications, the circular polarization is the most common choice because it is less influenced by multipath fading effects, polarization mismatch due to the Faraday's Effect and the ground terminal mobility. The up-link and down-link use orthogonal polarizations and different frequency bands to reduce the interference between the transmitted and received signals.

Beam scanning antennas must present a high gain to compensate the Path Loss that is critical for long distance millimeter wave communications simultaneously with a large elevation scanning range ($\theta_{max} \in [0°, 50°]$) and a complete azimuth scanning ($\varphi_{max} \in [0°, 360°]$) with $Scan\ Loss > -3\ dB$ and $SLL < -10\ dB$.

The market of small ground terminals for mobile broadband access applications is expected to grow with the next generation of High Throughput Satellites (HTS) and High Altitude Platforms (HAP), so the challenge is to satisfy the previous requirements using a compact, low-profile ($F/D < 1$), lightweight and low-cost solution that is appropriate for mass market production.

In this thesis, it is proposed a polarization-insensitive mechanical beam steering antenna concept for ground mobile terminals on bi-directional Ka-band satellite links (Rx: $20\ GHz$, Tx: $30\ GHz$) using a rotary system with two circular transmit arrays based on the Risley Prism concept using thin dual-band phase-delay cells. Unlike other mechanical steering solutions, rotary systems do not vary its operation volume while steering the main lobe without requiring the complexity of electronic solutions. This antenna is the first dual-band and polarization-insensitive beam scanning solution based on rotary transmit arrays in the literature and the Risley Prism concept is implemented using a new approach.

1.2 State of the Art

Beam scanning antennas can be divided into three groups according to their steering mechanism nature: electronic, mechanical or hybrid.

Electronic steering solutions [1-5] are based on phased arrays with a feeding system that is electronically controlled. Typically, they are characterised by compact and low-profile antennas with a very fast beam scanning, but they also have a complex feeding network which increases the antenna cost and deteriorates the RF efficiency.

Mechanical steering solutions rely on mechanical movements from the radiating aperture or from the feed to vary the propagation direction of the transmitted wave [6-10]. Usually, they allow for a wider beam scanning range and they are very cost-effective because they only use one single feed. However, they tend to be bulkier which can be a problem in some scenarios.

Hybrid solutions [11] are a compromise between these two: one of the scanning angles is mechanically steered while the other one is controlled by an electronic mechanism.

There is no optimal steering mechanism because each case has its own particularities, and the best solution corresponds to a trade-off between the antenna complexity, size, performance, and cost. Since our solution belongs to the second group, that will be the one focused in this Section. There is a vast set of mechanical solutions using reflector antennas [12-14], 3D lenses inspired in dielectric wedges [10, 15, 16] or transmit arrays [6, 7, 17].

Reflector antennas, such as parabolic antennas or reflect arrays, reflect the incident wave while altering its wavefront. This reflection mechanism has one disadvantage: the feeding antenna has to be deviated to prevent beam blockage.

Dielectric wedges, due to their wedge geometry, allow to shift the incident wave's propagation direction according to Snell's Law. Consequently, if the wedge is rotated around the normal axis, it is possible to control the azimuth angle with a constant elevation angle defined by its thickness and relative electric permittivity. These dielectric wedges can be used in pairs to work as a Risley Prism. The combination of the independent rotation of two wedges allows not only the complete azimuth coverage but also elevation scanning. However, this is not a very common mechanism because it presents a high reflection coefficient, and it is a relatively bulky solution.

A transmit array (TA) is a thin flat Phase Shifting Surface (PSS) lens discretized into unit cells. Inspired by reflect arrays, transmit arrays receive an incident wave and manipulate the propagation characteristics of the transmitted wave using predefined in-plane wave vectors, preventing any feed blockage. PSS technology is a low-cost, compact and low-weight alternative to dielectric wedges.

The mechanical steering mechanisms of solutions involving TAs typically involve in-plane translations and/or rotations around the normal axis to reduce the antenna height. In-plane translation mechanisms are simpler because they only require one lens [6, 9] but they are associated with non-linear phase shifting errors that originate aberrations in the radiation pattern. The in-plane translation can be applied to the lens, which requires extra available space, or the feed, twisting the RF cable and damaging it in the long run. On the other hand, rotary solutions use two [7] or more [8] lenses which introduce losses, but they require less available space to operate.

Similar to a LEGO construction, the unit cells are the building blocks of a TA and they usually consist in metallic components (capacitive patches, inductive rings, etc) separated by dielectric layers. Each one of the cells introduces a different phase shift that determines the cell's position in the lens. There are two families of passive cells that use different working principles to control: phase-delay (PD) cells [7, 9] and phase-rotation (PR) cells [17-19]. While two distinct PD cells have metallic components with

slightly different dimensions presenting different effective parameters, two PR cells have the exact same components but they are rotated. Each family has advantages and disadvantages regarding the other one that should be considered when designing a TA for a specific problem [20]. PD cells tend to use more layers, making them bulkier, but they are insensitive to the polarization. PR cells usually are thinner but they only work for a specific circular polarization sense.

Satellite communication links are bi-directional, and each link uses a separate frequency band to minimize the inter-link interference. Additionally, in some applications like SOTM, orthogonal circular polarizations are required between up-link and down-link, with the possibility of toggling the combination. One option is to have two distinct apertures working at different frequency bands, but this solution requires more space and introduces additional complexity to the problem. Another alternative is to use TA with interleaved single-band cells [25]. Although this is the simplest option, it has some limitations regarding the antenna efficiency. The best solution is to use dual-band apertures that can operate simultaneously on two distinct bands. These solutions require dual-band PD unit cells which can have different designs [6, 8, 21-23]. Dual-band PR cells are not common when designing beam scanning solutions involving transmit arrays due to their working principle, but they can be used in other applications such as polarization converters [24].

In the literature, there are already solutions performing beam steering using dual-band PD transmit arrays [6, 23] and single-band Risley Prism-like rotary systems [7, 8] but the two were never combined before, as far as we know. In [8], a solution is proposed using 3 TAs (one for collimation and two rotating lenses with tilting effects) and dual-band PD cells, however the gain is considerably low ($e_a \approx 25\%$ at $f = 8\ GHz$ and $e_a \approx 15\%$ at $f = 14\ GHz$) and it is not truly a dual-band Risley Prism-like system because the main lobe direction is not the same in both bands.

1.3 Work Highlights

The design of a system with dual-band TAs based on the Risley Prism concept had three steps. First, a Physical Optics/Geometrical Optics (PO/GO) analysis to study and determine the main geometrical parameters with ideal phase distributions. Then, a full-wave analysis in the Frequency Domain to design a set of 29 thin dual-band PD cells with high amplitude transmission ($|S_{21}| > -1\ dB$), small phase error and small phase discretization step ($\Delta\phi < 30°$ at $f_1 = 20\ GHz$ and $\Delta\phi < 45°$ at $f_2 = 30\ GHz$). This process is particularly difficult when designing dual-band cells because these requirements must be satisfied simultaneously in two distinct bands. Finally, a full-wave analysis in the Time Domain to compare different Risley Prism implementations using the cells from the previous step, to evaluate the respective scanning performances and to optimise parameters. Due to the complexity of these simulations, we were forced to resort to alternative methods to improve the time-efficiency of the simulations: an equivalent feed source instead of a Horn antenna to reduce the simulation volume and an equivalent dielectric description of the unit cells [26] before using the real lenses. The full-wave

analyses were performed using CST software [27] and the PO/GO analysis was done using the KH3D_near program developed in house [28].

A prototype of the rotary system is being built and measured using a radio-frequency anechoic chamber to validate the simulation results.

The antenna proposed in this work is the first dual-band polarization-insensitive beam scanning solution using a rotary system of transmit arrays. It is an extension of the Risley Prism concept, that allows pointing the beam at the same direction at two well-separated bands, like the satellite Ka-bands. A new approach is proposed for the Risley Prism implementation that ensures more stable radiation patterns than traditional designs. Our antenna presents high gain at both frequency bands ($G = 25.6\ dBi$ at $f_1 = 20.3\ GHz$ and $G = 27.7\ dBi$ at $29.9\ GHz$) and it guarantees a scanning range of $[-50°, 50°]$ with a scan loss smaller than $-3\ dB$ and a Sidelobe Level better than $-10\ dB$.

This thesis is organized as follows. The geometry of our solution and a brief description of the theoretical background supporting PSS technology and the Risley Prism concept is presented in Chapter 2, as well as an introduction to the general aspects that characterize dual-band cells. Chapter 3 addresses the design and performance of the unit cells, as well as a comparison between the simulation results of the conventional implementation and the new one proposed in this work. Also, it is provided a general description of the experimental setup for the prototype manufacturing and testing. Finally, Chapter 4 has the main conclusions and a small discussion about open questions and future work related to this work.

2 Formulation and Methods

2.1 PO/GO Formulation

The Field Equivalence Principle [29] states that the problem of determining the electric and magnetic fields, $\boldsymbol{E}(\boldsymbol{r})$ and $\boldsymbol{H}(\boldsymbol{r})$, at some far observation point $\boldsymbol{r}$ outside a volume V radiated by sources inside V is equivalent to the one where the electromagnetic fields are radiated by electric and magnetic surface currents, $\boldsymbol{J_s}$ and $\boldsymbol{J_{ms}}$, over the closed outer surface ∂V of that volume. These equivalent currents are defined as

$$\begin{aligned} \mathbf{J}_s &= \hat{\boldsymbol{n}} \times \boldsymbol{H_a} \\ \boldsymbol{J_{ms}} &= -\hat{\boldsymbol{n}} \times \boldsymbol{E_a} \end{aligned} \tag{1}$$

where $\boldsymbol{E_a}$ and $\boldsymbol{H_a}$ are the tangential electric and magnetic fields components over ∂V and $\hat{n}$ is the unit vector normal to the outer surface pointing away from the sources. It is important to mention that this magnetic surface current is fictitious: it has no physical meaning because magnetic monopoles do not exist.

In the equivalent formulation, the far-field radiation is given by (2).

$$\begin{aligned} \boldsymbol{E}(r,\theta,\varphi) &= -jk\frac{e^{-jkr}}{4\pi r}\hat{\boldsymbol{r}} \times [\eta \boldsymbol{F}(\theta,\varphi) \times \hat{\boldsymbol{r}} - \boldsymbol{F_m}(\theta,\varphi)] \\ \boldsymbol{H}(r,\theta,\varphi) &= \frac{1}{\eta}\hat{\boldsymbol{r}} \times \boldsymbol{E} = -\frac{jk}{\eta}\frac{e^{-jkr}}{4\pi r}\hat{\boldsymbol{r}} \times [\eta \boldsymbol{F}(\theta,\varphi) - \boldsymbol{F_m}(\theta,\varphi) \times \hat{\boldsymbol{r}}] \end{aligned} \tag{2}$$

where θ and ϕ are the elevation and azimuth angles and $\boldsymbol{F}$ and $\boldsymbol{F_m}$ are the electric and magnetic radiation vectors that determine the radiation pattern. They are defined as the 2-D Fourier Transforms of the Equivalent Currents:

$$\begin{aligned} \boldsymbol{F}(\theta,\varphi) &= \int_{\partial V} \boldsymbol{J_s}(\boldsymbol{r'})\, e^{j\boldsymbol{k}(\theta,\varphi)\cdot\boldsymbol{r'}} dS' \\ \boldsymbol{F_m}(\theta,\varphi) &= \int_{\partial V} \boldsymbol{J_{ms}}(\boldsymbol{r'})\, e^{j\boldsymbol{k}(\theta,\varphi)\cdot\boldsymbol{r'}} dS' \end{aligned} \tag{3}$$

with $\boldsymbol{k}(\theta,\varphi).\boldsymbol{r}' = kx'\sin\theta\cos\varphi + ky'\sin\theta\sin\varphi$ for a planar aperture orthogonal to $\hat{\boldsymbol{z}}$.

This Principle is particularly useful when dealing with radiating apertures and it is the basis for the working principle of a transmit array (TA): if the far-field radiation is defined solely by the tangential fields over a closed surface ∂V surrounding the field sources inside V, then it is possible to design a certain radiation pattern using any radiation feed as long as it is imposed externally the corresponding Equivalent Currents over that surface.

If the outer surface of a TA belongs to ∂V, we can neglect the currents outside of it because the incident radiation is focused over the lens' inner surface. In that case, for a very thin and lossless transmit array, the transmission coefficient is $S_{21}(x,y) = e^{-j\phi_{lens}(x,y)}$ and we get

$$\begin{aligned} \boldsymbol{E_{out}}(x,y) &= \boldsymbol{E_{in}}(x,y)\cdot S_{21}(x,y) \Leftrightarrow \\ \Leftrightarrow |\boldsymbol{E_{out}}|e^{-j\phi_{out}} &= |\boldsymbol{E_{in}}|e^{-j(\phi_{in}+\phi_{lens})} \Leftrightarrow \\ \Leftrightarrow \phi_{out}(x,y) &= \phi_{in}(x,y) + \phi_{lens}(x,y) \end{aligned} \tag{4}$$

where $\phi_{lens}(x,y)$ is the lens phase delay, which is symmetric to the transmission phase (i.e. phase of the transmission coefficient). Note also, that we are using the convention $\boldsymbol{E}(\boldsymbol{r},t) = E_A(\boldsymbol{r})e^{j(\omega t - \boldsymbol{k}\cdot\boldsymbol{r})}$.

By defining the lens phase delay distribution as $\phi_{lens}(x,y) = \phi_{out}(x,y) - \phi_{in}(x,y)$, we obtain a simple and elegant tool for wavefront manipulation. Each one of the lenses introduces a different effect over the incident wave and thus we need two different phase distribution laws: $\phi_{lens,1}(x,y)$ for TA_1 and $\phi_{lens,2}(x,y)$ for TA_2.

2.2 Geometry Description

The mechanical beam steering mechanism of the proposed solution consists of two rotatable Phase Shifting Surfaces (PSS) working as transmit arrays, TA_1 and TA_2, with some external feed source, like a Patch Antenna or a Horn Antenna, as it is shown in Figure 1. The origin of the (x,y,z) coordinate system is the feed phase center.

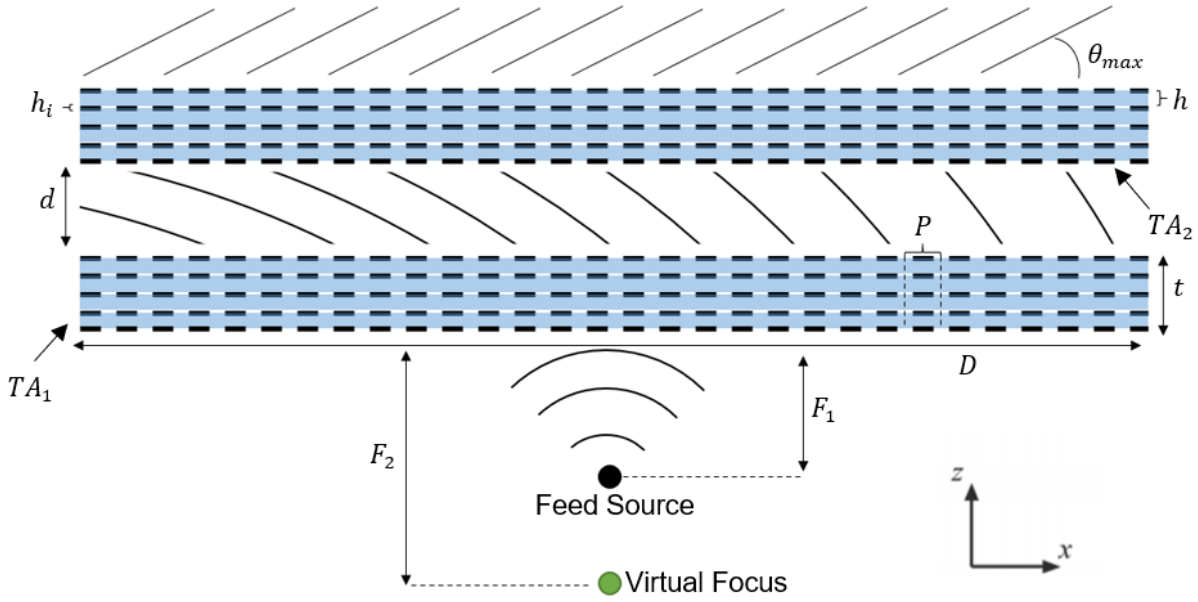

Figure 1 - Mechanical beam steering solution scheme: spherical wave feed source and two rotatable PSS lenses, TA_1 and TA_2. Each lens has 5 layers of metallic insertions (black) separated by four dielectric layers (blue). It is also represented the qualitative wavefront propagation (black lines).

These transmit arrays have a concentric circular geometry with diameter D and thickness t. The lenses are separated by an air gap with thickness d between them and they can rotate independently from each other around the vertical axis, $\hat{\boldsymbol{z}}$. This introduces two degrees of freedom: the rotation angles of TA_1 and TA_2 relative to the $\hat{\boldsymbol{x}}$ axis, ψ_1 and ψ_2, respectively (see Figure 2).

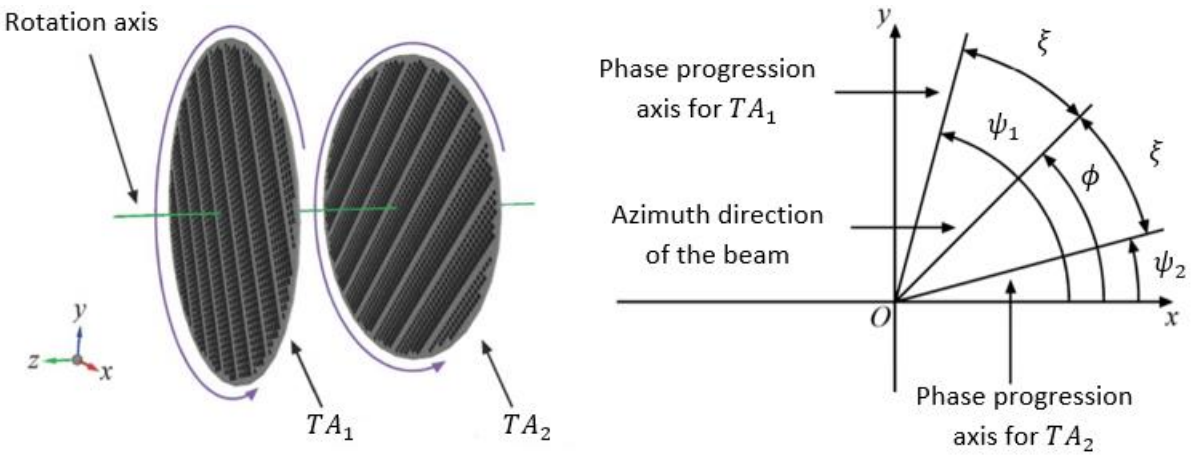

Figure 2 - TA rotary mechanism seen from perspective (left) and rotation coordinate system seen from above (right): ψ_1 and ψ_2 correspond to the progression axes of TA_1 and TA_2, respectively. This figure was taken from [7]

The working principle of the Risley Prism concept can be divided in three steps: i) beam collimation (the incident wave is usually a spherical wave); ii) first beam elevation angle offset α_1 for a given azimuth

position ψ_1; iii) second beam elevation offset α_2 along a different azimuth position ψ_2. To perform beam scanning it is always necessary to ensure at least two degrees of freedom, because an arbitrary direction is defined by two parameters (the elevation angle θ and the azimuth angle φ). The mean rotation angle, $\phi = \frac{\psi_1+\psi_2}{2}$, controls the azimuth scanning and the differential rotation angle, $\xi = \frac{\psi_1-\psi_2}{2}$, defines the elevation angle.

For a generic configuration of first and second beam elevation angle offsets α_1 and α_2 and first and second azimuth positions ψ_1 and ψ_2, the phase distribution over the radiating surface of the antenna is

$$\phi_{out}(x,y) = k_0([\sin\alpha_1 \cos\psi_1 + \sin\alpha_2 \cos\psi_2]x + [\sin\alpha_1 \sin\psi_1 + \sin\alpha_2 \sin\psi_2]y) \tag{5}$$

Considering $\alpha_1 = \alpha_0 + \delta$, $\alpha_2 = \alpha_0 - \delta$, $\psi_1 = \phi + \xi$ and $\psi_2 = \phi - \xi$, then

$$\phi_{out}(x,y) = k_0(\sin\theta_1\,[\cos\phi\, x + \sin\phi\, y] + \sin\theta_2\,[\cos(-\phi)\, x + \sin(-\phi)\, y]) \tag{6}$$

where

$$\begin{aligned} \theta_1(\xi,\delta) &= |\arcsin(2\sin\alpha_0 \cos\delta \cos\xi)| \\ \theta_2(\xi,\delta) &= |\arcsin(2\cos\alpha_0 \sin\delta \sin\xi)| \end{aligned} \tag{7}$$

Phase distribution (7) describes the superposition of two plane waves propagating along the directions $(\theta = \theta_1, \varphi = \phi)$ and $(\theta = \theta_2, \varphi = -\phi)$. It is expected that the gain of each plane wave depends on the value of δ, such that the amplitude of the second wave decreases for smaller values of δ. For a single beam pointing antenna, $\delta = 0$,

$$\phi_{out}(x,y) = k_0(\sin\theta_{RP}\,[\cos\phi\, x + \sin\phi\, y]) \tag{8}$$

with the output elevation angle θ_{RP} defined as

$$\theta_{RP}(\xi) = |\arcsin(2\sin\alpha_0 \cos\xi)| \tag{9}$$

The offset angle α_0 must be carefully chosen because it defines the relation between the differential rotation ξ and the elevation angle θ. Figure 4 shows this relation for different offset angles.

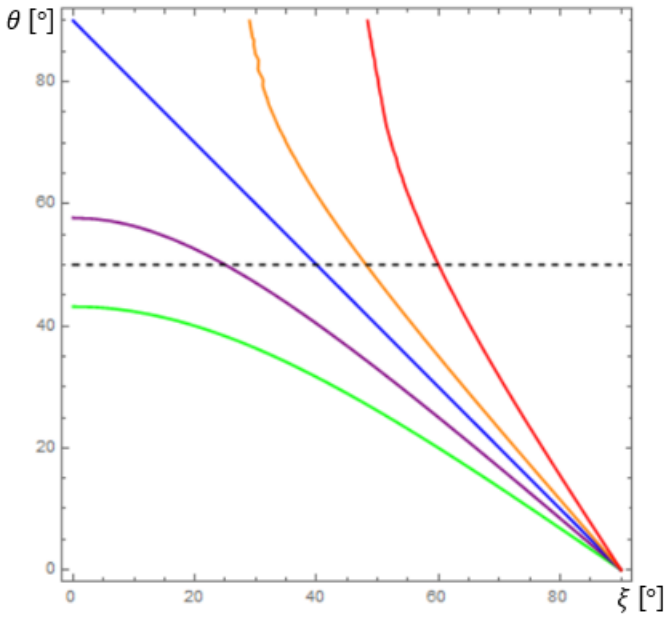

Figure 3 - Elevation angle θ as a function of ξ for different values of α_0: $20°$ (green), $25°$ (purple), $30°$ (blue), $35°$ (orange) and $40°$ (red). The limit $\theta = 50°$ is marked with a dashed black line

Figure 4 shows that the elevation angle decreases with ξ. It is also possible to define two different regimes:

If $\alpha_0 < 30°$, the elevation scanning range is limited to $[0, \arcsin(2\sin\alpha_0)]$. Therefore, the offset angle should be larger than

$$\alpha_{min} = \left|\arcsin\left(\frac{\sin\Theta}{2}\right)\right| \tag{10}$$

where Θ is the maximum scanning elevation angle.

If $\alpha_0 > 30°$, there is no limitation regarding the elevation scanning range but it may affect the Directivity performance. The Directivity of an aperture with surface area A and aperture efficiency e_a radiating a wave with an elevation angle θ for a wavelength λ is

$$D_{max} = \frac{4\pi A}{\lambda^2} e_a \cos\alpha_0 \tag{11}$$

where the aperture efficiency is defined as

$$e_a = \frac{\left| \iint_A \boldsymbol{E_a}(\boldsymbol{r'}) dS' \right|^2}{\iint_A |\boldsymbol{E_a}(\boldsymbol{r'})|^2 dS'} \tag{12}$$

Each lens will radiate a main lobe with elevation angle α_0 so the Directivity is expected to decrease for higher values of α_0. The best choice would be the smallest offset elevation angle that satisfies both the scanning and Directivity requirements. Although theoretically $\Theta = 90°$, the real value is $\Theta = 50°$ because the scan loss becomes too high ($Scan\ Loss < -3\ dB$). Therefore, the best offset elevation angle value is $\alpha_0 = 25°$.

This Risley Prism concept can be implemented with TAs using different approaches as it will be presented in this section. The greatest challenge is to accomplish this behaviour simultaneously in two well-separated frequency bands, while ensuring the same pointing direction in the two bands.

2.2.1 Conventional Implementation

In previous works with rotating systems, the conventional approach consists of implementing steps i) and ii) by one single offset Fresnel TA and step iii) by one linear phase delay correction [7]. Although less efficient, this can also be done using three lenses, one for implementing each step [8]. The following deduction uses the two lenses method, and it describes the working principle proposed in [7].

The incident field is assumed to be a gaussian illumination from a spherical wave feed with a focal distance F_1 from the first lens. TA_1 collimates the incident wave and tilts the output plane wave with an offset elevation angle α_0 along the direction defined by the rotation angle ψ_1. Apart from an additive term that is spatially constant, the incident wave's phase distribution is

$$\phi_{in,1}(x, y) = k_o \sqrt{x^2 + y^2 + F_1^2} \tag{13}$$

and the phase distribution of the desired transmitted wave with a progression axis along the $\hat{\boldsymbol{x}}$ direction ($\psi_1 = 0°$) and an offset elevation angle α_0 is

$$\phi_{out,1}(x, y) = k_0 \sin \alpha_0\, x \tag{14}$$

For a rotation angle ψ_1, the progression axis is $\widehat{\boldsymbol{x}}_{\mathbf{1}} = \cos\psi_1\,\widehat{\boldsymbol{x}} + \sin\psi_2\,\widehat{\boldsymbol{y}}$ and the transmitted plane wave is described by (15).

$$\phi_{out,1}(x,y) = k_0 \sin\alpha_0\,(\cos\psi_1\,x + \sin\psi_1\,y) \tag{15}$$

Thus, the phase delay distribution of TA_1 is defined as

$$\begin{gathered}\phi_{lens,1}(x,y) = \phi_{out,1} - \phi_{in,1} = \\ = k_0\left[-\sqrt{x^2+y^2+F_1^2} + \sin\alpha_0\,(\cos\psi_1\,x + \sin\psi_1\,y)\right] + k_0F_1\end{gathered} \tag{16}$$

Note that the wavefront is uniquely defined apart from a spatially constant term, so k_0F_1 is a phase zeroing term that does not affect the lens phase distribution and enforces that the lens has no phase delay in its center, that is, $\phi_{lens,1}(0,0) = 0$.

The second lens, TA_2, tilts once again the plane wave transmitted from TA_1 by an offset elevation angle α_0 according to the rotation angle ψ_2. Therefore, its phase delay distribution $\phi_{lens,2}$ is described by (17).

$$\phi_{lens,2}(x,y) = \phi_{out,2} - \phi_{in,2} = k_0 \sin\alpha_0\,(\cos\psi_2\,x + \sin\psi_2\,y) \tag{17}$$

Note that $\phi_{in,2}(x,y,z) = \phi_{out,1}(x,y,z+d)$.

The phase distribution of the wave emitted from TA_2 can be rewritten as (18) and corresponds to the Risley Prism concept, as expected.

$$\begin{gathered}\phi_{out}(x,y) = \phi_{out,2} = \phi_{in,2} + \phi_{lens,2} = \\ = k_0(\sin\theta_{RP}\,[\cos\phi\,x + \sin\phi\,y])\end{gathered} \tag{18}$$

2.2.2 New Proposed Implementation

A novel approach to define the phase correction of the two TAs that compose the antenna is presented: the implementation of the collimating effect is distributed by the two lenses so that the combination emulates the required overall phase compensation. The main difference is that TA_1 no longer radiates a plane wave, which has an impact over the antenna performance especially in terms of SLL, as shown in the next chapter.

Once again, the incident field is assumed to be a gaussian illumination from a spherical wave feed with a focal distance F_1 from the first lens. Now, TA_1 generates a virtual focus F_2, increasing the feed's Directivity, and tilts the output spherical wave with an offset elevation angle α_0 along the direction defined by the rotation angle ψ_1. The incident wave's phase distribution is still (13), but the phase distribution of the desired transmitted wave with a progression axis along the $\hat{\boldsymbol{x}}$ direction ($\psi_1 = 0°$) and an offset elevation angle α_0 is

$$\phi_{out,1}(x,y) = k_0\left[\sqrt{x^2+y^2+F_2^2} + \sin\alpha_0\, x\right] \tag{19}$$

For a rotation angle ψ_1, the progression axis is $\hat{\boldsymbol{x}}_{\boldsymbol{1}} = \cos\psi_1\,\hat{\boldsymbol{x}} + \sin\psi_2\,\hat{\boldsymbol{y}}$ and the transmitted plane wave is described by (20).

$$\phi_{out,1}(x,y) = k_0\left[\sqrt{x^2+y^2+F_2^2} + \sin\alpha_0\,(\cos\psi_1\, x + \sin\psi_1\, y)\right] \tag{20}$$

Thus, the phase delay distribution of TA_1 is defined as

$$\begin{gathered}\phi_{lens,1}(x,y) = \phi_{out,1} - \phi_{in,1} = \\ = k_0\left[\sqrt{x^2+y^2+F_2^2} - \sqrt{x^2+y^2+F_1^2} + \sin\alpha_1\,(\cos\psi_1\, x + \sin\psi_1\, y)\right] + k_0(F_1 - F_2)\end{gathered} \tag{21}$$

where $k_0(F_1 - F_2)$ is simply a phase zeroing term.

The second lens, TA_2, collimates the spherical wave transmitted from TA_1 and tilts the radiated plane wave by an offset elevation angle α_0 according to the rotation angle ψ_2. Therefore, its phase delay distribution $\phi_{lens,2}$ is described by (22).

$$\phi_{lens,2}(x,y) = \phi_{out,2} - \phi_{in,2} =$$
$$= k_0\left[-\sqrt{x^2+y^2+(F_2+d)^2} + \sin\alpha_0\,(\cos\psi_2\,x + \sin\psi_2\,y)\right] + k_0(F_2+d) \quad (22)$$

Note that $\phi_{in,2}(x,y,z) = \phi_{out,1}(x,y,z+d)$ and $k_0(F_2+d)$ is another phase zeroing term. Since $d \ll F_2$, we use

$$\phi_{lens,2}(x,y) = \phi_{out,2} - \phi_{in,2} =$$
$$= k_0\left[-\sqrt{x^2+y^2+F_2^2} + \sin\alpha_2\,(\cos\psi_2\,x + \sin\psi_2\,y)\right] + k_0F_2 \quad (23)$$

The phase distribution of the wave emitted from TA_2 can be rewritten as (24) and corresponds once again to the Risley Prism concept, as expected.

$$\phi_{out}(x,y) = \phi_{out,2} = \phi_{in,2} + \phi_{lens,2} = k_0(\sin\theta_{RP}\,[\cos\phi\,x + \sin\phi\,y]) \quad (24)$$

2.3 Dual-Band Transmit Arrays

The phase distributions of the incident and transmitted waves over the inner and outer surfaces of a TA can be factorized as $\phi_{in}(x,y,f) - \phi_{in}^{ref}(f) = k_0(f)h_{in}(x,y)$ and $\phi_{out}(x,y,f) - \phi_{out}^{ref}(f) = k_0(f)h_{out}(x,y)$, respectively. Consequently, the lens phase delay distribution, ϕ_{lens}, can also be similarly factorized as

$$\phi_{lens}(x,y,f) - \phi_f^{ref} = k_0(f)h_{lens}(x,y) \propto f \quad (25)$$

where $k_0(f) = 2\pi f/c$ is the free-space wavenumber and c is the speed of light in vacuum. Note that the reference phase terms, $\phi_{in}^{ref}(f)$, $\phi_{out}^{ref}(f)$ and ϕ_f^{ref}, are spatially constant terms but they may have different values for different frequencies. As long as the radiation pattern and the feed phase center position are frequency-independent, which is true in our work, this factorization is valid. In this case, the relation between the phase delay distribution for two different frequencies, f_1 and f_2, is simply given by

$$\phi_{lens}(x,y,f_2) - \phi_{f_2}^{ref} = \frac{f_2}{f_1}\left(\phi_{lens}(x,y,f_1) - \phi_{f_1}^{ref}\right) \tag{26}$$

Obviously, a dual-band cell must also satisfy this additional condition. Choosing a more convenient notation, we can define the phase delay of cell i as $\phi_f^i = \phi_{lens}(x_i, y_i, f) - \phi_f^{ref}$ and thus we have the relation $\phi_{f_2}^i = \frac{f_2}{f_1}\phi_{f_1}^i$, which is represented in Figure 4.

When the lens has electrically large dimensions (typically due to very high gain or low F/D requirements), there is the need to compensate several wavelengths of phase error, that is, the phase delay range must be very wide. In order to reduce the number of cells necessary to populate the entire phase range, it may be used phase wrapping [6]: since phase is a periodic function, it is only necessary to populate one periodic range. While in single-band lenses the periodic range is $[0°, 360°[$, in dual-band problems this is not so simple because each band will have a periodic range that is different from the other. To find these ranges, each cell i must satisfy

$$\phi_{f_2}^i + n \times 360° = \frac{f_2}{f_1}\left(\phi_{f_1}^i + m \times 360°\right) \tag{27}$$

where m, n are the number of $360°$ loops necessary to fill the periodic range for f_1 and f_2, respectively. For $\phi_{f_2}^i = \phi_{f_1}^i = 0°$, it becomes clear that $n/m = kf_2/f_1$, where k or $1/k$ is an integer number. To minimize the phase shift range, one should choose $k = 1$. Since $n, m \in \mathbb{N}$, the frequencies f_1, f_2 should be chosen as the pair of frequencies from the working spectral bands that have integer values and present the maximum greatest common divisor [6]. Since we are designing our antenna for satellite Ka-band applications, it was chosen $f_1 = 20\,GHz$, $f_2 = 30\,GHz$. Figure 4 shows the phase wrapping of a dual-band lens using the Reduced Phase-Pair (RPP) Plane.

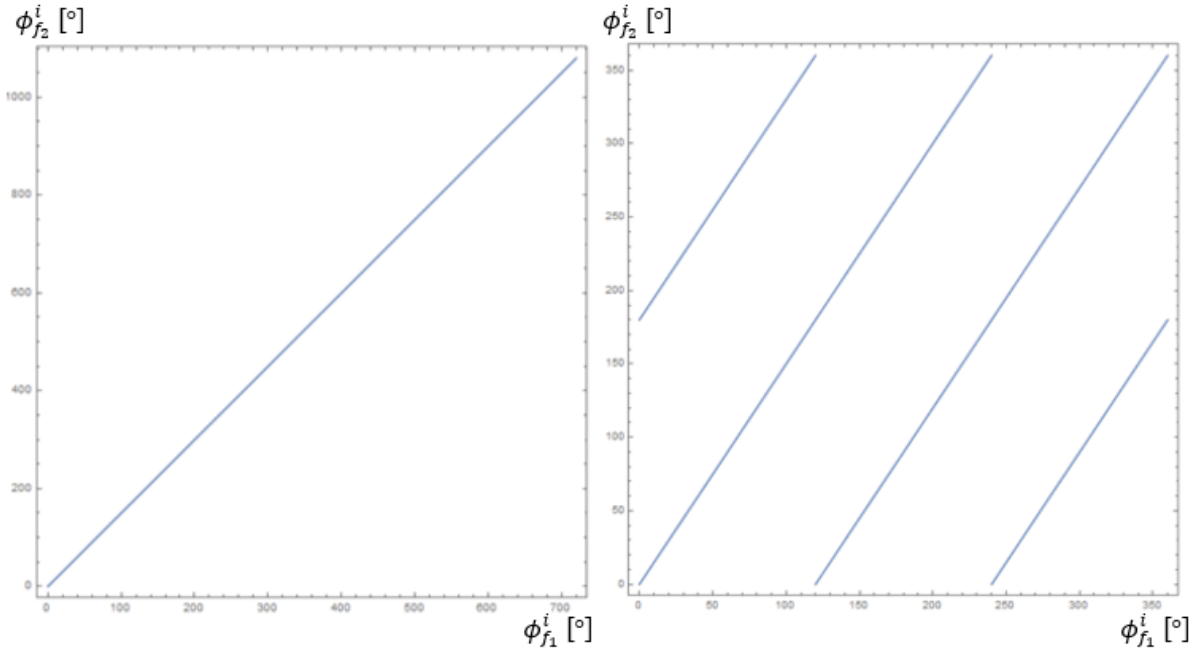

Figure 4 - Representation of the phase shift of a dual-band cell for frequencies $f_1 = 20\ GHz$ and $f_2 = 30\ GHz$ for an entire periodic range (left) and in the RPP (right).

Note that the phase delay function $\phi_{lens}(x, y)$ is symmetric to the transmission phase function, so the relation (18) is valid for both the phase delay and the transmission phase of cell i.

2.4 Unit Cells

The implementation of the PSS lenses mentioned above requires its discretization into multiple unit cells. This means that the real phase delay distribution is not $\phi_{lens}(x, y)$ but it is in fact $\phi_{real}(x, y) = \phi_{lens}(x_i, y_i)$, $|x - x_i| \leq P/2$, $|y - y_i| \leq P/2$ where (x_i, y_i) are the coordinates of the center of unit cell i and P is the cell dimension along the $x0y$ plane. Each one of these cells has a constant thickness t (see Figure 1) and it is designed to introduce a specific phase shift value. There are some conditions that are commonly imposed when designing these cells:

a) Sub-wavelength criterion: It is a known result from Array Theory that undesired grating lobes start to appear if the distance between consecutive elements becomes larger than half-wavelength, so analogously it is common to enforce that $P \leq \lambda_0/2$, where λ_0 is the free-space wavelength.

b) Symmetry regarding the $\hat{\boldsymbol{z}}$ axis: Since these PSS structures can be used in bi-directional links, they should be reciprocal systems, that is, $S_{21} = S_{12}$. Obviously, the easiest way to satisfy this condition is to have symmetric cells regarding the normal axis (propagation direction).

As explained in the previous chapter, passive cells can use two working principles: phase-delay or phase-rotation (see [20] for a deeper understanding of this topic).

PD cells present different phase shifts due to the variation of the frequencies related to their resonances (maximum transmission) and zeros (maximum reflection) by altering very slightly the dimensions of the metallic components. This means that to build a TA using PD cells it is necessary to design a discrete set of cells with good transmission coefficients and different phase shifts that discretize the phase shift range within a certain frequency band. Since this is not always easy, it may be acceptable to compromise the transmission performance of some cells in order to improve the phase shift discretization. Although less layers reduce the dependence on the incidence angle, more layers allow a bigger phase shift range, so it should be used the least number of layers that achieve the desired phase shift range.

The working principle of the PR cells, on the other hand, is based on the rotation of the metallic components. In this case, it is only necessary to design one single cell with a good transmission coefficient (which should not be affected by the cell rotation) and the entire TA is built using the same cell rotated by different angles.

PD cells have a double-symmetry regarding the $\hat{\boldsymbol{x}}$ and $\hat{\boldsymbol{y}}$ axes and thus have the same response for x and y-linearly polarized incident waves, while PR cells present an anti-symmetry: the transmission coefficient should have the same amplitude for both axes and a $180°$ transmission phase difference between them. This means that a PD TA is insensible to the polarization and orientation of the feed, but this is not true for a PR TA: the RHCP or LHCP component of the incident wave will be filtered depending on how it is designed. If the feed is RHCP, the PD TA will transmit a RHCP wave and reflect a LHCP wave whereas the RHCP-PR TA will transmit a LHCP wave and reflect a RHCP wave. However, if the feed is LHCP, the PD TA will transmit a LHCP wave and reflect a RHCP wave but the RHCP-PR TA will disperse both the transmitted RHCP and the reflected LHCP waves. This last characteristic is great to filter the undesired cross-polarization component of a feed with CP.

When designing dual-band cells, each cell must present different phase shifts for the two bands. Since the phase shift in PR cells is defined by its rotation angle, it is not usual to use them in dual-band scanning problems because the complexity increases significantly.

There is an alternative to designing a TA with dual-band Cells, which is an Interleaved solution. The idea is to design up-link and down-link single-band cells that have good transmission coefficients and the same phase delay for the down-link and up-link bands respectively and then mix them in an interleaved distribution [25]. Although this is much simpler, Nature is not easily fooled and the Directivity suffers a $3\ dB$ loss, which is the same as having a dual-band TA with half the surface.

For the reasons mentioned above, we have designed the transmit arrays using dual-band PD cells.

3 Design and Simulation Results

3.1 Methods to Improve the Full-Wave Simulations Efficiency

The full-wave simulations of large systems, such as our antenna, are very complex in terms of memory and time required to perform. There, before presenting and discussing the design process of our solution and the simulation results, it is important to introduce two methods that were used to improve the efficiency of the full-wave analyses of the transmit arrays and the rotary system.

As shown in Figure 18, a significant part of the simulation volume corresponds to the empty space between the feed (Horn antenna) and the lenses. To eliminate this unnecessary volume, the Horn antenna was replaced by an equivalent feed source close to the lenses (blue screen): the near-field values of the radiation from the Horn antenna were sampled over a large plane surface and later they are reproduced by an equivalent feed source generating the same near and far-field radiation as the real feed source. This corresponds to the “Synthetize feed” step shown below.

Also, the proper discretization of the unit cells with small metallic components, as in our case, requires an extremely thin Mesh. This is still feasible when dealing with individual cells, but when studying transmit arrays with several unit cells this becomes problematic and the complexity of the simulations increases significantly. So, before using the real cells, the transmit arrays were studied using the equivalent dielectric description of the cells proposed in [26] (“Homogenized lens” step): the cells are replaced by dielectric blocks with the same physical dimensions and the same transmission coefficients as the real ones. Note that the unit cell sub-wavelength assumption of the Homogenization Theory is verified because $P \leq \lambda_0/2$. For each dielectric cell the relative electric permittivity ε_{eq}^{i} and magnetic permeability μ_{eq}^{i} are defined according to

$$\varepsilon_{eq,f}^{i} = -\frac{\phi_f^i + \phi_f}{k_0 t}\frac{1+\left|\Gamma_f^i\right|}{1-\left|\Gamma_f^i\right|}$$
$$\mu_{eq,f}^{i} = -\frac{\phi_f^i + \phi_f}{k_0 t}\frac{1-\left|\Gamma_f^i\right|}{1+\left|\Gamma_f^i\right|} \quad (28)$$

where ϕ_f^i is the phase transmission, k_0 is the free-space wavenumber and Γ_f^i is the reflection coefficient at frequency f. ϕ_f is an arbitrary phase constant used to guarantee that $\varepsilon_{eq,f}^{i}, \mu_{eq,f}^{i} \geq 1$ at frequency f. Obviously, this transmission coefficients correspondence between the real cells and the equivalent ones is only valid for a single specific frequency, so a set of dual-band cells is represented by two distinct sets of single-band dielectric cells.

Table 1 compares the resources necessary to simulate each one of the three methods shown in Figure 5 using the lens presented in [9].

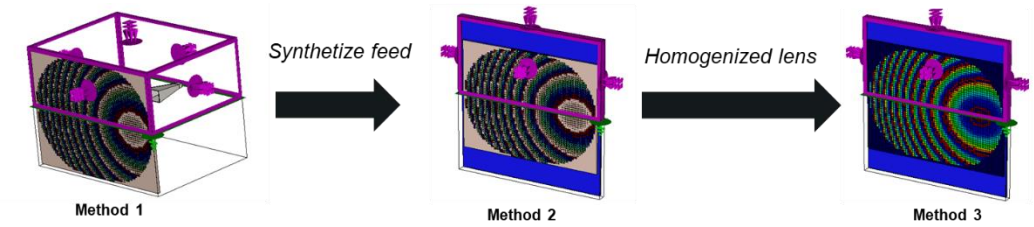

Figure 5 - Equivalent feed source and dielectric cell description methods

Table 1 - Comparison of the resources necessary to simulate each one the methods in Figure 5

Method	Mesh cells	Memory (GB)	Simulation time	Mesh Density	
				Smallest cell (mm)	Largest cell (mm)
1	87 M	20	5h 55 m	0.09	0.85
2	8 M	6	2h 54 m	0.09	0.83
3	0.8 M	0.6	24 m	0.50	2.11

3.2 Unit Cell Design

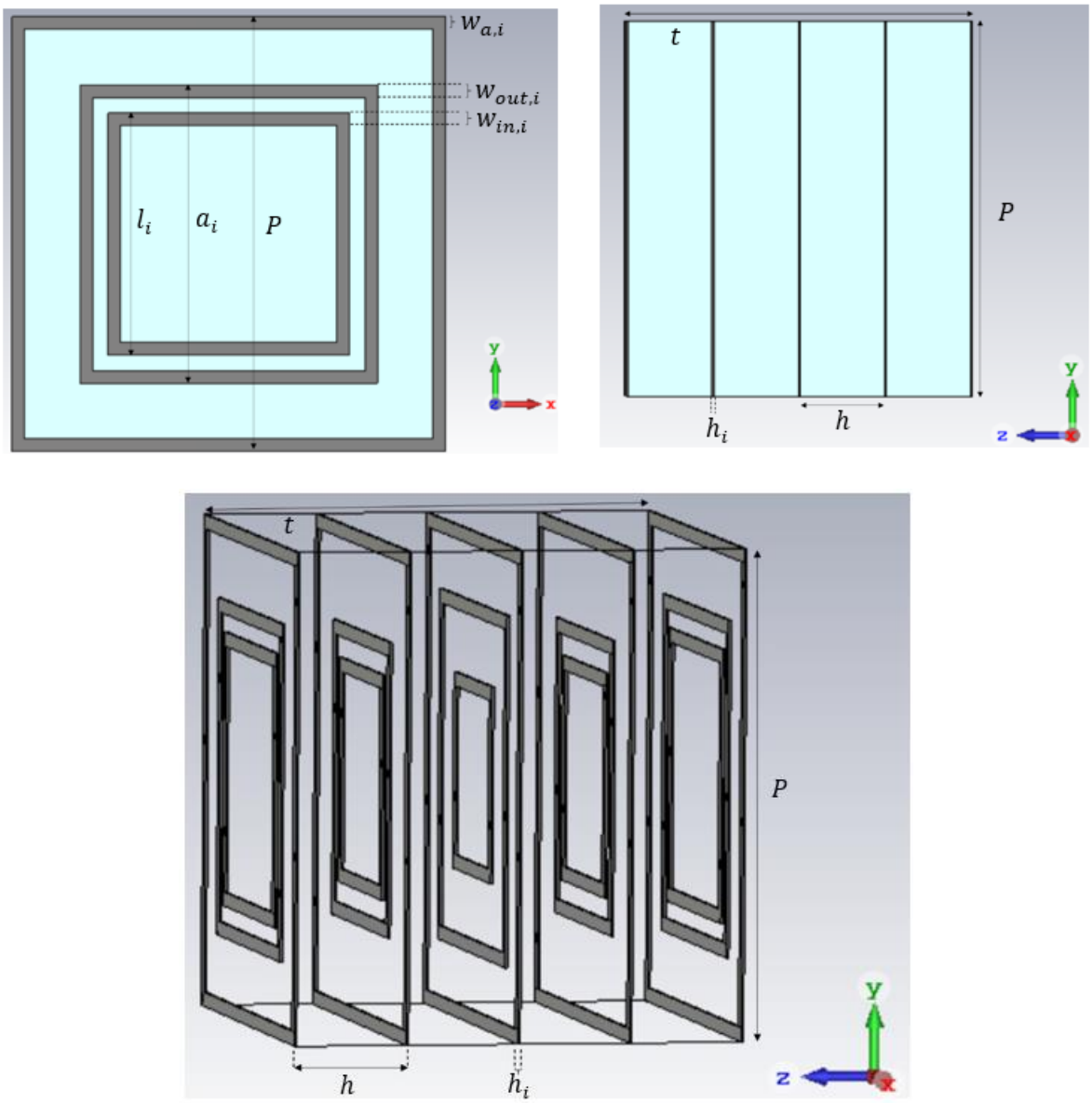

Figure 6 – Dual-band PD unit cell's design model: the square metal rings are represented in dark grey and the dielectric layers in light green; the layer's number label decreases with z. Up: front (left) and side (right) view of a cell. Down: 5 layers of metal insertions without the dielectric layers

Figure 6 shows the design of the unit cell used in this work, it was inspired by the PG TA cells presented in [8]: each cell has 5 very thin metal insertion layers interleaved with 4 dielectric layers and each metal layer consists of 2 or 3 square rings (the number of rings may vary from layer to layer in each cell). The symmetry conditions mentioned in the previous chapter for PD cells require that the metal layers 1 and 5 are identical, as well as layers 2 and 4, and each one of the layers must have a double-symmetric geometry (it could also be a circular geometry, for example).

The original cells in [8] are designed to operate at the X and Ku-Bands (8 and 14 GHz), so the cell's width, P, was scaled by a factor of $14/30$ to operate at the Ka-band (20 and 30 GHz) and optimised afterwards. It is used the factor $14/30$ and not $8/20$ because the phase range in the up-link band ($[0°, 1080°[$) is larger than the one in the down-link band ($[0°, 720°[$). The chosen dielectric and metal thickness, h and h_i, are the smallest values available in our laboratory. The dielectric is Rogers RT/Duroid 5880 ($\varepsilon_r = 2.2$, $\tan\delta = 0.0009$) and it was also chosen from the set of materials that were available. All these macro-parameters are presented in Table 2.

Table 2 - Unit cell's macro-parameters

Macro-Parameter	Value [mm]
P	3.5
h	0.787
h_i	0.017
t	3.233

Once the cell geometry and macro-parameters are fixed, it is necessary to populate the RPP plane [6]. This iterative process consists of three steps:

1 – Generate several cells and reject those that do not satisfy the transmission amplitude criterion;

2 – Choose $\left(\phi_{f_1}^{ref}, \phi_{f_2}^{ref}\right)$ in order to maximize the number of cells that satisfy equation (26);

3 – If there are not enough valid cells to satisfy the phase discretization step criterion, then go back to Step 1.

The transmission amplitude criterion was defined as $|S_{21}| \geq -1\ dB$ and the phase discretization step criterion as $\Delta\phi_{f1} \leq 30°, \Delta\phi_{f_2} \leq 45°$.

In Step 1 it is possible to control the cell's transmission response by altering its micro-parameters. When a ring dimension (l_i or a_i) increases, its resonance frequency decreases, and thus the cell's frequency response is "shifted" left. In that case, the transmission phase decreases and the cell's phase delay increases since they are symmetric. When a ring width ($w_{in,i}$, $w_{out,i}$ or $w_{a,i}$) increases, the cell's bandwidth increases as well, which can be used to improve the cell's transmission amplitude. Finally, the exterior ring increases the cell's phase delay which is very useful when designing cells with higher values for the wrapped transmission phase (RPP plane), but not so much for lower values, which is why some cells have layers with three rings while others only have two.

Dual-band cell geometries based on inductive elements like metal rings [8, 24] have an interesting characteristic that is not found on capacitive metal patches geometries [6]: it is possible to design some elements to be resonant in the up-link band and others to be resonant in the down-link band. This way the dual-band problem can be treated almost as two single-band problems. Obviously, they are not

completely independent because the down-link elements are not “invisible” in the up-link band and vice-versa, there are always coupling effects between the elements, but the problem can be dealt in a more elegant way than simply a brute-force approach of trial and error. Usually, up-link elements have a far less impact over the down-link results than the contrary. In our case, the interior rings affect primarily the cell’s response at f_2, the middle rings at f_1 and the exterior rings affect both bands. Figures 7 and 8 show this behaviour by varying independently the l_i or a_i parameters of a cell, respectively.

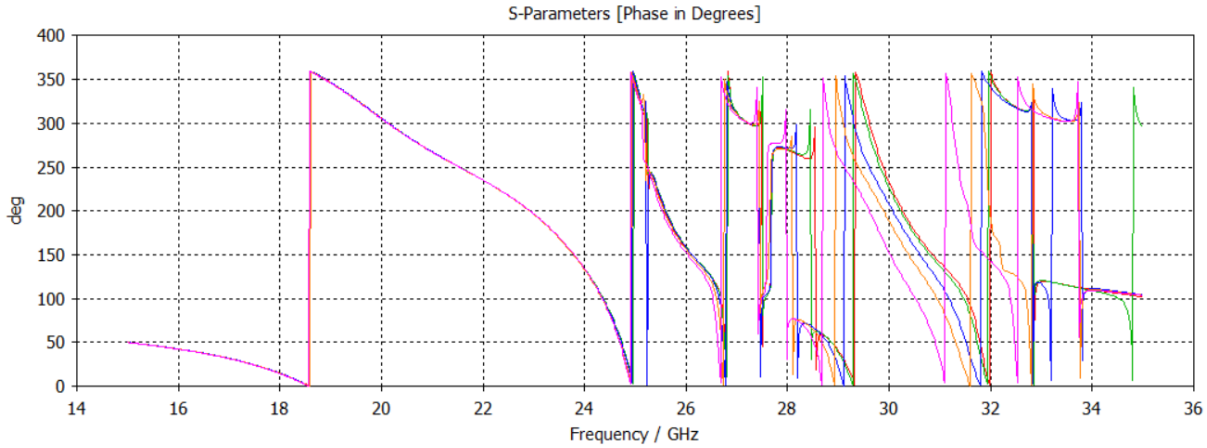

Figure 7 - Transmission phase frequency response of a cell for different micro-parameters l_i. While the phase range in f_1 is only $1°$, in f_2 it is near $80°$

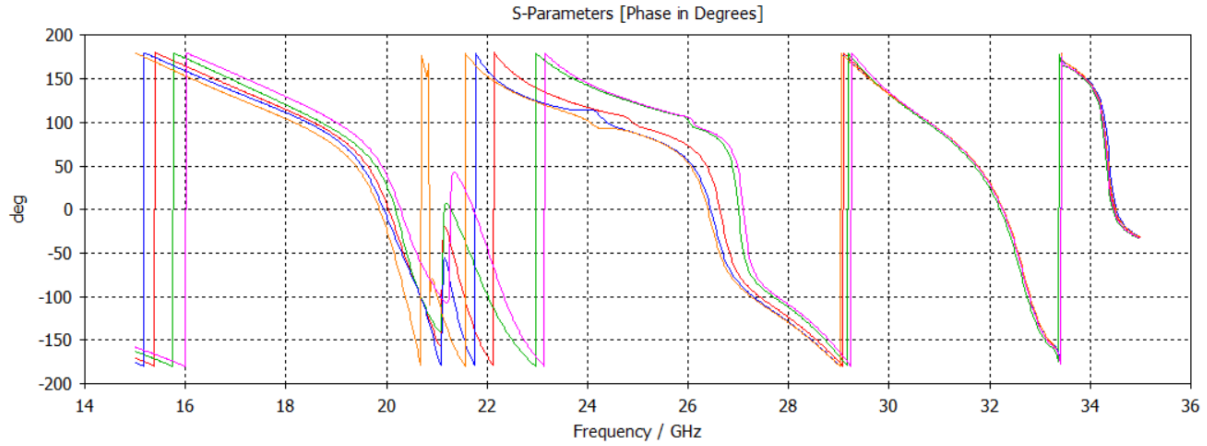

Figure 8 - Transmission phase frequency response of a cell for different micro-parameters a_i. While the phase range in f_1 is around $60°$, in f_2 it is only $3°$

In total, 29 dual-band PD cells were designed using full-wave analysis in the Frequency Domain using the CST software [27] considering a normal incident plane wave with linear polarization and periodic boundaries. Due to the sub-wavelength criterion, the phase delay in a small neighbourhood of a cell varies slowly. This means that two cells that are next to each other are expected to be very similar because they share the same global geometry and the parameters will only differ slightly, unless there

is an abrupt unwrapped phase jump associated with the phase wrapping. For this reason, the periodic boundaries used in the individual cell analysis are a valid approximation despite the TA's finite dimensions and heterogeneous phase distribution. The micro-parameters of these cells are presented in Appendix A. There is only one column for the width of the middle ring because $w_{out,i} = w_{out} = 0.1\,mm$ and $w_{a,i} = 0\,mm$ means there is no exterior ring. It was not used ring widths or gaps between rings smaller than $0.1\,mm$ due to the precision of the prototype's manufacturing process.

Appendix B presents the reflection amplitude, transmission amplitude and transmission phase of these cells at $f_1 = 20\,GHz$ and $f_2 = 30\,GHz$. Figures 9 and 10 show the amplitude and phase distributions for the pair of phase references $\left(\phi_{f_1}^{ref} = -80°, \phi_{f2}^{ref} = -22.5°\right)$ that minimize the phase error. Table 3 shows the corresponding statistical analysis.

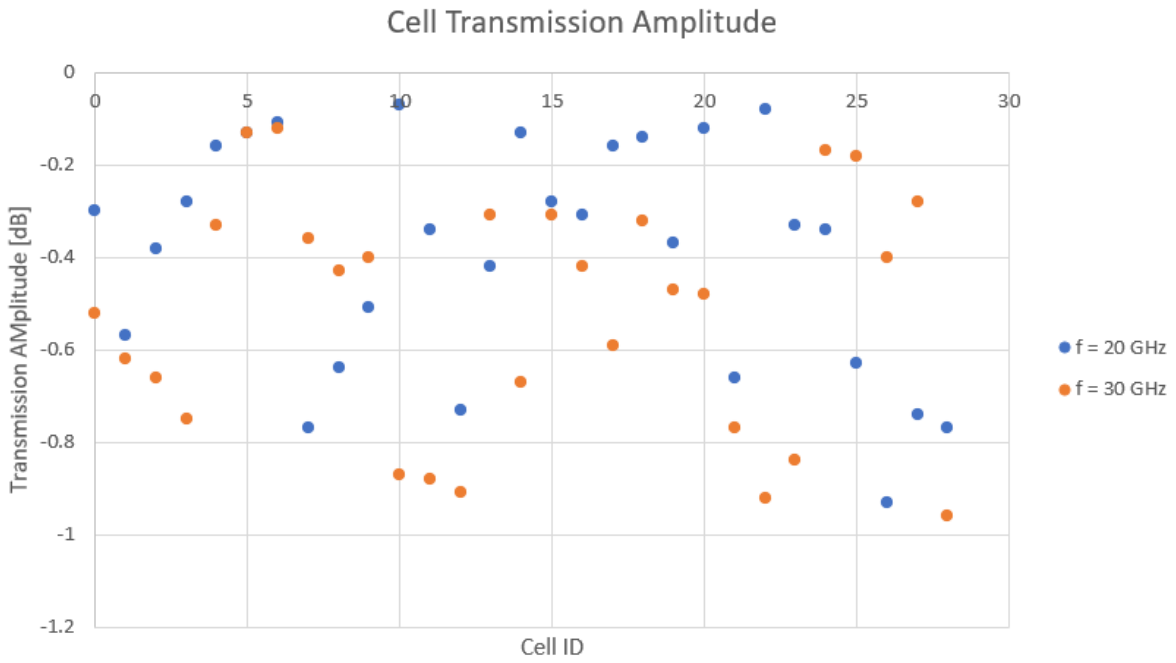

Figure 9 - Transmission amplitude of each cell: $f_1 = 20\,GHz$ (blue) and $f_2 = 30\,GHz$ (orange). Some cells have the same transmission amplitude in both frequencies, so it is only possible to see the f_2 data

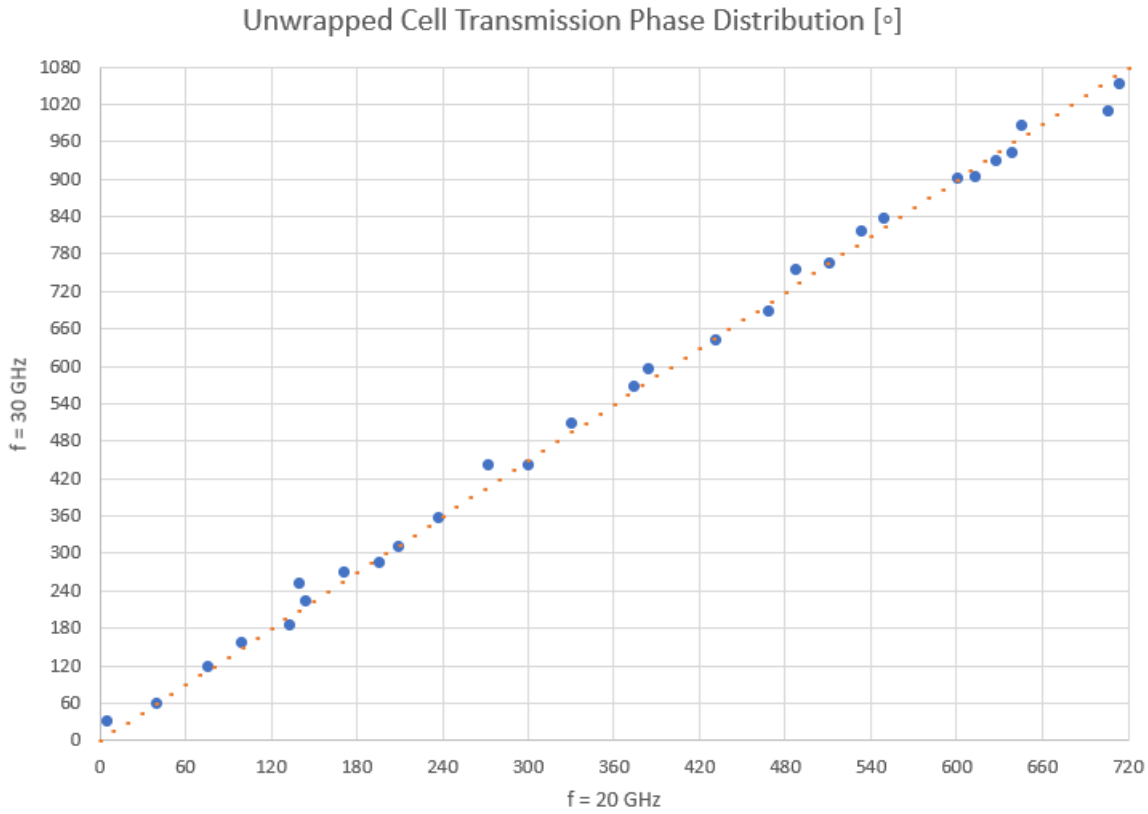

Figure 10 - Unwrapped transmission phase of each cell: in orange, the graphical representation of the relation (26); in blue, the cells' transmission phase distribution. The lowest phase corresponds to $ID = 0$ and the highest to $ID = 28$

Table 3 - Dual-band PD cells' transmission coefficients analysis

Frequency	$\boldsymbol{T}$	**Phase Error**		**Phase Discretization Step**
	Average $[\boldsymbol{dB}]$	**Average** [°]	**Standard Deviation** [°]	**Average** [°]
$f_1 = 20\ GHz$	-0.39	9.3	7.6	24.8
$f_2 = 30\ GHz$	-0.52	13.9	11.3	37.2

Every cell satisfies the transmission amplitude criterion, the average phase discretization satisfies the phase discretization criterion and the phase error is with an acceptable range. Thus, this is a valid set of dual-band PD cells.

We have used more degrees of freedom than the ones used in [8] by varying the width of the metal rings independently between layers. This increases the complexity of the problem, but it also improves the results: our cells present a better transmission amplitude, they have a smaller average phase discretization and P is electrically smaller.

So far, all the results were obtained using normal incidence, but the incidence angle is not always the same, it depends on the cell's position on the transmit array and the incident wave. For this reason, it is important to study the cells performance for different angles. Table 4 shows the response of 3 cells

for the incidence angles $\theta_{in} = 0°, 20°, 40°, 60°$. The cells 0, 16 and 13 were chosen to represent the three types of cell: 2 rings with $w_{in,i} = 0.1\ mm$, 2 rings with $w_{in,i} \geq 0.1\ mm$ and 3 rings, respectively.

Table 4 - Dual-band PD cells' response to different incidence angles θ_{in}

ID	$\boldsymbol{\theta_{in}}$ [°]	$\boldsymbol{f_1 = 20\ GHz}$		$\boldsymbol{f_2 = 30\ GHz}$	
		$\boldsymbol{T}$ $[\boldsymbol{dB}]$	$\boldsymbol{\phi}$ [°]	$\boldsymbol{T}$ $[\boldsymbol{dB}]$	$\boldsymbol{\phi}$ [°]
0	0	-0.30	286.6	-0.52	5.4
	20	-0.32	303.7	-0.51	8.9
	40	-1.19	351	-0.33	17.7
	60	-6.43	43.6	-0.59	30.9
13	0	-0.42	251.2	-0.31	123.7
	20	-0.59	255.2	-0.38	123.5
	40	-1.20	264.4	-0.92	124
	60	-3.08	273	-2.72	117.4
16	0	-0.31	352.4	-0.42	257.4
	20	-0.64	7.4	-0.46	256.6
	40	-2.81	43.4	-1.04	255.3
	60	-8.70	78.4	-2.60	255.2

Overall, the transmission amplitude deteriorates and the transmission phase increases for higher values of θ_{in}. Also, it seems the cell performance is less sensible to the incidence angle for $f_2 = 30\ GHz$ and for cells with 3 metal rings instead of 2. For a ratio $F/D = 0.8$, as in our case, the incidence angle θ_{in} is always smaller than $40°$ so there should be no problem regarding the incidence angle.

3.3 PO/GO Analysis of the Risley Prism TA System

Besides designing individually each unit cell, it is important to study the performance of the global system. To study and determine the main geometrical parameters, it was performed a Physics Optics/Geometrical Optics (PO/GO) analysis using ideal phase distributions for one and two lenses scenarios.

This analysis was done using the KH3D_near program developed in house [28]. The near and far-field radiation are calculated using the vector form of the Stratton-Chu integral formula, without far-field approximations.

Each PSS lens is assumed to have no thickness like a two-dimensional surface, and it is only represented by the equivalent electric and magnetic surface currents over it. The radiation pattern of each lens is calculated using a three steps process:

1 – Calculation using Mathematica of the equivalent surface currents over the incident surface of the lens, $J_{in}(x,y)$, corresponding to the incident wave for each lens. The feed is assumed to be a Gaussian illumination $U(\theta) \sim \exp\{-(\theta/\sigma)^2\}$, where σ is the beamwidth;

2 – Calculation using Mathematica of the equivalent surface currents over the output surface, $J_{out}(x,y) = J_{in}(x,y) \cdot S_{21}(x,y)$, corresponding to the radiated wave;

3 – Calculation using KH3D_near of the far-field radiation.

To perform Step 1, it is necessary to define the tangential magnetic field $\boldsymbol{H_a} = \frac{1}{\eta_0}\hat{\boldsymbol{k}} \times \boldsymbol{E_a}$ before calculating the equivalent currents. $\hat{\boldsymbol{k}} = \hat{\boldsymbol{k}}(x,y)$, but the tangential magnetic Field is approximated as $\boldsymbol{H_a} = \frac{1}{\eta_0}\hat{\boldsymbol{z}} \times \boldsymbol{E_a}$. This simplifies the problem and the results are almost identical.

In Step 2, the transmission function $S_{21}(x,y)$ is obviously related to the spatial distribution of the unit cells:

$$S_{21}(x,y,f) = T_f^i e^{-j\phi_{real}(x,y,f)} = T_f^i e^{j\phi_f^i}, \quad |x - x_i| \le P/2\,, |y - y_i| \le P/2 \tag{29}$$

where (x_i, y_i) is the center of the lens discretisation grid cell i, T_f^i and ϕ_f^i are the transmission amplitude and phase of cell i at frequency f, and ϕ_{real} is defined as in the section “Unit Cells” of the previous chapter. Cell i is chosen as the cell that minimizes the square-phase error on both frequencies $f_1 = 20\ GHz$ and $f_2 = GHz$:

$$i = \underset{k}{\operatorname{argmin}} \left\{ \left(\phi_{f_1}^k - \phi_{real}(x,y,f_1)\right)^2 + \left(\phi_{f_2}^k - \phi_{real}(x,y,f_2)\right)^2 \right\} \tag{30}$$

When dealing with more than one TA, it is necessary to study the propagation from one lens to the other. The radiation pattern of the Risley Prism-like system is calculated in a similar way to the single lens case:

1 – Calculation using Mathematica of the equivalent surface currents over the incident surface of Lens 1, $J_{in,1}(x,y)$, corresponding to a spherical incident wave. The feed is once again assumed to have a Gaussian distribution;

2 – Calculation using Mathematica of the equivalent surface currents over the output surface of Lens 1, $J_{out,1}(x,y) = J_{in,1}(x,y) \cdot S_{21,1}(x,y)$, corresponding to the transmitted wave;

3 – Calculation using KH3D_near of the near-field radiation over Lens 2;

4 – Calculation using Mathematica of the equivalent surface currents over the incident surface of Lens 2, $J_{in,2}(x,y)$, corresponding to the wave transmitted by Lens 1;

5 – Calculation using Mathematica of the equivalent surface currents over the output surface of Lens 2, $J_{out,2}(x,y) = J_{in,2}(x,y) \cdot S_{21,2}(x,y)$, corresponding to the radiated wave;

6 – Calculation using KH3D_near of the far-field radiation.

It is obtained only approximated results, but the solution becomes very time-efficient which is especially useful when one wants to perform several simulations to quickly gain an initial grasp of the system's behaviour using different sets of parameters.

3.3.1 Single Lens

The Taper Level is an important parameter when designing transmit arrays, it can have a big impact on the radiation pattern because the radiation vectors, $\boldsymbol{F}(\theta,\phi)$ and $\boldsymbol{F_m}(\theta,\phi)$, are 2-D Fourier Transforms of the Equivalent Currents, $\boldsymbol{J_s}(x,y)$ and $\boldsymbol{J_{ms}}(x,y)$ (see equation (3)). To understand its impact, it may be useful to remember the following results:

– Discontinuous Equivalent Currents generate a radiation pattern with undesired side lobes. In a similar way, the 1-D Fourier Transform of a rectangular pulse is a sinc pulse. It is important to have a small Taper Level to minimize the discontinuity over the lens border;

– The aperture efficiency e_a is maximum for a uniform Equivalent Current [29] and, since $D_{max} \sim e_a$, we want to maximize e_a. Also, in a similar way, the 1-D Fourier Transform of a Dirach pulse is a constant pulse, which would be equivalent to a very large lobe with a small magnitude. Larger Taper Level values are associated with Equivalent Currents that are more distributed in a more uniform way.

Gaussian feeds are very popular exactly because they are a continuous pulse and, for a fixed Focal Distance F_1, the Taper Level is controlled by its beamwidth σ. If σ is too small, the Taper Level will also be too small, and we will have a radiation pattern with a good SLL but a small e_a; on the other hand, if σ is too large, we will have a poor SLL but a high e_a. It is necessary to do a careful trade-off between the SLL and e_a, so typically the best choice is to define σ such that the Taper Level value is close to $-10\ dB$. It is also possible to compensate a feed with a large σ by decreasing F_1.

To better understand the impact of the Taper Level on the performance of a lens, it was used the new phase configuration (23) of Lens 2 with $f_1 = 20\ GHz$, $D = 140\ mm$, $F_2 = 150\ mm$, $\psi_2 = 0°$, $\alpha_0 = 25°$, a spherical LHCP feed and three different beamwidth values: $\sigma = 13.0°$, $\sigma = 16.4°$, $\sigma = 25.9°$. Below, Figures 11 – 14 and Table 5 show the results using the PO/GO analysis after Steps 2 and 3.

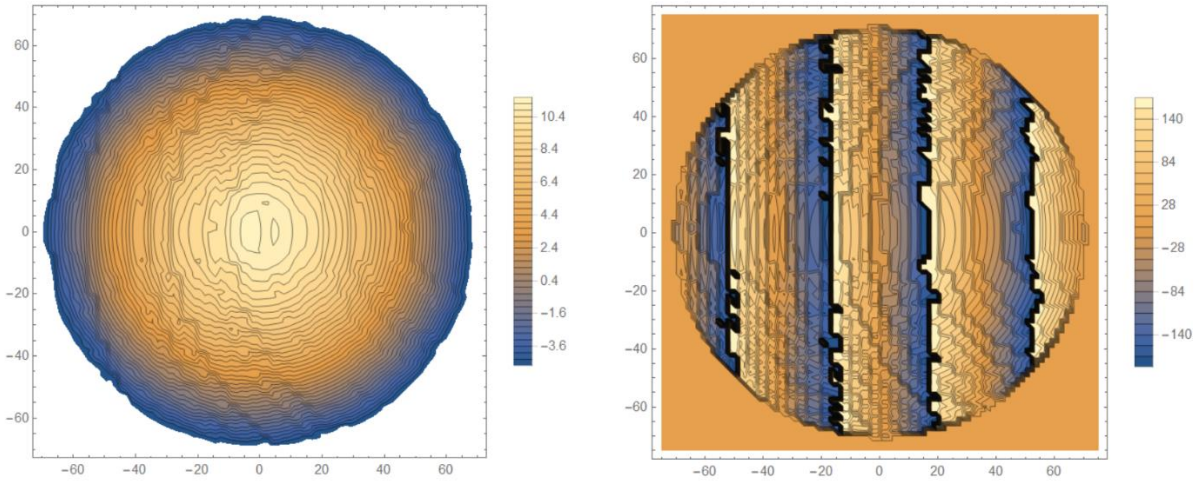

Figure 11 - Absolute value of the Equivalent Electric Current in $dBAm^{-2}$ (left) and the phase of its x-component in degrees (right) of Lens 2 at $f_1 = 20\ GHz$ for $F_2 = 150\ mm$, $\alpha_0 = 25°$, $\psi_2 = 0°$ and $\sigma = 13.0°$. The axes are in mm and they correspond to the $\hat{\boldsymbol{x}}$ and $\hat{\boldsymbol{y}}$ axes (horizontal and vertical, respectively)

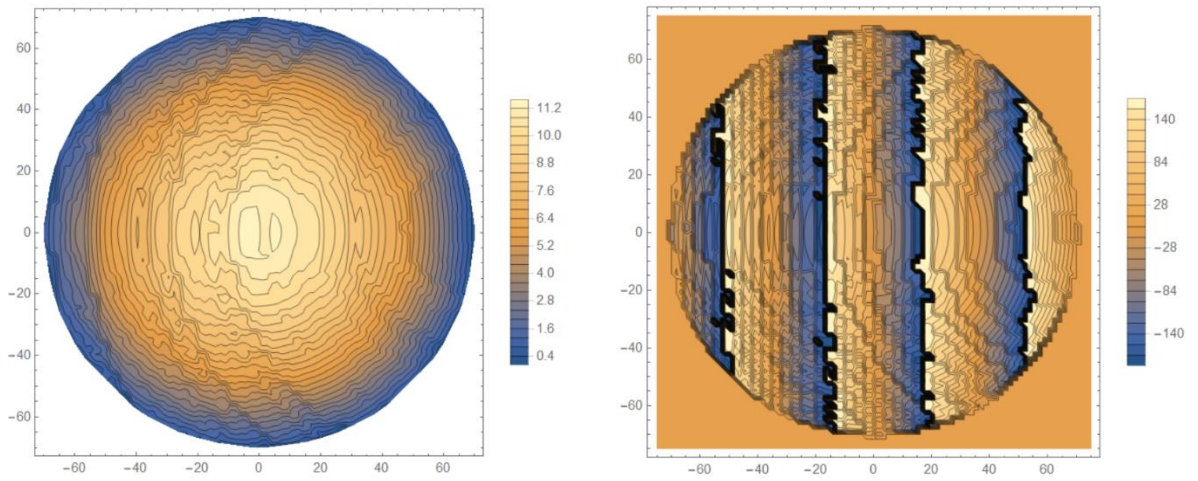

Figure 12 - Absolute value of the Equivalent Electric Current in $dBAm^{-2}$ (left) and the phase of its x-component in degrees (right) of Lens 2 at $f_1 = 20\ GHz$ for $F_2 = 150\ mm$, $\alpha_0 = 25°$, $\psi_2 = 0°$ and $\sigma = 16.4°$. The axes are in mm and they correspond to the $\hat{\boldsymbol{x}}$ and $\hat{\boldsymbol{y}}$ axes (horizontal and vertical, respectively)

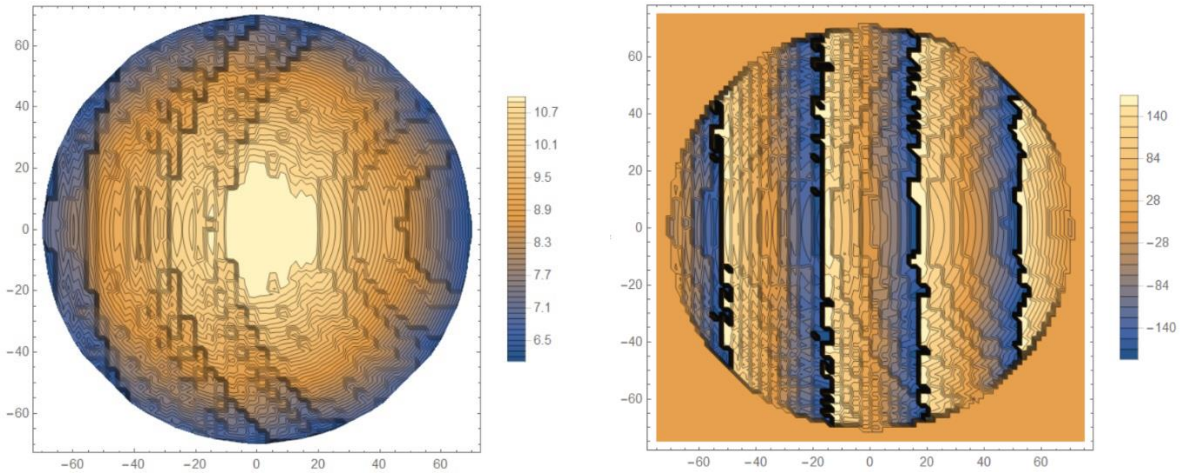

Figure 13 - Absolute value of the Equivalent Electric Current in $dBAm^{-2}$ (left) and the phase of its x-component in degrees (right) of Lens 2 at $f_1 = 20\ GHz$ for $F_2 = 150\ mm$, $\alpha_0 = 25°$, $\psi_2 = 0°$ and $\sigma = 25.9°$. The axes are in mm and they correspond to the $\hat{x}$ and $\hat{y}$ axes (horizontal and vertical, respectively)

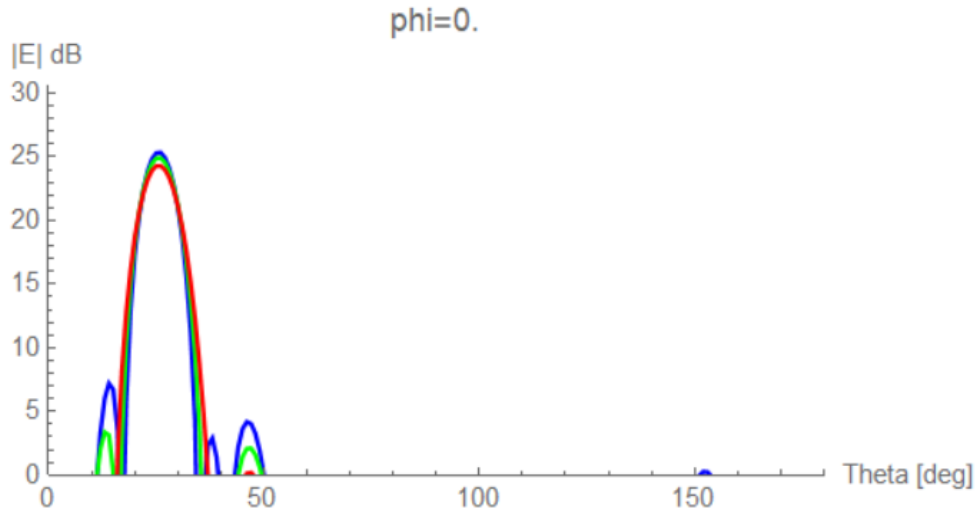

Figure 14 - $x0z$ Directivity cut of components E_θ and E_φ of Lens 2 at $f_1 = 20\ GHz$ with $F_2 = 150\ mm$, $\alpha_0 = 25°$ and $\psi_2 = 0°$ for different values of σ: $\sigma = 13.0°$ (red), $\sigma = 16.4°$ (green) and $\sigma = 25.9°$ (blue). The cross-polarization is so small, it is not possible to distinguish the two orthogonal components

Table 5 - Far-field results of Lens 2 at $f_1 = 20\ GHz$ with $F_2 = 150\ mm$, $\alpha_0 = 25°$ and $\psi_2 = 0°$ for different values of σ

$\boldsymbol{\sigma}$ [°]	Taper Level $[\boldsymbol{dB}]$	$\boldsymbol{D_{max}}$ $[\boldsymbol{dBi}]$	$\boldsymbol{SLL}$ $[\boldsymbol{dB}]$	$\boldsymbol{\theta_{max}}$ [°]
13.0	-16.45	27.4	-24	25
16.4	-10.81	28.0	-21.5	25
25.9	-4.4	28.4	-18.9	25

The radiation patterns of Figure 14 only show the $\varphi = 0°$ plane because it is the only relevant cut-plane since Lens 2 radiates a plane wave propagating along this direction. Also, there is approximately

a $-3\,dB$ difference D_{max} and the radiation pattern graphics maximum because it is represented each one of the LHCP Electric Field components and not its norm. As expected, SLL is minimum for σ_1 and the Directivity is maximum for σ_3. Also, in all three cases, $\theta_{max} = \alpha_0 = 25°$ and the phase distributions in Figures 11 – 13 are consisted with expression (24) for $\psi_2 = 0°$, confirming this PO/GO analysis gives reliable results, despite being simpler than a full-wave analysis.

Another parameter that is very important to analyse is the offset elevation angle α_0. To study it, it was used Lens 2 at $f_1 = 20\,GHz$ and $f_2 = 30\,GHz$ with three different elevation angles: $\alpha_0 = 25°$, $\alpha_0 = 30°$, $\alpha_0 = 35°$. It was considered $D = 140\,mm$, $F_2 = 150\,mm$, $\psi_2 = 0°$, $\sigma = 16.4°$ and a spherical LHCP feed. The results are shown in Figures 15 – 16 and Table 6.

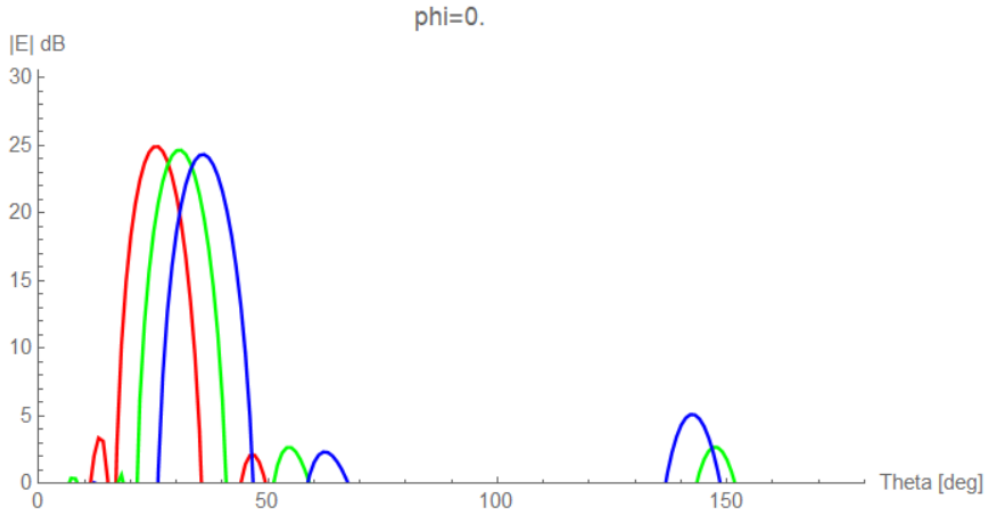

Figure 15 - $x0z$ Directivity cut of components E_θ and E_φ of Lens 2 at $f_1 = 20\,GHz$ with $F_2 = 150\,mm$, $\sigma = 16.4°$ and $\psi_2 = 0°$ for different values of α_0: $\alpha_0 = 25°$ (red), $\alpha_0 = 30°$ (green) and $\alpha_0 = 35°$ (blue). The cross-polarization is so small, it is not possible to distinguish the two orthogonal components

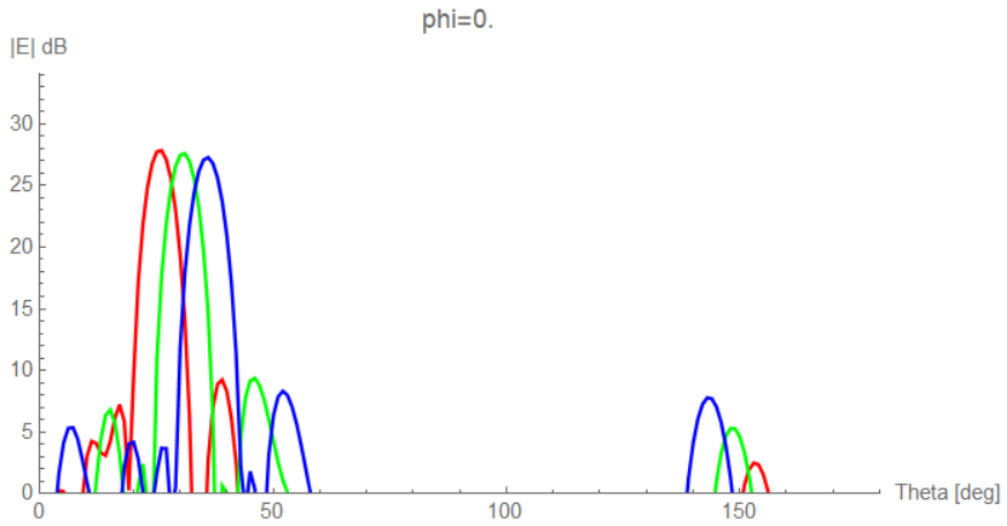

Figure 16 - $x0z$ Directivity cut of components E_θ and E_φ of Lens 2 at $f_2 = 30\ GHz$ with $F_2 = 150\ mm$, $\sigma = 16.4°$ and $\psi_2 = 0°$ for different values of α_0: $\alpha_0 = 25°$ (red), $\alpha_0 = 30°$ (green) and $\alpha_0 = 35°$ (blue). The cross-polarization is so small, it is not possible to distinguish the two orthogonal components

Table 6 - Far-field results of Lens 2 at $f_1 = 20\ GHz$ and $f_2 = 30\ GHz$ with $F_2 = 150\ mm$, $\sigma = 16.4°$ and $\psi_2 = 0°$ for different values of α_0

$\boldsymbol{\alpha_0}$ [°]	$\boldsymbol{D_{max}}$ $[\boldsymbol{dBi}]$		$\boldsymbol{SLL}$ $[\boldsymbol{dB}]$		$\boldsymbol{\theta_{max}}$ [°]	
	$\boldsymbol{f_1}$	$\boldsymbol{f_2}$	$\boldsymbol{f_1}$	$\boldsymbol{f_2}$	$\boldsymbol{f_1}$	$\boldsymbol{f_2}$
25	28.0	31.0	-21.5	-18.5	25	26
30	27.7	30.8	-22.1	-18.4	30	31
35	27.4	30.5	-19.2	-18.7	36	35

Figure 16 shows a reflected side lobe at $\theta = 180° - \theta_{max}$ symmetric to the transmitted main lobe at $\theta = \theta_{max} = \underset{\theta}{\operatorname{argmax}}\, U(\theta, \varphi = \psi_2)$, which is a known effect of transmit arrays [20], and its magnitude increases with the offset angle α_0. Also, the Directivity decreases with α_0 and increases with the frequency, as expected. This relation between the Directivity and the elevation angle, $D_{max} \sim \cos\theta_{max}$, is responsible for the scan loss associated with any beam steering mechanism.

These simulations confirm that the lenses performance regarding D_{max} and SLL improve for smaller values of α_0.

3.3.2 Two Lenses

After studying the individual performance of Lens 2, it is important to study the beam scanning performance of our Risley Prism-like system of two lenses and to compare the elevation angle of the main lobe θ_{max} with expression (9). For that, it was used two lenses, Lens 1 and Lens 2, separated by

an air gap with thickness $d = 5\,mm$, diameter $D = 140\,mm$, $F_1 = 100\,mm$, $F_2 = 150\,mm$, an offset elevation angle $\alpha_0 = 25°$ and a feed with LHCP. Using $\sigma = 21.8°$, the Taper Level over Lens 1 is close to $-10\,dB$ for $F_1 = 100\,mm$. Figures 17 – 18 and Table 7 show the results for $\phi = 0°$ and 4 different differential rotation angles: $\xi = 90.0°$, $\xi = 78.1°$, $\xi = 66.1°$, $\xi = 53.7°$, $\xi = 40.5°$ and $\xi = 25.0°$.

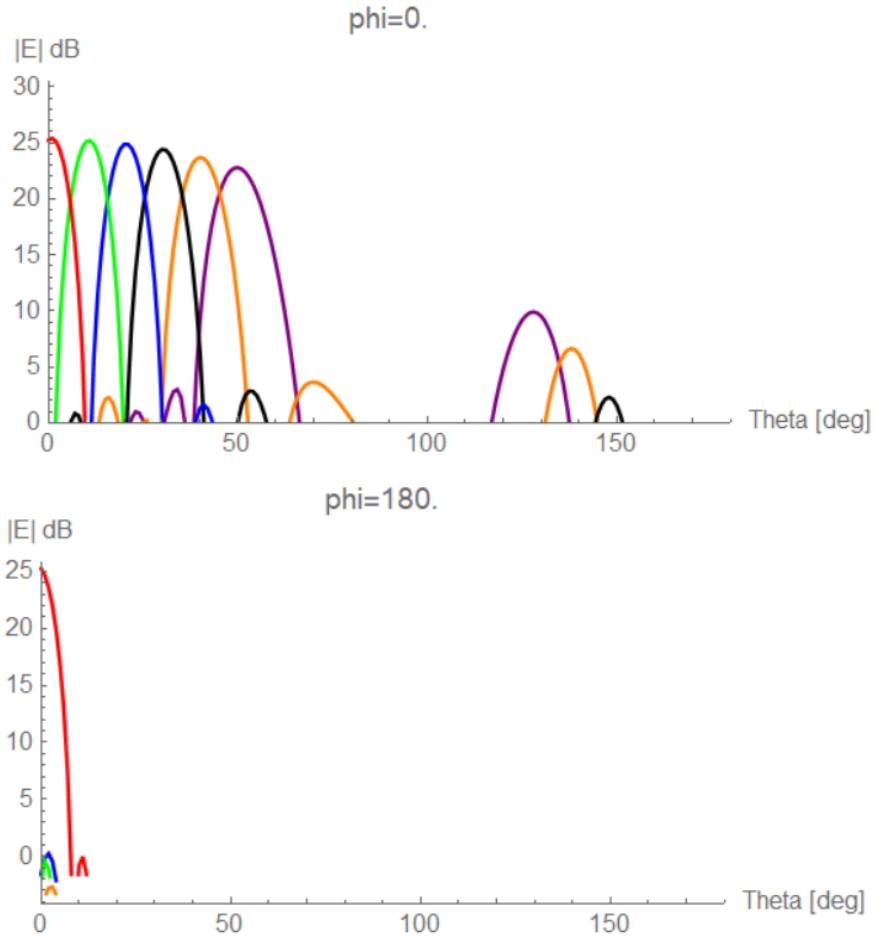

Figure 17 - $x0z$ Directivity cut of components E_θ and E_φ of the two lenses system at $f_1 = 20\,GHz$ with $F_1 = 100\,mm$, $F_2 = 150\,mm$, $d = 5\,mm$, $\sigma = 21.8°$ and $\phi = 0°$ for different values of ξ: $\xi = 90.0°$ (red), $\xi = 78.1°$ (green), $\xi = 66.1°$ (blue), $\xi = 53.7°$ (black), $\xi = 40.5°$ (orange) and $\xi = 25.0°$ (purple). The cross-polarization is so small, it is not possible to distinguish the two components

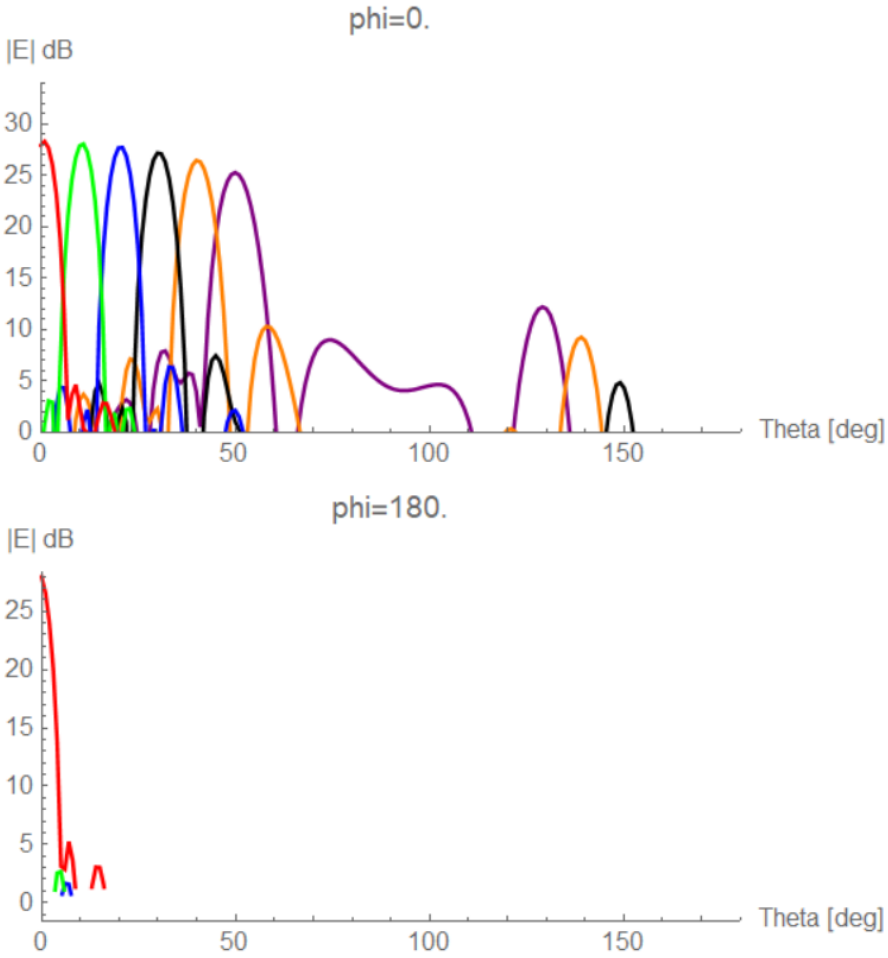

Figure 18 - $x0z$ Directivity cut of components E_θ and E_φ of the two lenses system at $f_2 = 30\ GHz$ with $F_1 = 100\ mm$, $F_2 = 150\ mm$, $d = 5\ mm$, $\sigma = 21.8°$ and $\phi = 0°$ for different values of ξ: $\xi = 90.0°$ (red), $\xi = 78.1°$ (green), $\xi = 66.1°$ (blue), $\xi = 53.7°$ (black), $\xi = 40.5°$ (orange) and $\xi = 25.0°$ (purple). The cross-polarization is so small, it is not possible to distinguish the two components

Table 7 - Beam scanning performance of the two lenses system

$\boldsymbol{\xi}$ [°]	$\boldsymbol{D_{max}}$ $[\boldsymbol{dBi}]$		$\boldsymbol{SLL}$ $[\boldsymbol{dB}]$ $(\boldsymbol{\varphi = 0°})$		$\boldsymbol{\theta_{RP}}$ [°]	$\boldsymbol{\theta_{max}}$ [°]	
	$\boldsymbol{f_1}$	$\boldsymbol{f_2}$	$\boldsymbol{f_1}$	$\boldsymbol{f_2}$		$\boldsymbol{f_1}$	$\boldsymbol{f_2}$
90.0	28.4	31.3	-25.2	-22.9	0	1	1
78.1	28.2	31.1	-25.0	-25.2	10	11	11
66.1	27.9	30.8	-23.3	-21.5	20	21	20
53.7	27.4	30.2	-21.7	-19.4	30	30	30
40.5	26.7	29.5	-16.9	-16.2	40	40	40
25.0	25.9	28.4	-13.0	-13.3	50	50	50

As expected, $\varphi = \phi = 0$ and θ_{max} is consisted with θ_{RP}, the theoretical elevation angle given by expression (12), which means that the system is performing the beam steering correctly. The Directivity decreases with θ_{max} due to the scan loss and it increases with the frequency once again.

3.4 Full-wave Analysis

There are always coupling effects between the two lenses and between nearby cells that are not considered in the previous PO/GO analysis due to some of its limitations:

a) The lenses are assumed to be independent from each other: the reflected waves and coupling effects between the lenses are not considered. Therefore, it is not possible to study the impact of the air gap thickness d;
b) The cells are assumed to be independent from each other: the coupling effects between the cells on the same lens are not accounted for;
c) The lenses are assumed to be 2-D structures: the incidence angle has no impact on the cell's response;

Therefore, it is necessary to perform a full-wave analysis, where the complete set of Maxwell's equations are solved without any simplifying assumptions, to obtain more accurate results that consider some of the previous effects. For that, it was used the CST software using the Time Domain tool and the methods mentioned before to improve the simulations efficiency. The equivalent dielectric cells were defined using the phase constants $\phi_{f_1} = -487.0°$ and $\phi_{f_2} = -658.9°$.

3.4.1 Single Equivalent Dielectric Lens

The phase distribution of the two lenses is defined by three parameters: the real feed focus distance, F_1, the virtual focus distance, F_2, and the offset elevation angle, α_0. Also, there is a fourth parameter in our system: the distance d between the lenses. For practical reasons, it was defined $F_1 = 100\,mm$ to guarantee a $Taper\ Level = -12\,dB$ using the already existing Horn feeds in the laboratory.

Previous solutions involving a Risley Prism-like rotation [7, 8] use the conventional pair of phase distributions (16) and (17) described in the previous chapter.

In this case, Lens 1 transforms the incident spherical wave into a tilted plane wave, while Lens 2 only has a tilting effect. Figure 19 presents the equivalent lenses used to simulate the conventional phase distributions (16) and (17) in CST, it is used a colour-coded system to represent the ID of each cell: two separate areas with the same colour correspond to the phase wrapping mentioned before. Although visually identical because the cell colour indicates the ID and not the phase delay, each dual-band lens is simulated using two distinct equivalent single-band lenses, one for $f_1 = 20\ GHz$ and another for $f_2 = 30\ GHz$. Figures 20 – 21 and Tables 8 – 9 show the far-field results of each one of these lenses for $\alpha_0 = 25°$ and $\alpha_0 = 30°$.

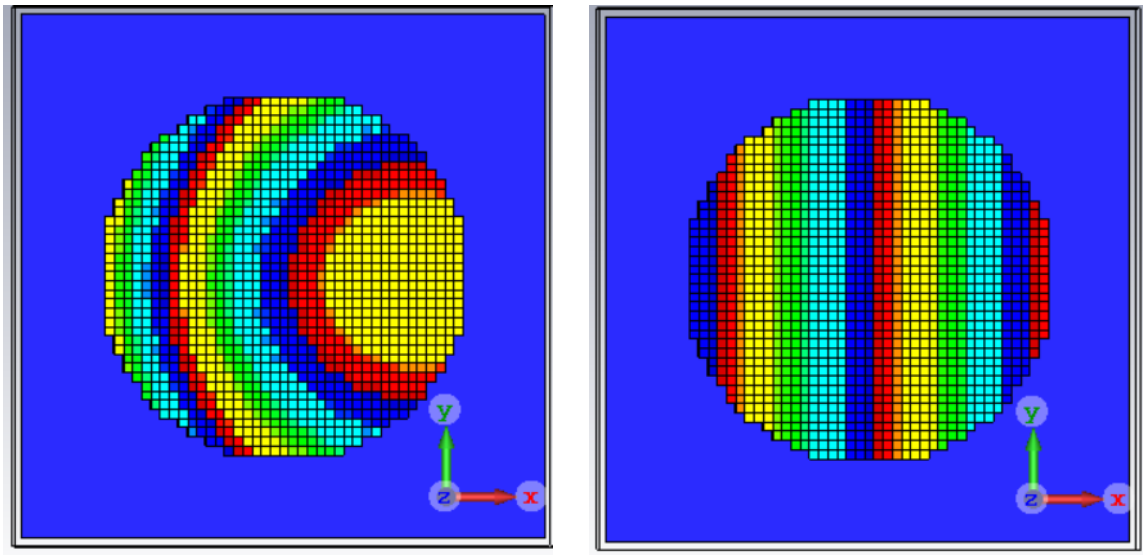

Figure 19 - Equivalent dielectric Lens 1 (left) and Lens 2 (right) defined by phase distributions (16) and (17) with $F_1 = 100\ mm$, $\alpha_0 = 25°$ and $\psi_1 = \psi_2 = 0°$. The blue screen behind each lens is the equivalent feed source

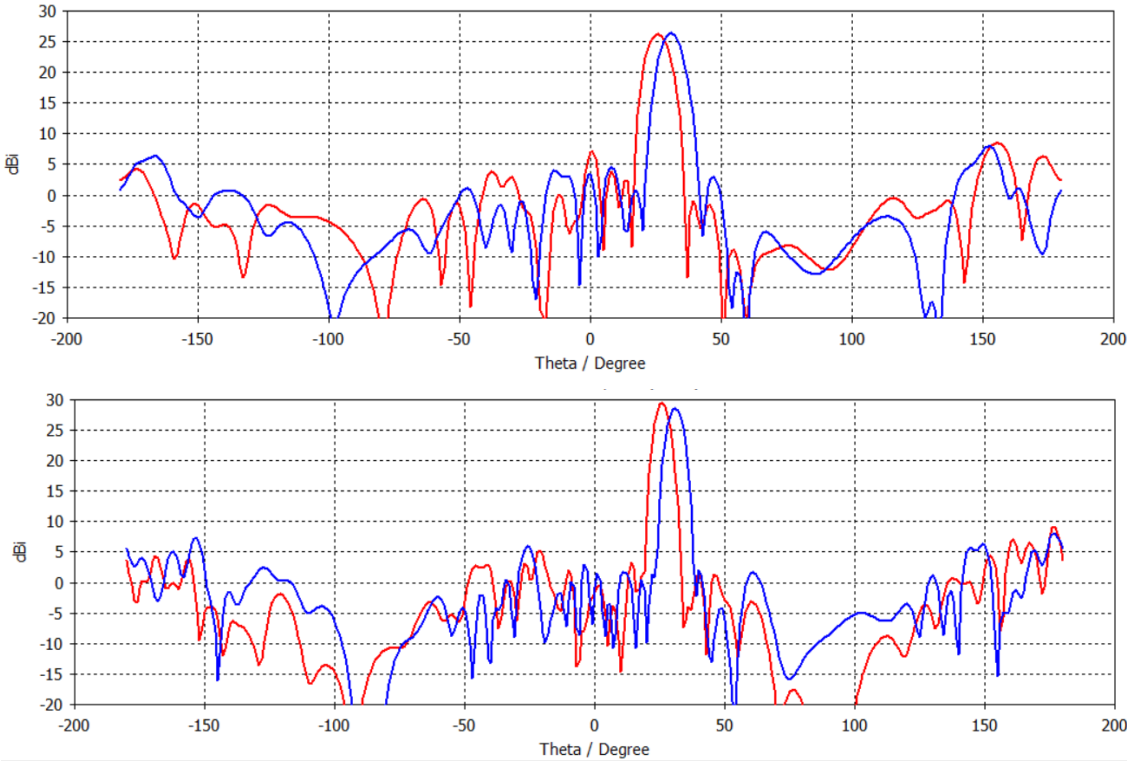

Figure 20 - $\varphi = 0°$ Directivity cut for Lens 1 at $f_1 = 20\ GHz$ (above) and $f_2 = 30\ GHz$ (below) using phase distribution (16) with $F_1 = 100\ mm$ for $\alpha_0 = 25°$ (red) and $\alpha_0 = 30°$ (blue)

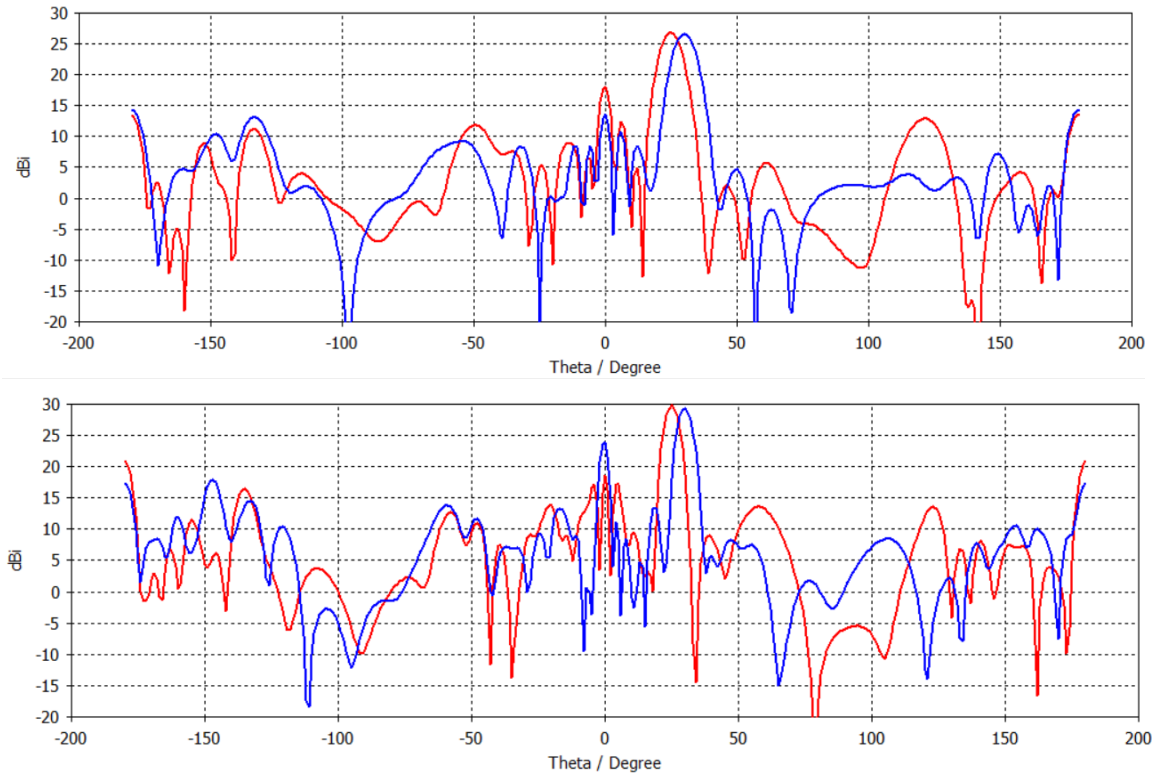

Figure 21 - $\varphi = 0°$ Directivity cut for Lens 2 at $f_1 = 20\ GHz$ (above) and $f_2 = 30\ GHz$ (below) using phase distribution (17) with $F_1 = 100\ mm$ for $\alpha_0 = 25°$ (red) and $\alpha_0 = 30°$ (blue)

Table 8 - Far-field results for Lens 1 at $f_1 = 20\ GHz$ and $f_2 = 30\ GHz$ using phase distribution (16) with $F_1 = 100\ mm$ for different values of α_0

$\boldsymbol{\alpha_0}$ [°]	$\boldsymbol{D_{max}}$ $\boldsymbol{[dBi]}$		$\boldsymbol{SLL}$ $\boldsymbol{[dB]}$		$\boldsymbol{\theta_{max}}$ [°]	
	$\boldsymbol{f_1}$	$\boldsymbol{f_2}$	$\boldsymbol{f_1}$	$\boldsymbol{f_2}$	$\boldsymbol{f_1}$	$\boldsymbol{f_2}$
25	26.2	29.5	-17.7	-20.3	26	26
30	26.4	28.6	-18.4	-20.7	31	31

Table 9 - Far-field results for Lens 2 at $f_1 = 20\ GHz$ and $f_2 = 30\ GHz$ using phase distribution (17) with $F_1 = 100\ mm$ for different values of α_0

$\boldsymbol{\alpha_0}$ [°]	$\boldsymbol{D_{max}}$ $\boldsymbol{[dBi]}$		$\boldsymbol{SLL}$ $\boldsymbol{[dB]}$		$\boldsymbol{\theta_{max}}$ [°]	
	$\boldsymbol{f_1}$	$\boldsymbol{f_2}$	$\boldsymbol{f_1}$	$\boldsymbol{f_2}$	$\boldsymbol{f_1}$	$\boldsymbol{f_2}$
25	26.8	29.7	-8.8	-8.9	25	25
30	26.5	29.4	-12.2	-5.4	30	30

Figures 20 and 21 show Lens 1 is performing as expected but Lens 2 presents transmitted and reflected side lobes with high magnitudes at $\theta = 0°$ and $\theta = 180°$, specially at $f_2 = 30\ GHz$. Since both lenses use the same set of cells, this effect must be related to the phase distributions. To better understand these results, we have studied the impact of the cell parameter P over the far-field radiation of Lens 2. Note that, unlike real metallic cells, dielectric cells do not present strong coupling effects

between them and we are using a set of cells with good transmission coefficients and phase discretization, so P is the only parameter left to improve. Figure 22 and Table 10 show these results.

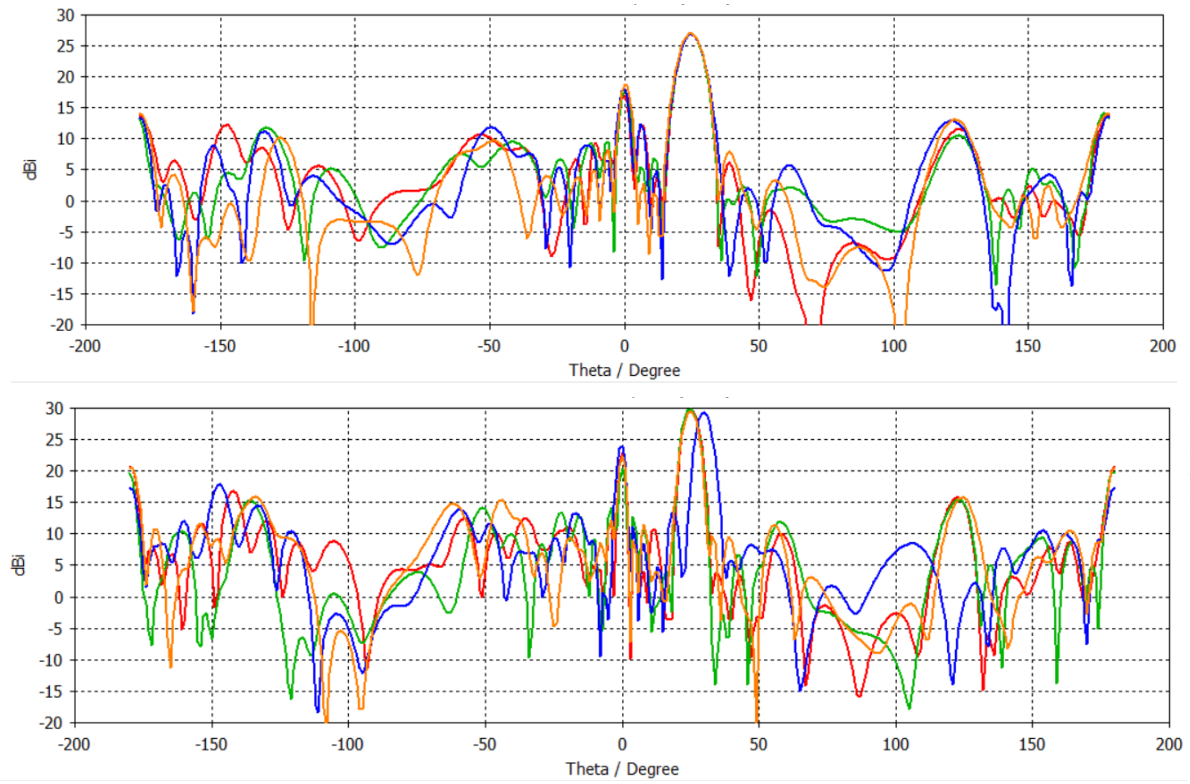

Figure 22 - $\varphi = 0°$ Directivity cut for Lens 2 at $f_1 = 20\ GHz$ (above) and $f_2 = 30\ GHz$ (below) using phase distribution (17) with $F_1 = 100\ mm$ and $\alpha_0 = 25°$ for different values of P: $P = 2.5\ mm$ (red), $P = 3.0\ mm$ (green), $P = 3.5\ mm$ (blue), $P = 4.0\ mm$ (orange)

Table 10 - Far-field results for Lens 2 at $f_1 = 20\ GHz$ and $f_2 = 30\ GHz$ using phase distribution (17) with $F_1 = 100\ mm$ and $\alpha_0 = 25°$ for different values of P. $\Delta D(\theta)$ is defined as $\Delta D(\theta) = D_{max} - D(\theta)$

P $[mm]$	**D_{max} $[dBi]$**		**ΔD ($\theta \approx 0°$) $[dB]$**		**ΔD ($\theta \approx 180°$) $[dB]$**	
	f_1	**f_2**	**f_1**	**f_2**	**f_1**	**f_2**
2.5	26.9	29.6	-9.8	-6.7	-13.1	-9.4
3.0	27.0	29.9	-9.3	-9.6	-12.8	-9.9
3.5	26.8	29.7	-8.8	-5.4	-13.5	-12.0
4.0	27.0	29.4	-8.2	-7.1	-13.1	-9.2

The best result regarding the side lobe at $\theta = 0°$ corresponds to $P = 3.0\ mm$, while for the side lobe at $\theta = 180°$ it corresponds to $P = 4.0\ mm$. The results do not improve necessarily for smaller or bigger values of P, which may indicate some sort of tuning effect involved. Our suspicion is that the equivalent surface currents are a linear combination of Floquet modes, due to the periodic nature of the phase distribution of Lens 2, with second-order effects that may generate constructive interference in some

cases like ours, originating the transmitted and reflected side lobes. Curiously, we have not found this effect mentioned in similar works, so probably it arises from some unlucky combination of phase distribution (17) and our particular set of cells, despite being a valid one. This was the motivation to explore alternative implementations of the Risley Prism concept.

3.4.2 Two Equivalent Dielectric Lenses

The new phase distributions (21) and (23) introduced in Chapter 2 appear as an alternative approach to deal with the problem discussed in the last section: the periodicity of Lens 2 disappears by creating a virtual focus which introduces a radial term. To further explore this solution, we have studied the impact of the virtual focus distance F_2 on the performance of the two lenses system using the equivalent dielectric description in CST represented in Figure 23 separated by an air gap with $d = 5\,mm$. Figures 24 – 25 and Table 11 show these results. From now on, the offset elevation angle is defined as $\alpha_0 = 25°$ because it is the best compromise between the scanning range and the Directivity as shown by Figure 3.

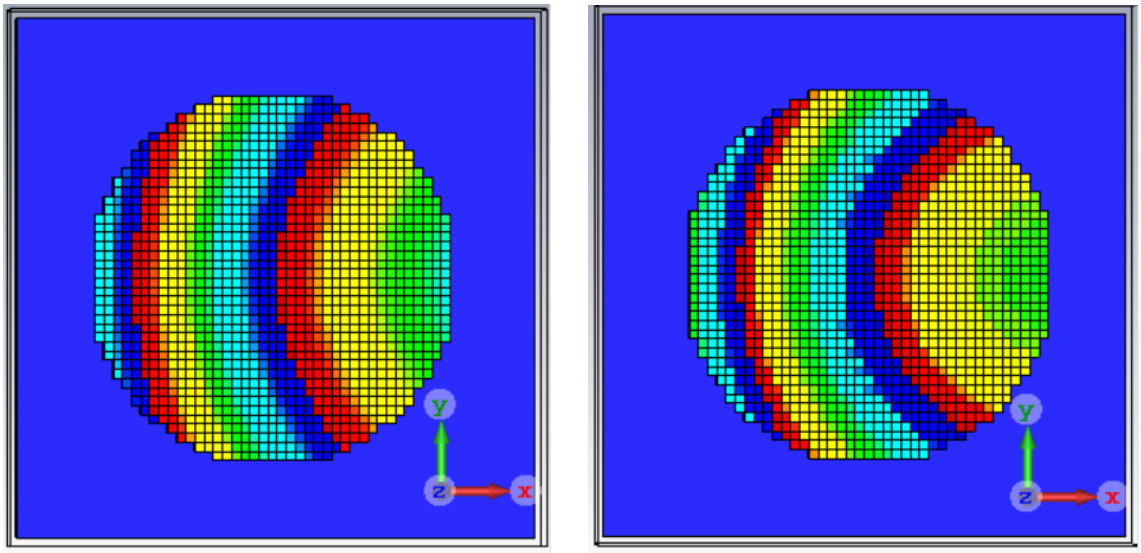

Figure 23 - Equivalent dielectric Lens 1 (left) and Lens 2 (right) defined by phase distributions (21) and (23) with $F_1 = 100\,mm$, $F_2 = 150\,mm$, $\alpha_0 = 25°$ and $\psi_1 = \psi_2 = 0°$. The blue screen behind each lens is the equivalent feed source

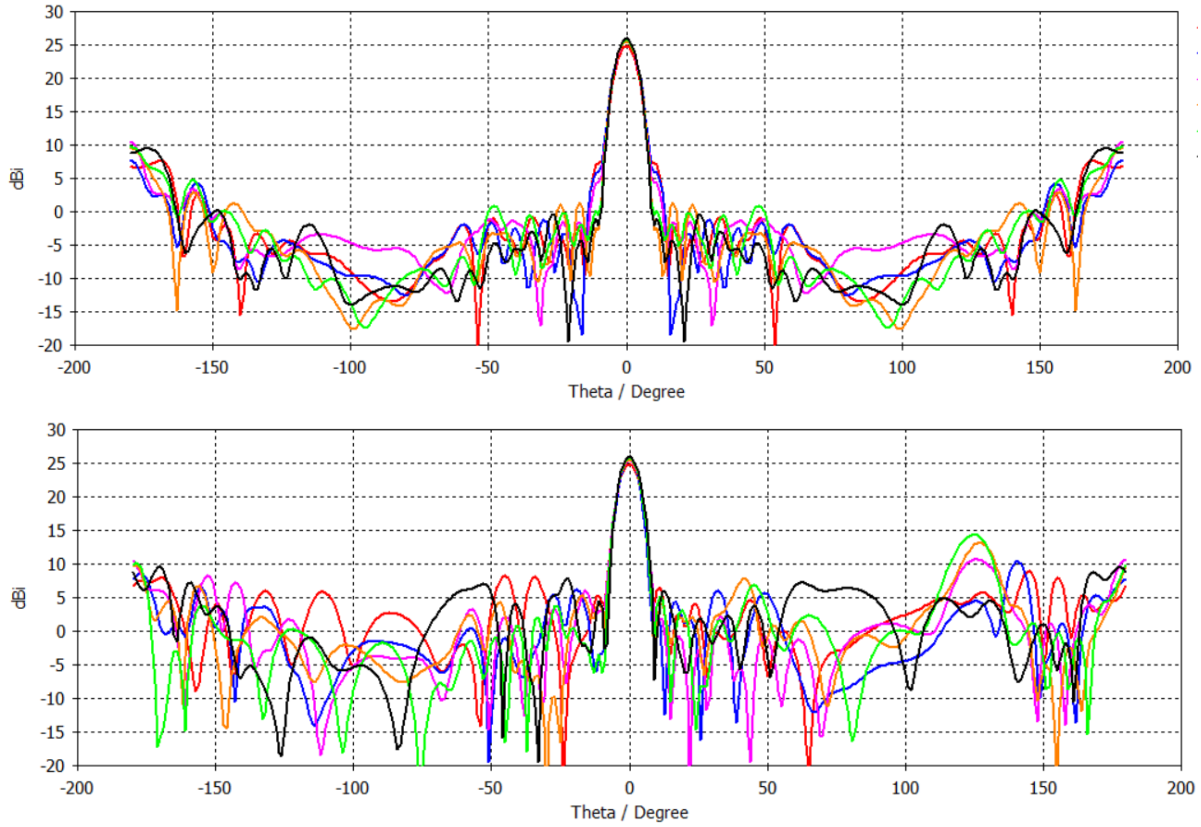

Figure 24 - $\varphi = 0°$ (above) and $\varphi = 90°$ (below) Directivity cuts for the 2 equivalent lenses system at $f_1 = 20\ GHz$ using phase distributions (21) and (23) with $F_1 = 100\ mm$, $\alpha_0 = 25°$ $d = 5\ mm$ and $\theta_{RP} = 0°$ for different values of F_2: $F_2 = 100\ mm$ (red), $F_2 = 125\ mm$ (blue), $F_2 = 150\ mm$ (purple), $F_2 = 175\ mm$ (orange), $F_2 = 200\ mm$ (green) and $F_2 \to \infty$ (black)

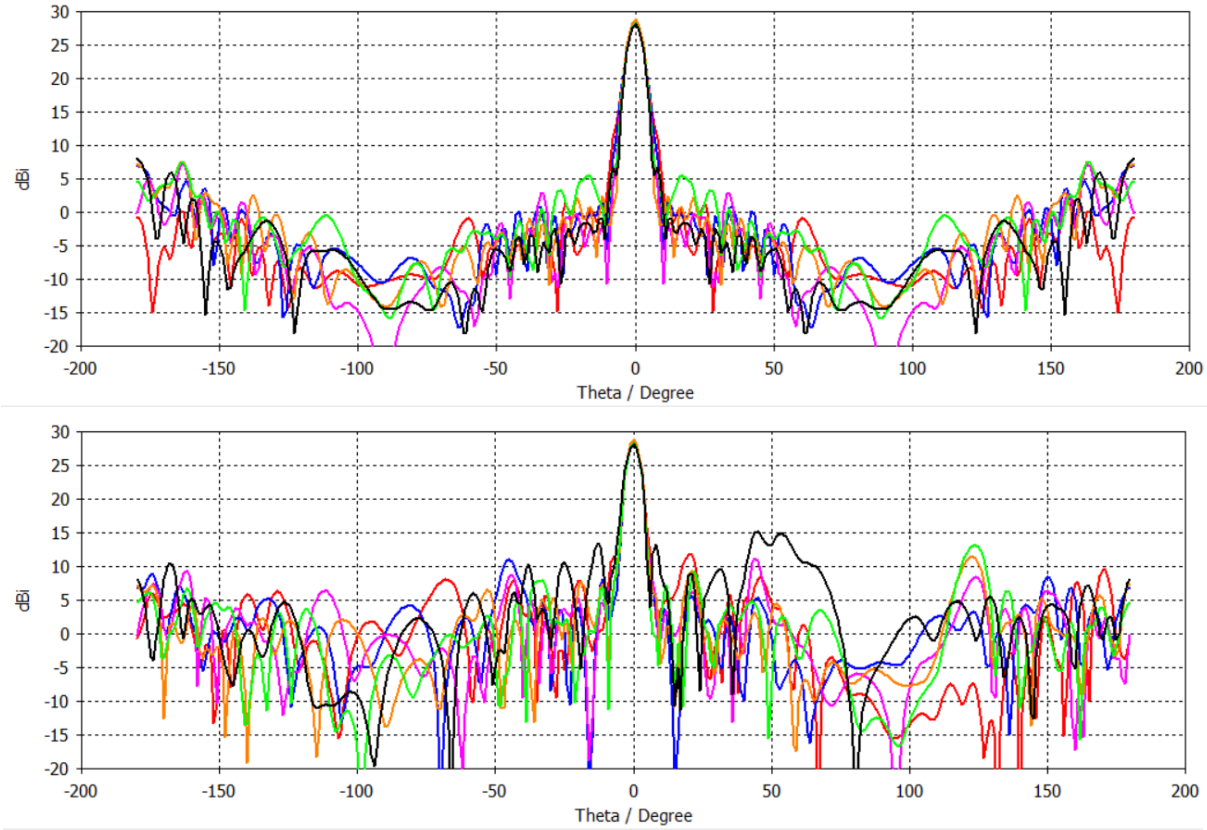

Figure 25 - $\varphi = 0°$ (above) and $\varphi = 90°$ (below) Directivity cuts for the 2 equivalent lenses system at $f_2 = 30\ GHz$ using phase distributions (21) and (23) with $F_1 = 100\ mm$, $\alpha_0 = 25°$ $d = 5\ mm$ and $\theta_{RP} = 0°$ for different values of F_2: $F_2 = 100\ mm$ (red), $F_2 = 125\ mm$ (blue), $F_2 = 150\ mm$ (purple), $F_2 = 175\ mm$ (orange), $F_2 = 200\ mm$ (green) and $F_2 \to \infty$ (black)

Table 11 - Far-field results for the 2 equivalent lenses system at $f_1 = 20\ GHz$ and $f_2 = 30\ GHz$ using phase distributions (21) and (23) with $F_1 = 100\ mm$, $\alpha_0 = 25°$, $d = 5\ mm$ and $\theta_{RP} = 0°$ for different values of F_2

$\mathbf{F_2}\ [mm]$	$D_{max}\ [dBi]$		$e_a\ [\%]$		$SLL\ [dB]$		θ_{max}	
	f_1	f_2	f_1	f_2	f_1	f_2	f_1	f_2
100	24.9	28.3	35.9	34.9	-15.9	-16.6	2	3
125	25.5	28.5	41.3	36.6	-15.2	-17.5	2	2
150	25.5	28.6	41.3	37.4	-14.8	-17.4	2	2
175	25.6	28.8	42.2	39.2	-12.4	-17.4	1	1
200	25.8	28.2	44.2	34.2	-11.5	-15.1	1	1
∞	26.0	28.1	46.3	33.4	-16.5	-12.9	1	1

$F_2 \to \infty$ corresponds to the conventional distributions (16) and (17), which means our alternative solution is a generalization of the conventional phase distributions. Table 11 confirms the Directivity and the SLL improves significantly at $f_2 = 30\ GHz$ with the virtual focus. However, the results at $f_1 = 20\ GHz$

become worse. Also, it is interesting to point out that the elevation angle error $\theta_{error} = |\theta_{RP} - \theta_{max}|$, despite being small, increases for smaller values of F_2.

We have used three criteria to determine the best solution:

a) Maximize aperture efficiency: We have chosen to maximize the aperture efficiency to consider the effect of the wavelength over the Directivity, because the same Directivity value can be good for a certain frequency and bad for another;
b) Minimize the sidelobe level: It is important to have a good SLL for $\theta_{RP} = 0°$ to guarantee that it remains low for the entire scanning range;
c) Improve the worst case between the two bands: A dual-band solution is only as good as its worst single-band performance.

After analysing Table 11, the best results correspond to $F_2 = 125\ mm$ and $F_2 = 150\ mm$ and we have chosen to use the latter because it presents the best Directivity. If we compare the results for $F_2 = 150\ mm$ with the ones for $F_2 \to \infty$, the Directivity decreases $0.5\ dB$ and the SLL increases $1.7\ dB$ at $f_1 = 20\ GHz$, but the Directivity increases $0.5\ dB$ and the SLL improves $4.5\ dB$ at $f_2 = 30\ GHz$. Curiously, $F_2 = 100\ mm$ corresponds to (16) and (17) if we switch the order of the lenses and the results at $f_2 = 30\ GHz$ improve as well. It seems that Lens 1 transmitting a spherical wave, instead of a plane wave, makes the side lobe energy spread out, explaining the impact over the SLL.

Finally, the only parameter left to define is the air gap thickness d between the two lenses. Figures 26 – 27 and Table 12 show the results for different values of d.

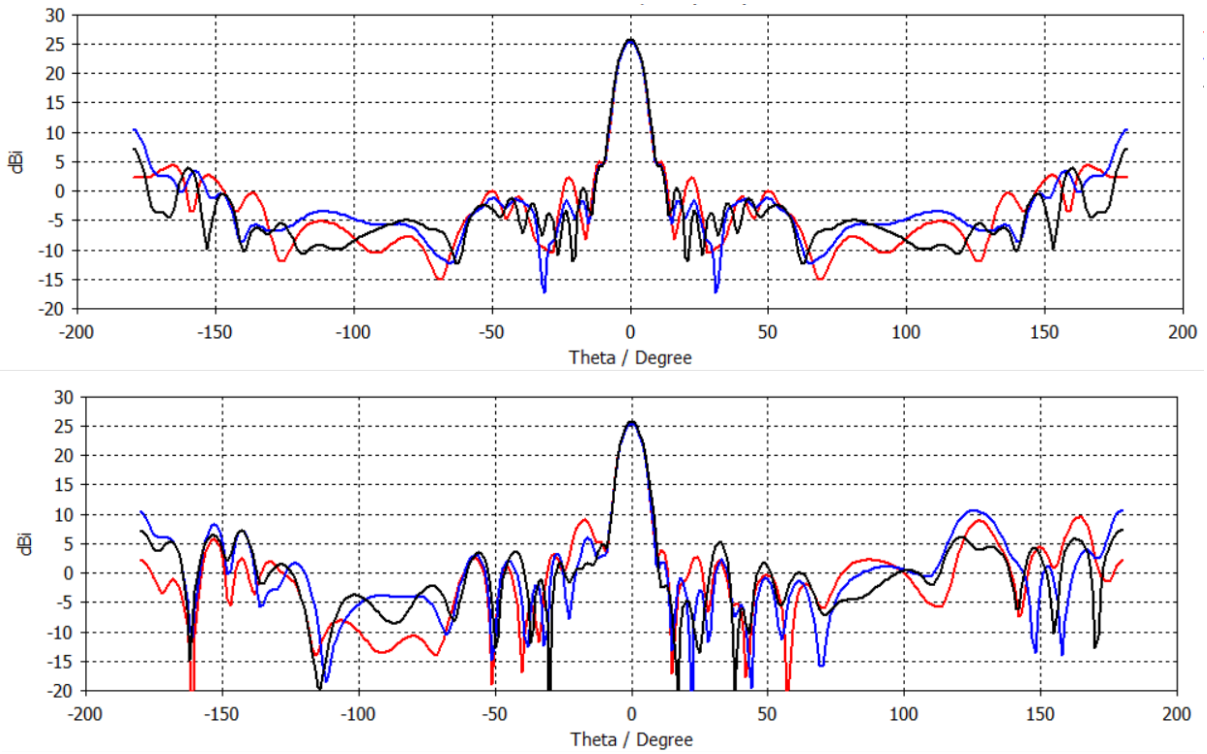

Figure 26 - $\varphi = 0°$ (above) and $\varphi = 90°$ (below) Directivity cuts for the 2 equivalent lenses system at $f_1 = 20\ GHz$ using phase distributions (21) and (23) with $F_1 = 100\ mm$, $F_2 = 150\ mm$, $\alpha_0 = 25°$ and $\theta_{RP} = 0°$ for different values of d: $d = 2.5\ mm$ (red), $d = 5.0\ mm$ (blue) and $d = 7.5\ mm$ (black)

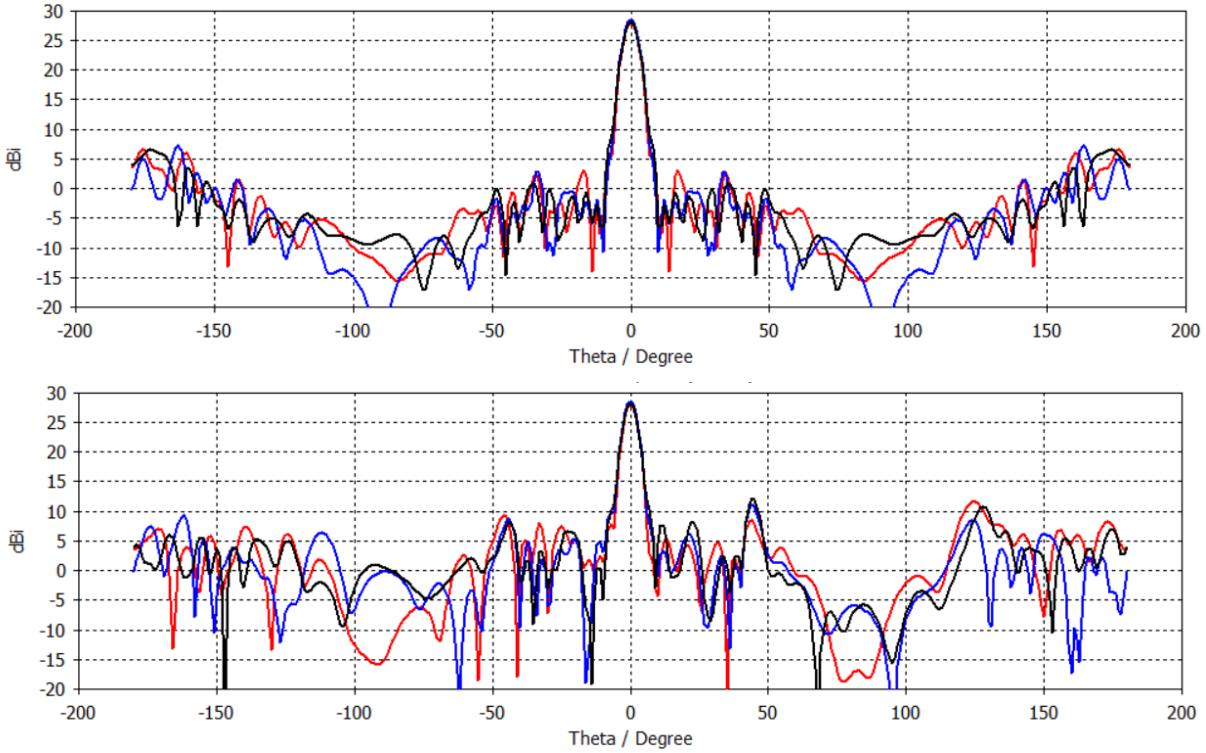

Figure 27 - $\varphi = 0°$ (above) and $\varphi = 90°$ (below) Directivity cuts for the 2 equivalent lenses system at $f_2 = 30\ GHz$ using phase distributions (21) and (23) with $F_1 = 100\ mm$, $F_2 = 150\ mm$, $\alpha_0 = 25°$ and $\theta_{RP} = 0°$ for different values of d: $d = 2.5\ mm$ (red), $d = 5.0\ mm$ (blue) and $d = 7.5\ mm$ (black)

Table 12 - Far-field results for the 2 equivalent lenses system at $f_1 = 20\ GHz$ and $f_2 = 30\ GHz$ using phase distributions (21) and (23) with $F_1 = 100\ mm$, $F_2 = 150\ mm$, $\alpha_0 = 25°$ and $\theta_{RP} = 0°$ for different values of d

$d\ [mm]$	$D_{max}\ [dBi]$		$e_a\ [\%]$		$SLL\ [dB]$	
	f_1	f_2	f_1	f_2	f_1	f_2
2.5	25.8	27.8	44.2	31.1	-16.2	-16.3
5.0	25.5	28.6	41.3	37.4	-14.8	-17.4
7.5	25.8	28.1	44.2	33.4	-18.5	-15.8

Using the same criteria mentioned before, the best results correspond to $d = 5.0\ mm$.

We have also compared our solution for $\theta_{RP} = 0°$ with the case of a single lens with the same diameter D that collimates the incident spherical wave without any tilt (i.e. lens with phase distribution (16) for $\alpha_0 = 0°$) using the same set of equivalent dielectric cells as represented in Figure 28. Figures 29 – 30 and Table 13 show the far-field results.

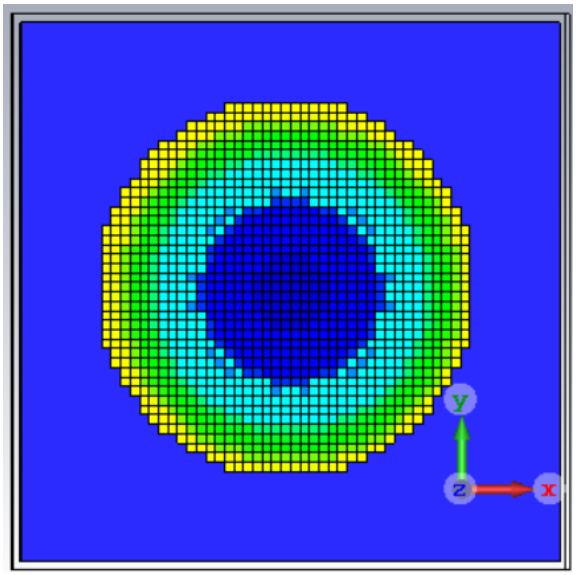

Figure 28 - Single equivalent dielectric collimating lens. The blue screen behind the lens is the equivalent feed source

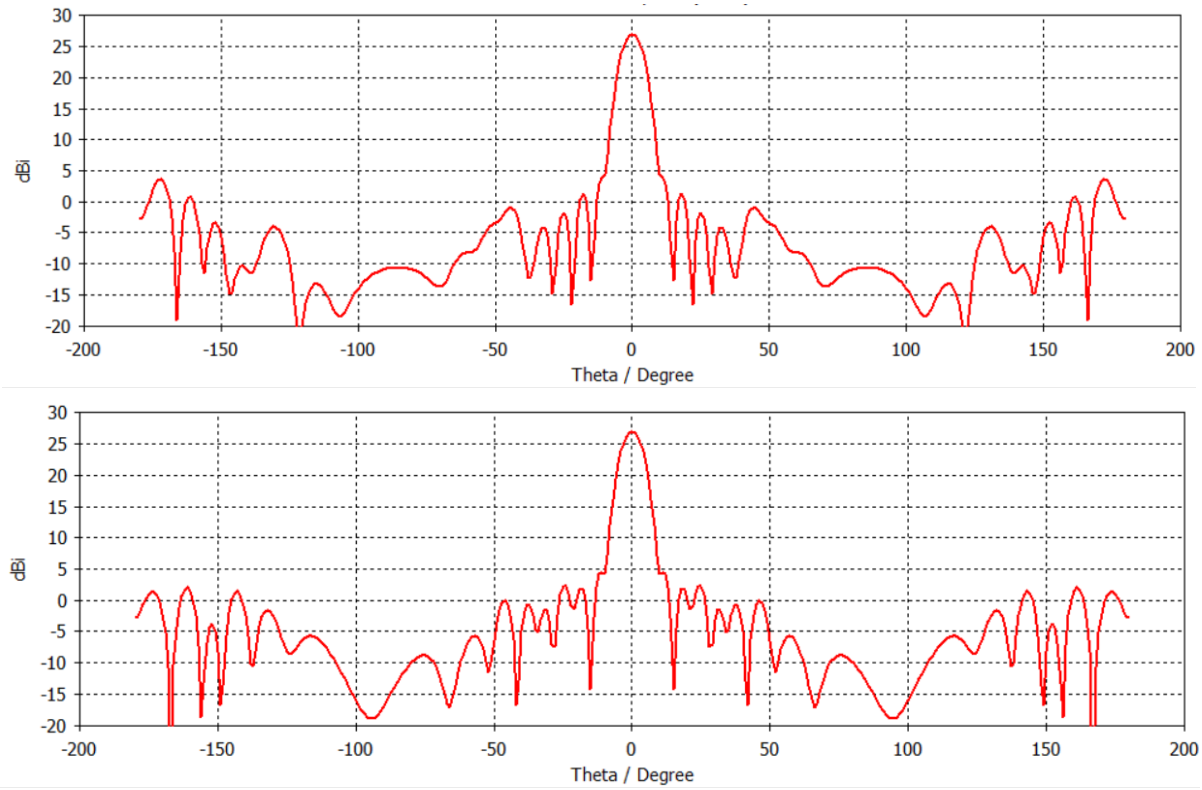

Figure 29 - $\varphi = 0°$ (above) and $\varphi = 90°$ (below) Directivity cuts for the single equivalent dielectric collimating lens at $f_1 = 20\ GHz$

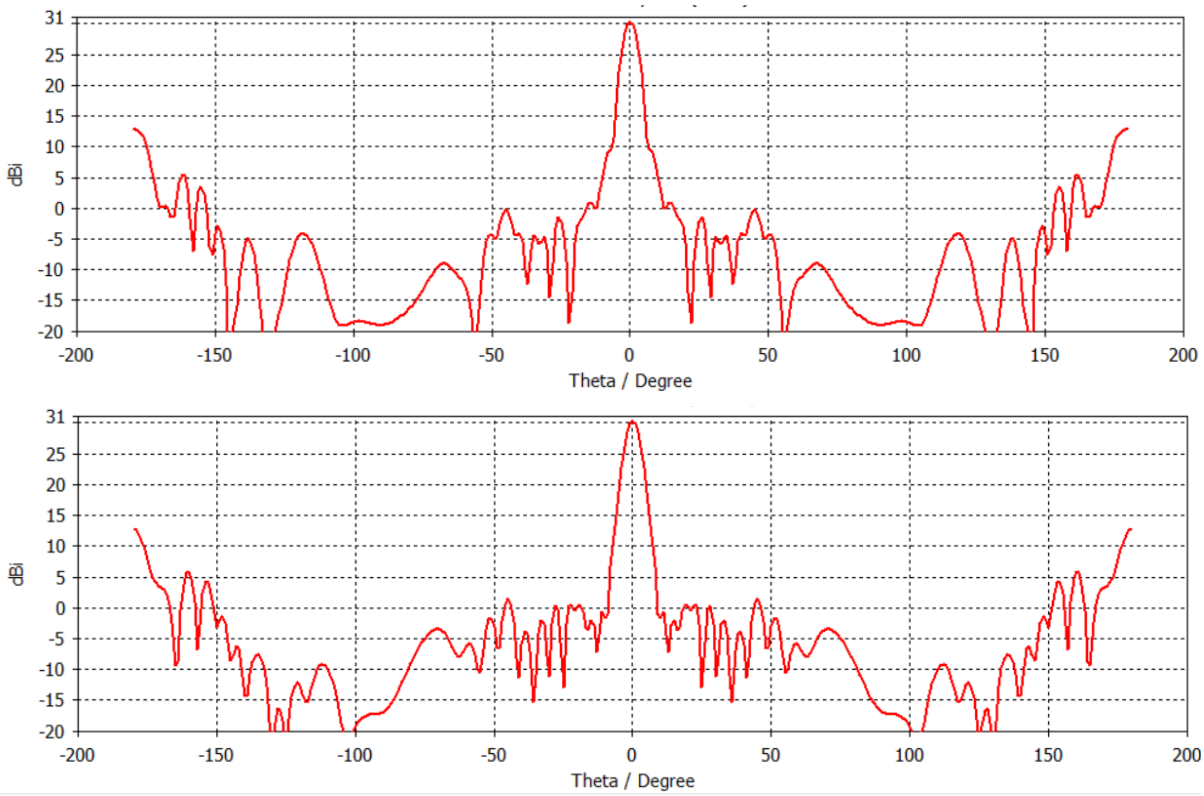

Figure 30 - $\varphi = 0°$ (above) and $\varphi = 90°$ (below) Directivity cuts for the single equivalent dielectric collimating lens at $f_2 = 30\ GHz$

Table 13 - Far-field results comparison for the single collimating lens and the two lenses system at $f_1 = 20\ GHz$ and $f_2 = 30\ GHz$

Number of lenses	D_{max} $[dBi]$		e_a [%]		SLL $[dB]$	
	f_1	f_2	f_1	f_2	f_1	f_2
1	27.0	30.3	58.3	55.4	-22.7	-17.6
2	25.5	28.6	41.3	37.4	-14.8	-17.4

As expected, there is a loss associated with the system having two lenses instead of just one: 17.0 % for $f_1 = 20\ GHz$ and 18.0% for $f_2 = 30\ GHz$.

3.4.3 Final Equivalent Dielectric Lenses Design

After defining all the parameters of our system, it is necessary to evaluate the scanning performance of our system. The system's scanning range is defined as the elevation angle range where two criteria are satisfied simultaneously: the scan loss should be smaller or equal than $-3\ dB$ and $SLL \leq -10\ dB$. The results are represented in Figure 31 and Table 14. Figure 32 and Table 15 show the results using the conventional phase distributions (16) and (17) for comparison.

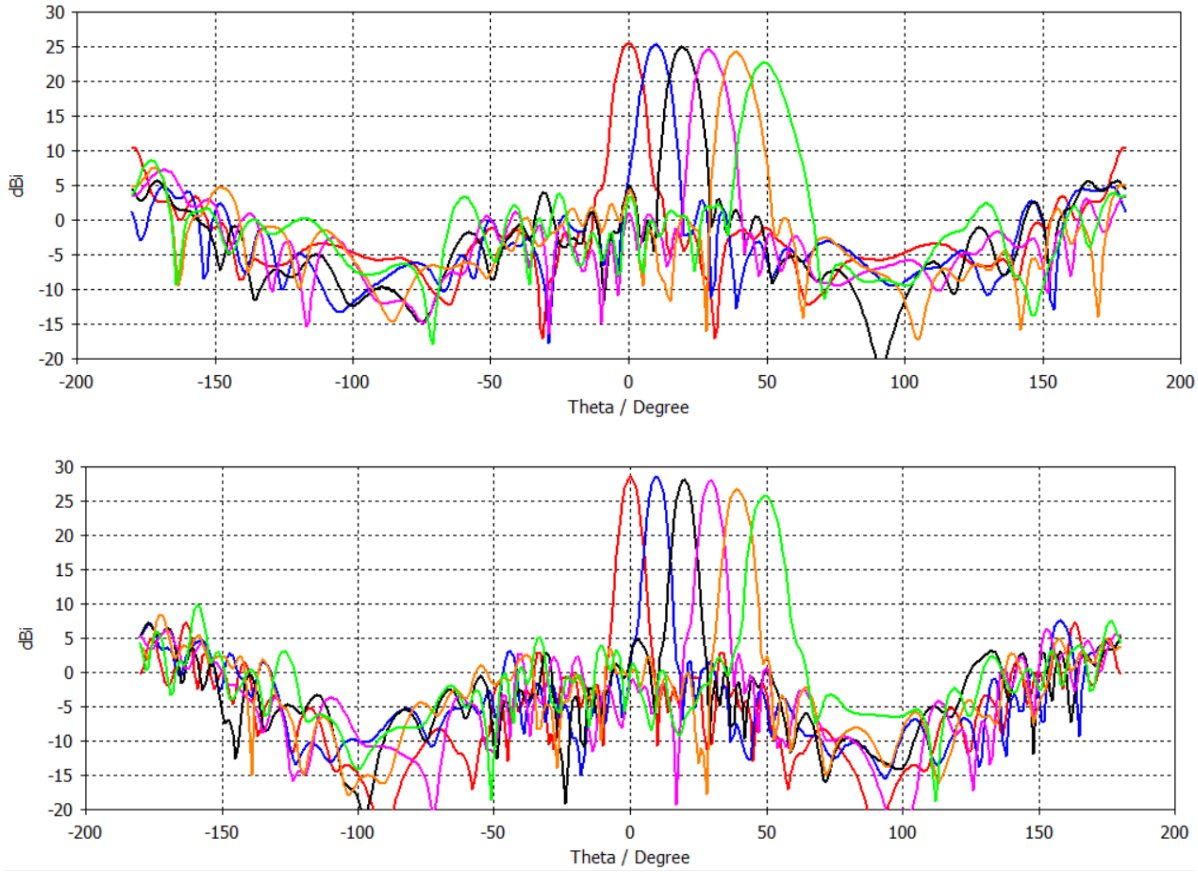

Figure 31 - Scanning performance of the 2 equivalent lenses system at $f_1 = 20\ GHz$ (above) and $f_2 = 30\ GHz$ (below) using phase distributions (21) and (23) with $F_1 = 100\ mm$, $F_2 = 150\ mm$, $\alpha_0 = 25°$ and $d = 5\ mm$ for different scanning angles: $\theta_{RP} = 0°$ (red), $\theta_{RP} = 10°$ (blue), $\theta_{RP} = 20°$ (black), $\theta_{RP} = 30°$ (purple), $\theta_{RP} = 40°$ (orange) and $\theta_{RP} = 50°$ (green)

Table 14 - Scanning performance of the 2 equivalent lenses system at $f_1 = 20\ GHz$ and $f_2 = 30\ GHz$ using the new phase distributions (21) and (23) with $F_1 = 100\ mm$, $F_2 = 150\ mm$, $\alpha_0 = 25°$ and $d = 5\ mm$

θ_{RP} [°]	D_{max} [dBi]		SLL [dB]		θ_{max} [°]		φ_{max} [°]	
	f_1	f_2	f_1	f_2	f_1	f_2	f_1	f_2
0	25.5	28.6	-14.8	-17.4	2	2	-90	-90
10	25.3	28.6	-13.5	-19.5	10	10	-11	-9
20	24.9	28.2	-13.8	-19.5	19	20	-5	-5
30	24.6	28.0	-12.8	-19.5	29	29	-3	-3
40	24.3	26.7	-12.4	-17.6	39	39	-2	-2
50	22.7	25.7	-11.1	-15.3	49	49	-2	-2

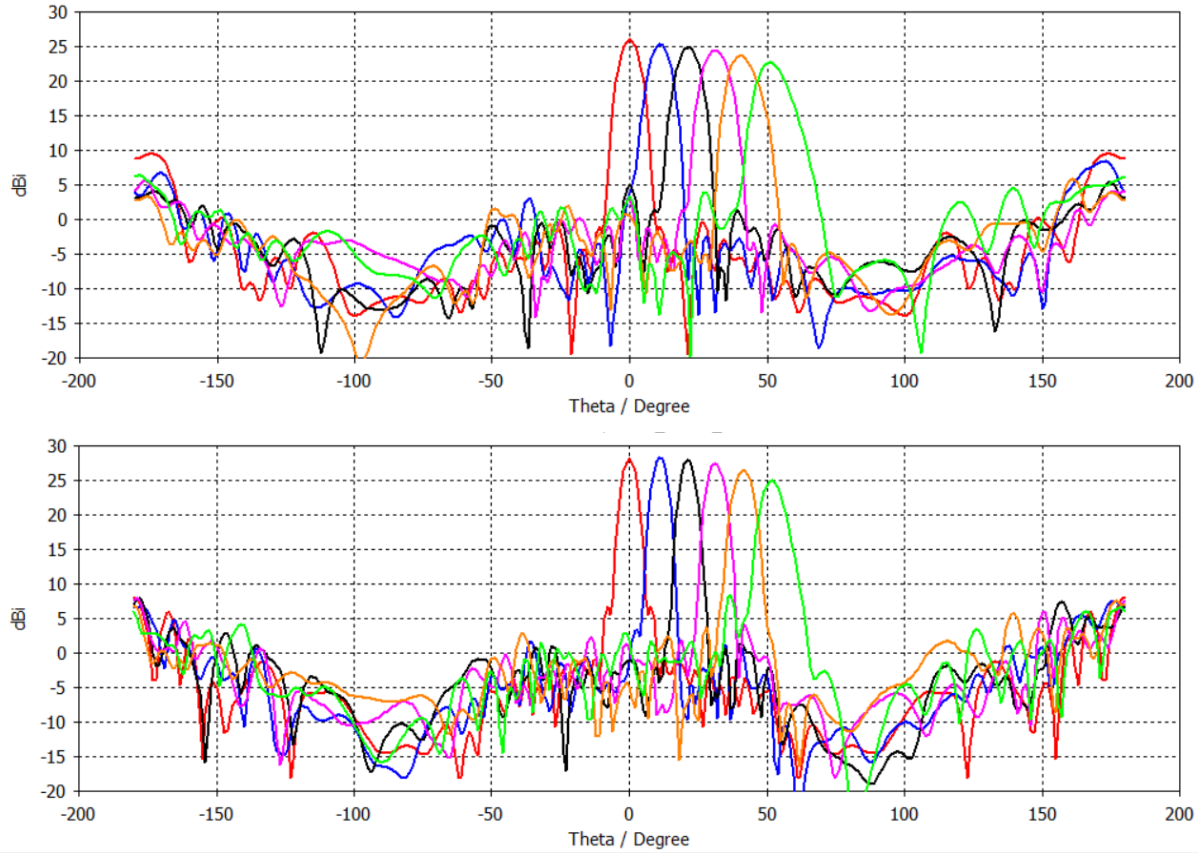

Figure 32 - Scanning performance of the 2 equivalent lenses system at $f_1 = 20\ GHz$ (above) and $f_2 = 30\ GHz$ (below) using the conventional phase distributions (16) and (17) with $F_1 = 100\ mm$, $\alpha_0 = 25°$ and $d = 5\ mm$ for different scanning angles: $\theta_{RP} = 0°$ (red), $\theta_{RP} = 10°$ (blue), $\theta_{RP} = 20°$ (black), $\theta_{RP} = 30°$ (purple), $\theta_{RP} = 40°$ (orange) and $\theta_{RP} = 50°$ (green)

Table 15 - Scanning performance of the 2 equivalent lenses system at $f_1 = 20\ GHz$ and $f_2 = 30\ GHz$ using the conventional phase distributions (16) and (17) with $F_1 = 100\ mm$, $\alpha_0 = 25°$ and $d = 5\ mm$

θ_{RP} [°]	D_{max} [dBi]		SLL [dB]		θ_{max} [°]		φ_{max} [°]	
	f_1	f_2	f_1	f_2	f_1	f_2	f_1	f_2
0	26.0	28.1	-16.5	-12.9	1	1	90	90
10	25.3	28.4	-16.7	-13.4	11	11	4	3
20	24.9	28.0	-17.0	-12.5	21	21	2	1
30	24.4	27.4	-16.8	-13.7	31	31	1	1
40	23.6	26.5	-13.1	-11.2	40	42	0	0
50	22.7	25.0	-9.3	-10.8	51	52	-1	0

The SLL values from Tables 14 and 15 do not correspond to Figures 31 and 32 because the most prominent side lobes are not aligned with the main lobe direction. At $\theta_{max} \approx 50°$, our solution has a scan loss of $-2.8\ dB$ and a $SLL = -11.1\ dB$ at $f_1 = 20\ GHz$ and a scan loss of $-2.9\ dB$ and a $SLL = -15.3\ dB$ at $f_2 = 30\ GHz$, so the scanning range is $[-50°, 50°]$. On the other hand, at $\theta_{max} \approx 50°$, the system using the conventional phase distributions has a scan loss of $-3.3\ dB$ and a $SLL = -9.3\ dB$ at $f_1 = 20\ GHz$

and a scan loss of $-3.1\,dB$ and a $SLL = -10.8\,dB$ at $f_2 = 30\,GHz$, so the scanning range is only $\theta \in [-40°, 40°]$. Also, at $\theta_{max} \approx 50°$, our system has the same Directivity as the conventional solution at $f_1 = 20\,GHz$ and a $0.7\,dB$ gain at $f_2 = 30\,GHz$, besides a significant improvement regarding the SLL. Therefore, our solution presents better results than the conventional system. Table 16 compares the main results from the two implementations.

Table 16 – Simulated far-field results comparison between the two lenses systems with an equivalent dielectric description using the conventional phase distributions (16) and (17) and the new (21) and (23)

Pair of Phase Distributions	$\boldsymbol{D_{max}}$ $[\boldsymbol{dBi}]$ $(\boldsymbol{\theta_{RP}} = \mathbf{0}°)$		$\boldsymbol{SLL}$ $[\boldsymbol{dB}]$ $(\boldsymbol{\theta_{RP}} = \mathbf{0}°)$		$\boldsymbol{Scan\ Loss}$ $[\boldsymbol{dB}]$ $(\boldsymbol{\theta_{RP}} = \mathbf{50}°)$		$\boldsymbol{SLL}$ $[\boldsymbol{dB}]$ $(\boldsymbol{\theta_{RP}} = \mathbf{50}°)$	
	$\boldsymbol{f_1}$	$\boldsymbol{f_2}$	$\boldsymbol{f_1}$	$\boldsymbol{f_2}$	$\boldsymbol{f_1}$	$\boldsymbol{f_2}$	$\boldsymbol{f_1}$	$\boldsymbol{f_2}$
Conventional	26.0	28.1	-16.5	-12.9	-3.3	-3.1	-9.3	-10.8
Alternative	25.5	28.6	-14.8	-17.4	-2.8	-2.9	-11.1	-15.3

Even though both systems present a shift regarding the azimuth direction of the main lobe φ_{max}, this is not problematic because that can always be corrected by controlling the mean rotation angle ϕ.

3.4.4 Final Real Lenses Design

We have studied our system using an equivalent dielectric description of the two lenses and, although it has been shown to provide accurate results [26], there are coupling effects between cells from the same lens and between the two lenses that cannot be described by dielectric cells. Therefore, the previous analysis must be confirmed using the real dual-band PD cells shown in Figure 33. The diameter $D = 148\,mm$ is slightly larger than the one used in the equivalent lenses due to the extra dielectric in the border.

We have simulated the two lenses system for $\theta_{RP} = 0°$ and the best results appear at $f_1 = 20.3\,GHz$ and $f_2 = 29.9\,GHz$. Figures 34 – 35 and Table 17 show these results.

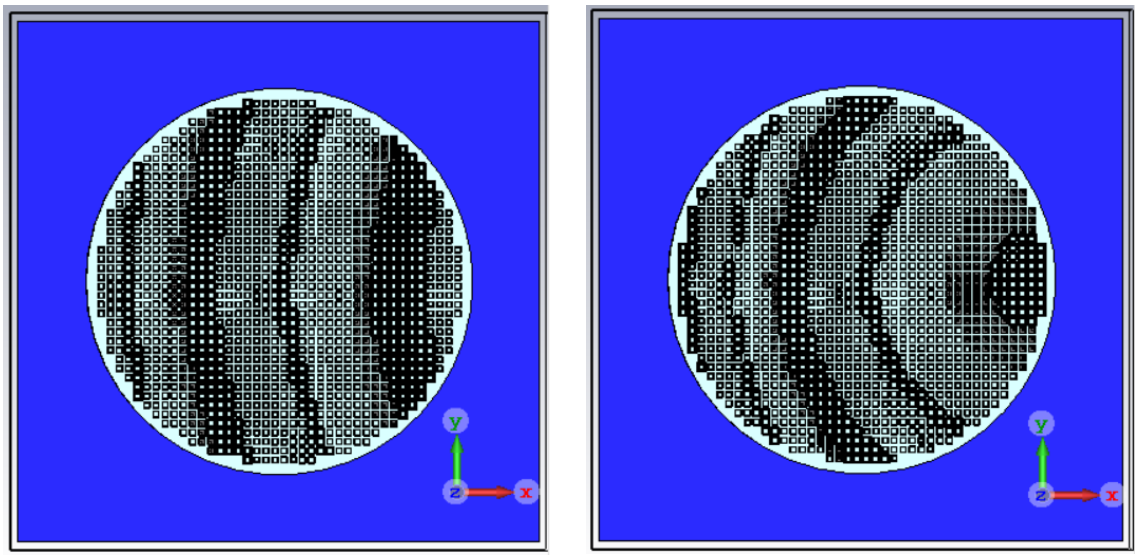

Figure 33 - Real Lens 1 (left) and Lens 2 (right) defined by phase distributions (21) and (23) for $F_1 = 100\ mm$, $F_2 = 150\ mm$, $\alpha_0 = 25°$ and $\psi_1 = \psi_2 = 0°$. The dielectric layers are coloured in light green and the metallic layers are coloured in dark grey. The blue screen behind each lens is the equivalent feed source

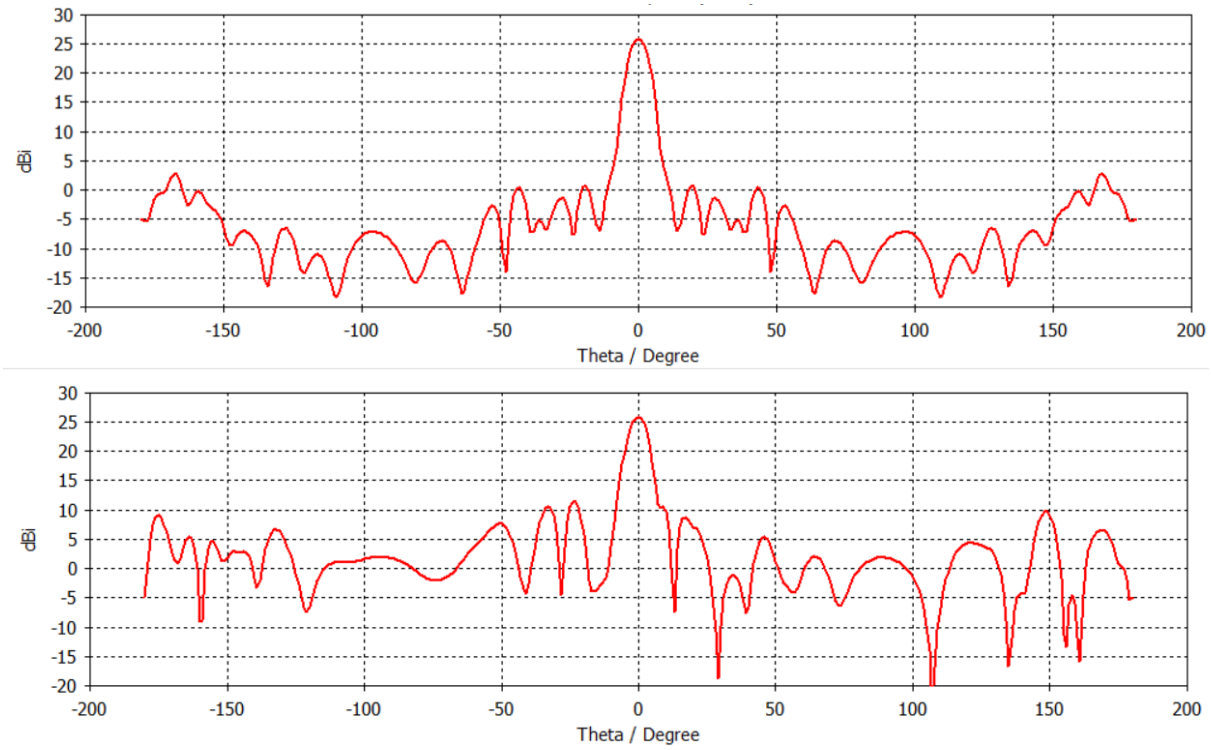

Figure 34 - $\varphi = 0°$ (above) and $\varphi = 90°$ (below) Directivity cuts for the two real lenses at $f_1 = 20.3\ GHz$ using phase distributions (21) and (23) with $F_1 = 100\ mm$, $F_2 = 150\ mm$, $\alpha_0 = 25°$, $d = 5\ mm$ and $\theta_{RP} = 0°$

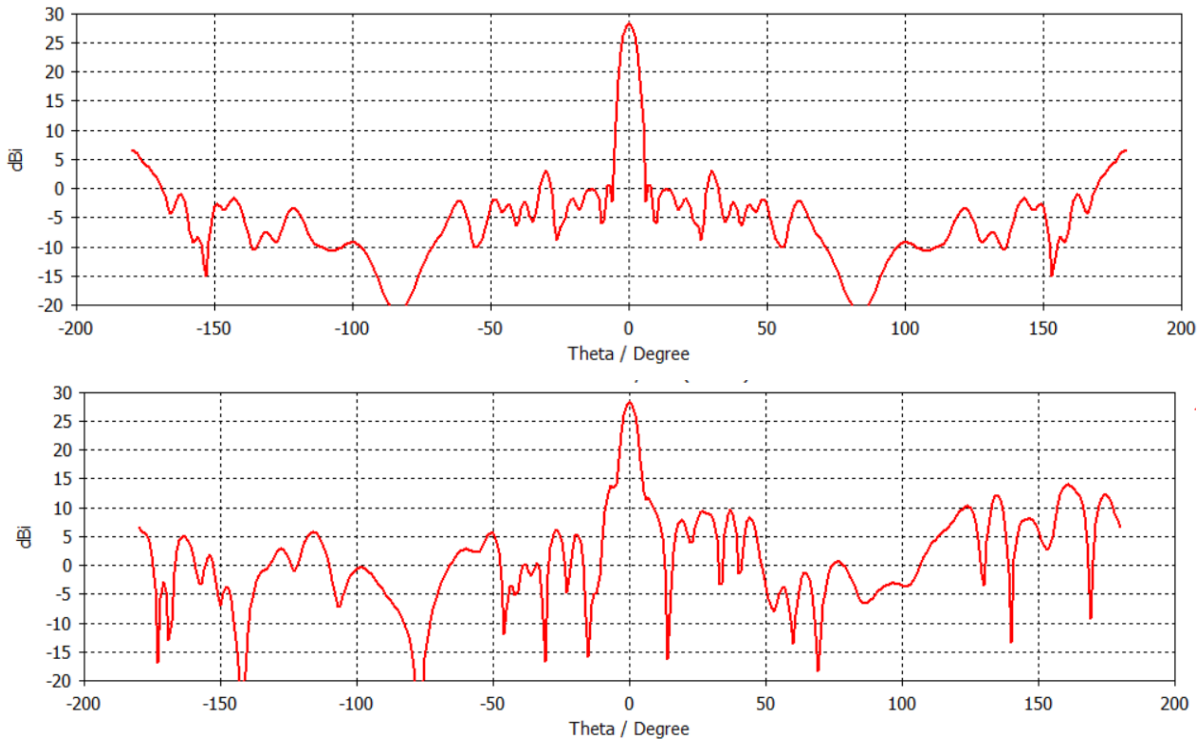

Figure 35 - $\varphi = 0°$ (above) and $\varphi = 90°$ (below) Directivity cuts for the two real lenses at $f_1 = 29.9\ GHz$ using phase distributions (21) and (23) with $F_1 = 100\ mm$, $F_2 = 150\ mm$, $\alpha_0 = 25°$, $d = 5\ mm$ and $\theta_{RP} = 0°$.

Table 17 - Far-field results comparison for the 2 real and equivalent lenses system at both bands using phase distributions (21) and (23) with $F_1 = 100\ mm$, $F_2 = 150\ mm$, $\alpha_0 = 25°$, $d = 5\ mm$ and $\theta_{RP} = 0°$

Lenses	D_{max} $[dBi]$		SLL $[dB]$		θ_{max} [°]	
	f_1	f_2	f_1	f_2	f_1	f_2
Equivalent	25.5	28.6	-14.8	-17.4	2	2
Real	25.9	28.3	-14.4	-14.4	1	1

The results from the real description are very similar to the ones obtained for the equivalent description (see Table 12), thereby validating the previous analysis. We have only used the $\theta_{RP} = 0°$ scenario to explore the symmetry regarding the $y0z$ plane, which significantly reduces the simulation time. Even for this special case, the simulation time was 37 hours due to the very thin Mesh.

It is not possible to directly calculate the gain of the antenna in CST using equivalent feed sources, so the losses associated with the lenses were determined by comparing the total radiated power (TRP) from the equivalent feed source with and without the rotary system shown in Figure 36.

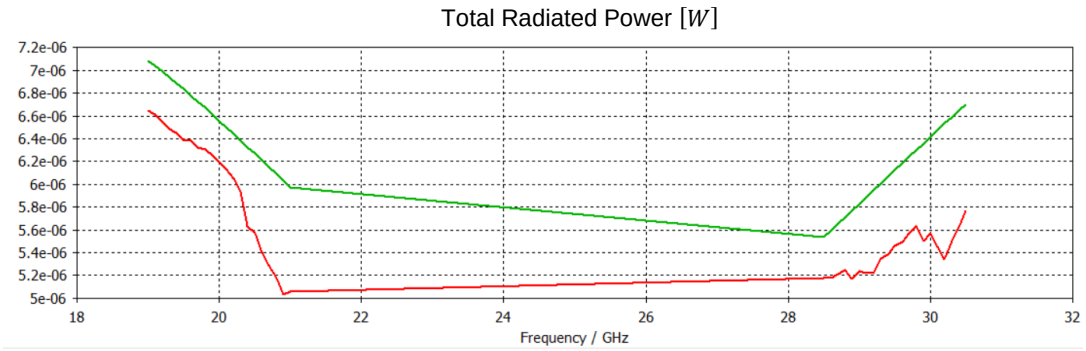

Figure 36 - Total radiated power from the equivalent feed source with (red) and without (green) the rotary system

The power gain is defined as $G = eD_{max}$, where e is the antenna efficiency associated with loss. Therefore, e can be calculated as the ratio between the TRP with and without the rotary system, because the only possible source of loss is system itself. Table 18 shows the total radiated power and antenna efficiency at $f_1 = 20.3\ GHz$ and $f_2 = 29.9\ GHz$.

Table 18 – Total radiated power and antenna efficiency at $f_1 = 20.3\ GHz$ and $f_2 = 29.9\ GHz$

Quantity	$\boldsymbol{f_1 = 20.3\ GHz}$	$\boldsymbol{f_2 = 29.9\ GHz}$
TRP with rotary system $[\mu W]$	5.94	6.36
TRP without rotary system $[\mu W]$	6.38	5.5
$e\ [dB]$	-0.3	-0.6

Therefore, the power gain is $G = 23.6\ dBi$ at $f_1 = 20.3\ GHz$ and $G = 27.7\ dBi$ at $f_2 = 29.9\ GHz$.

3.5 Experimental Setup

The simulation results shown previously must be compared with experimental results. For that purpose, a prototype is being built and tested using a radio-frequency anechoic chamber, so this experimental validation is not yet available. This section is intended to present the experimental setup that is going to be used.

Each one of the transmit arrays consists in 5 metallic layers interleaved with 4 dielectric layers. The metallic layers are made of copper and its thickness is $h_i = 0.017\ mm$. The dielectric layers are made of Rogers RT/Duroid 5880 and its thickness is $h = 0.787\ mm$. Therefore, the prototype uses 2 circular transmit arrays with a diameter $D = 148\ mm$ and a total thickness $t = 3.233\ mm$.

Each one of the metallic layers is fabricated as a printed circuit using the photolithography technique. First, a mask is created using the ABViewer software [30] as a 2D section cut of the layer from the CST

model. Figure 37 shows an example of a mask, where the metallic components are represented in black and there are also some additional marks useful for the transmit array assembly.

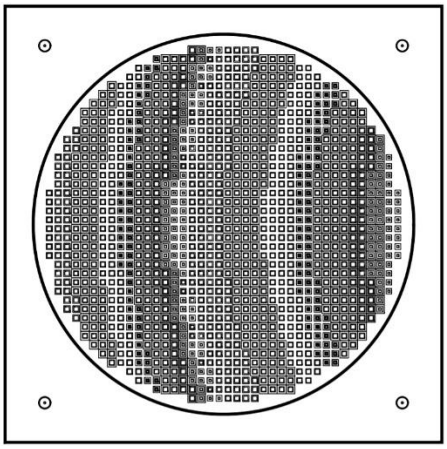

Figure 37 – Circuit mask of layer 2 from TA_1. The metallic components are represented in black and there are some additional marks useful for the transmit array assembly

This circuit mask is printed in a transparent film and placed over a copper sheet with thickness h_i that was previously cleaned, photo-varnished and dried. The photo-varnish is light-sensitive and acts as a photoresist so, when the copper sheet is exposed to an intense light source, the varnish that is not covered by the black ink of the mask is erased after being developed. The copper sheet is then taken to an acid bath: the varnish left is resistant to the acid and the naked metal surfaces are dissolved. The photo-varnish is later removed, and the circuit stays printed in the copper sheet.

Finally, the copper layers are "glued" to the dielectric layers with thickness $h = 0.787\ mm$. The additional marks in Figure 37 are used to align the different layers. Finally, the excessive dielectric is cut creating the circular geometry of diameter $D = 148\ mm$.

To test the rotary system, it was necessary to develop a support structure to hold and align the transmit arrays with the horn antenna center, while ensuring the focal distance $F_1 = 100\ mm$.

The model for this support structure was designed using CST and it is shown in Figure 38. This structure will be 3D printed using Polylactic Acid (PLA).

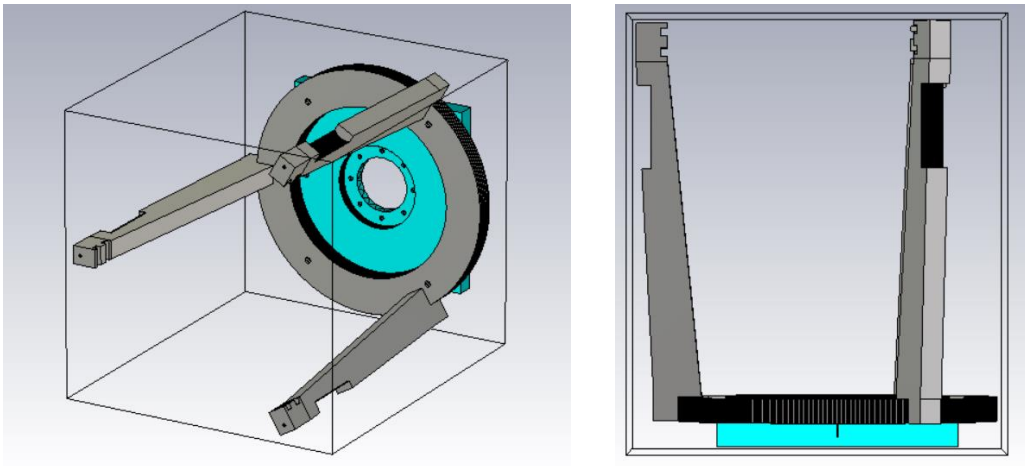

Figure 38 - Support structure model from CST (grey) and tower base (green)

The support structure has two components: the “body” has three “arms” that ensure the focal distance $F_1 = 100\,mm$ and it is fixed with M4 screws to the tower base where the Horn antennas are placed; the “hands” that hold the transmit arrays with a gap $d = 5\,mm$ between them. The “body” is separated from the “hands” to compensate the height difference between the two Horn antennas used in the measurements, one for $f_1 = 20\,GHz$ and another for $f_2 = 30\,GHz$. This way we do not have to change anything in the tower base. Also, if we want to test different gaps, we can simply replace the “hands”. These two components are attached using M2 screws and the “hole” in the “arms” allows the screw to get in. The support structure is made of PLA and it is used plastic screws to minimize the interference with the electromagnetic radiation.

As intended, the prototype is very lightweight: each transmit array weights approximately $115\,g$ and the support structure weights approximately $90\,g$, so the total weight of the rotary system with the support structure is only $320\,g$.

4 Conclusions

4.1 Main Achievements

The recent development of the small ground terminals market for mobile broadband access applications has created the need of beam steering antennas with high gain and large scanning range compatible with mass market production, that is, the solution should also be compact, lightweight and low-cost. Additionally, applications like SOTM use two distinct frequency bands and orthogonal circular polarization to minimize the interference between the up-link and the down-link. A dual-band polarization-insensitive rotary system is proposed in this work for small ground terminals in next generation mobile broadband access applications HTS and HAP in satellite Ka-Band (Rx: $20\ GHz$, Tx: $30\ GHz$). It is an extension of the Risley Prism concept, that allows pointing the beam at the same direction at two well-separated bands. The development of this antenna involved three different numerical analysis.

First, a PO/GO analysis was done using the KH3D_near program developed in house [28] to determine the main geometrical parameters using ideal phase distributions. Although this is a more simplistic analysis, it was very useful to gain an initial intuition of the system performance.

Second, the design of dual-band unit cells was performed using a full-wave analysis in the Frequency Domain of CST software [27]. These cells must satisfy a high amplitude transmission and a small phase discretization criteria, which is particularly difficult with dual-band cells: not only do these requirements must be satisfied simultaneously in two distinct bands but also the phase delay in one band is not independent from the phase delay in the other band. A set of 29 thin dual-band PD cells was designed with a transmission amplitude better than $-1\ dB$ at both bands and an average phase discretization step of $24.8°$ at $f_1 = 20\ GHz$ and $37.2°$ at $f_2 = 30\ GHz$ by varying the dimension, width and number of square metal rings. The geometry of these cells was inspired by the PG TA cells presented in [8], but their performance is better both in terms of transmission amplitude and phase discretization. One of the disadvantages of using PD cells is their thickness, however these cells are much thinner than other PD cells presented in previous works like [6].

Third, different Risley Prism implementations were compared using the previous cells and the final parameters were optimised using a full-wave analysis in the Time Domain of CST. Due to the complexity of these simulations, we were forced to resort to alternative methods to improve the time-efficiency of the simulations: an equivalent feed source instead of a Horn antenna to reduce the simulation volume and an equivalent dielectric description of the unit cells [26] before using the real cells. Initially, it was studied the conventional pair of phase distributions (16) and (17) used in previous works with rotary systems, however we have observed undesired prominent side lobes in the radiation pattern of Lens 2 that deteriorates the SLL, even when using ideal equivalent dielectric unit cells. To surpass this obstacle,

a new alternative pair of phase distributions was proposed by introducing a virtual focus and the results have improved.

A prototype is being built and measured using a radio-frequency anechoic chamber to validate the simulation results. The transmit arrays have a diameter $D = 148\,mm$, a thickness $t = 3.233\,mm$ and they are separated by an air gap $d = 5mm$. The real feed focal distance is $F_1 = 100\,mm$, which means $F/D \approx 0.8$ satisfying the low-profile requirement. The total weight of the transmit arrays with the support structure is approximately $320\,g$. The mass production of this antenna should be relatively easy and cost-effective, being appropriate for large markets with millions of users.

The new proposed implementation allows a scanning range $[-50°, 50°]$ with $Scan\ Loss > -3\ dB$ and $SLL < -10\ dB$ as required, unlike the conventional approach, as shown in Table 19. Additionally, the $Scan\ Loss$ at $f_1 = 20\ GHz$ and the SLL at $f_2 = 30\ GHz$ improve significantly when compared with the conventional approach using the equivalent dielectric cells. The simulated gain of the final design using the real cells is $G = 25.6\ dBi$ at $f_1 = 20.3\ GHz$ and $G = 27.7\ dBi$ at $f_2 = 29.9\ GHz$, satisfying the high gain requirement.

Table 19 - Simulated far-field results comparison between the two lenses systems with an equivalent dielectric description using the conventional phase distributions (16) and (17) and the new (21) and (23)

Pair of Phase Distributions	$\boldsymbol{D_{max}}$ $[\boldsymbol{dBi}]$ $(\boldsymbol{\theta_{RP}} = \mathbf{0°})$		$\boldsymbol{SLL}$ $[\boldsymbol{dB}]$ $(\boldsymbol{\theta_{RP}} = \mathbf{0°})$		$\boldsymbol{Scan\ Loss}$ $[\boldsymbol{dB}]$ $(\boldsymbol{\theta_{RP}} = \mathbf{50°})$		$\boldsymbol{SLL}$ $[\boldsymbol{dB}]$ $(\boldsymbol{\theta_{RP}} = \mathbf{50°})$	
	$\boldsymbol{f_1}$	$\boldsymbol{f_2}$	$\boldsymbol{f_1}$	$\boldsymbol{f_2}$	$\boldsymbol{f_1}$	$\boldsymbol{f_2}$	$\boldsymbol{f_1}$	$\boldsymbol{f_2}$
Conventional	26.0	28.1	-16.5	-12.9	-3.3	-3.1	-9.3	-10.8
Alternative	25.5	28.6	-14.8	-17.4	-2.8	-2.9	-11.1	-15.3

The antenna proposed in this work is the first dual-band polarization-insensitive beam scanning solution using a rotary system of transmit arrays. Unlike other mechanical steering mechanisms using in-plane translation, rotary systems keep a constant volume of operation without the complexity of electronic solutions. The rotary systems designed in previous works are implemented using single-band cells which means they cannot be used in applications like SOTM that require dual-band and polarization-insensitive antennas.

Considering the significant novel aspects achieved in this work regarding the present state of the art, an article is being prepared to be submitted in this field's IEEE journal.

4.2 Future Work

We have shown the performance of the two lenses rotary beam steering system can be improved by introducing a virtual focus. However, the limitations found using the conventional pair of phase distributions (16) and (17) have not been mentioned in previous works with similar systems, which gives rise to some questions that are still open, namely whether these limitations are solely due to the phase distributions or do they also depend on the unit cells geometry. To better understand this, one should compare the same phase distributions for different sets of unit cells. Also, the virtual focus could be possibly used to compensate the negative effects of reducing the real feed focus distance F_1, improving thus the F/D ratio of the total system.

As explained before, PR cells control the phase shift introduced by rotating the elements of the unit cell. Thus, dual-band PR cells require some mechanism that allows to control the phase shift in two separate bands by rotating elements, which is not trivial. However, it may be possible to extend the idea of using inductive elements like metal rings to design elements that affect primarily only one of the frequency bands. That way the dual-band cell rotation mechanism would be decomposed into two single-band rotation mechanisms. Unfortunately, due to time constraints, this idea was only pursued for a brief period and the results are shown in Appendix C. If it is proven successful, then it becomes possible to design dual-band beam steering solutions using TAs with PR cells that are usually thinner than PD cells. Nonetheless, these dual-band PR cells would not be fit for SOTM applications because the handover requires the ability to switch between orthogonal circular polarizations.

The creation of large broadband satellite internet constellations like SpaceX's Starlink or Amazon's Project Kuiper naturally requires the mass-production of ground terminal solutions that are compact and affordable for the projects to be viable. Nowadays, the proposed solutions are based in phased arrays that are electronically controlled to perform beam steering. Besides the extra costs associated with the complexity of the feeding network, the power consumption is extremely high ($100\,W$ for SpaceX for example). If this dual-band rotary system can be improved so that the gain is $30{\sim}35\,dBi$, this solution becomes an interesting low-cost and energy-efficient alternative to the electronic steering mechanisms.

Finally, the most promising topic to be explored in the future is the combination of a Radial Line Slot Antenna (RLSA) with one transmit array. The RLSA concept was introduced in 1985 by M. Ando for Ku-Band satellite applications [31], it consists of two parallel conductive plates filled with a dielectric and it is fed by a coaxial cable. The upper plate "leaks" radiation so that the equivalent surface currents radiate the desired far-field radiation pattern. This way, the external feed source can be removed, significantly reducing the total system height, while still being able to perform beam steering like a Risley Prism. In the literature, we can find RLSA solutions that radiate a plane wave without tilt for $\theta_{max} = 0°$ for dual-band applications [32], which would require two transmit arrays with phase distribution (20) that only have a tilting effect over the incident wave. For single-band applications, there are RLSA solutions that radiate a tilted wave [33], so it would only be required one additional transmit array with phase

distribution (20). To use specifically the Lens 2 proposed in this work, it would be necessary to design a RLSA that radiates a tilted spherical wave, instead of a plane wave.

Bibliography

[1] S. Ye, X. Liang, W. Wang, R. Jin, J. Geng, T. S. Bird, Y. J. Guo, “High-Gain Planar Antenna Arrays for Mobile Satellite Communications”, *IEEE Trans. Antennas Propag.*, vol. 54, no. 6, pp. 256-268, Dec. 2012.

[2] R. V. Gatti, L. Marcaccioli, E. Sbarra, R. Sorrentino, “Flat Array Antenna for Ku-Band Mobile Satellite Terminals”, *Proc. 5th European Conf. Antennas and Propag. (EuCAP)*, pp. 2618-2622, Rome, Italy, Apr. 2011.

[3] Y. J. Cheng, P. Chen, W. Hong, T. Djerafi, K. Wu, “Substrate Integrated-Waveguide Beamforming Networks and Multibeam Antenna Arrays for Low-Cost Satellite and Mobile Systems”, *IEEE Antennas and Propag. Mag.*, vol. 53, no. 6, pp. 18-30, Dec. 2011.

[4] L. A. Greda, A. Dreher, “Tx-Terminal Phased Array for Satellite Communication at Ka-Band”, in *Proc. 37th European Microwave Conf.*, pp. 266-269, Munich, Germany, Oct. 2007.

[5] Y. Sheng, L. Xianling, W. Wenzhi, J. Ronghong, G. Junping, T. S. Bird, Y. J. Guo, “High-Gain Planar Antenna Arrays for Mobile Satellite Communications”, *IEEE Antennas and Propag. Mag.*, vol. 54, no. 6, pp. 256-268, Dec. 2012.

[6] S. A. Matos, E. B. Lima, J. S. Silva, J. R. Costa, C. A. Fernandes, N. J. G. Fonseca, J. R. Mosig, “High Gain Dual-Band Beam-Steering Transmit Array for Satcom Terminals at Ka-Band”, *IEEE Trans. Antennas Propag.*, vol. 65, no. 7, pp. 3528-3539, Jul. 2017.

[7] N. Gagnon, A. Petosa, “Using Rotatable Planar Phase Shifting Surfaces to Steer a High-Gain Beam”, *IEEE Trans. Antennas Propag.*, vol. 61, no. 6, pp. 3086-3092, Jun. 2013.

[8] Q. Zeng, Z. Xue, W. Ren, W. Li, “Dual-Band Beam-Scanning Antenna Using Rotatable Planar Phase Gradient Transmit Arrays”, *IEEE Trans. Antennas Propag.*, vol. 68, no. 6, pp. 5021-5026, Jan. 2020.

[9] E. B. Lima, S. A. Matos, J. R. Costa, C. A. Fernandes, N. J. G. Fonsced, “Circular Polarization Wide-angle Beam Steering at Ka-band by In-plane Translation of a Plate Lens Antenna”, *IEEE Trans. Antennas Propag.*, vol. 63, no. 12, pp. 5443-5455, Oct. 2015.

[10] J. R. Costa, C. A. Fernandes, G. Godi, R. Sauleau, L. Le Coq, H. Legay, “Compact Ka-Band Lens Antennas for LEO Satellites”, *IEEE Trans. Antennas and Propag.*, vol. 56, pp. 1251-1258, May 2008.

[11] M. Tripodi, F. DiMarca, T. Cadili, C. Mollura, F. DiMaggio, M. Russo, “Ka Band Active Phased Array Antenna System for Satellite Communication on the Move Terminal”, *Proc. 5th European Conf. Antennas and Propag. (EuCAP)*, pp. 2628-2630, Rome, Italy, Apr. 2011.

[12] G. Bellaveglia, L. Marcellini, R. Lo Forti, A. Arcidiacono, B. Ray, “Low Profile Ku-Band VSAT Antenna System for High-Speed Trains”, *29th ESA Antenna Workshop on Multiple Beams and Reconfigurable Antennas,* ESA/ESTEC Noorwijk, Netherland, May 2007.

[13] D. Martinez-de-Rioja, E. Martinez-de-Rioja, J. A. Encinar, A. Pino, Y. Rodriguez-Vaqueiro, B. Gonzalez-Valdes, O. Rubiños, M. Arias, “Single and Dual Reflectarray Configurations for Multibeam Satellite Antennas in Ka-Band”, *13th European Conf. Antennas and Propag. (EuCAP)*, 2019.

[14] G. Wu, S. Qu, S. Yang, “Wide-Angle Beam-Scanning Reflectarray With Mechanical Steering”, *IEEE Trans. Antennas Propag.*, vol. 66, no. 1, pp. 172-181, Jan. 2018.

[15] A. A. Baba, R. M. Hashmi, K. P. Esselle, M. Attygalle, D. Borg, “A Millimeter-Wave Antenna System for Wideband 2-D Beam Steering”, *IEEE Trans. Antennas and Propag.*, vol. 68, no. 5, May 2020.

[16] T. Maruyama, K. Yamamori, Y. Kuwahara, “Design of Multibeam Dielectric Lens Antennas by Multiobjective Optimization”, *IEEE Trans. Antennas Propag.*, vol. 57, no. 1, pp. 57-63, Jan. 2009.

[17] X. Zhang, F. Yang, S. Xu, A. Aziz, M. Li, “Dual-Layer Transmitarray Antenna with High Transmission Efficiency”, *IEEE Trans. Antennas Propag.*, vol. 68, no. 8, pp. 6003-6012, Aug. 2020.

[18] P. Naseri, F. Khosravi, P. Mousavi, “Antenna-Filter-Antenna-Based Transmit-Array for Circular Polarization Application”, *IEEE Antennas and Wireless Propag. Letters*, vol. 16, pp. 1389-1392, 2017.

[19] P. Naseri, R. Mirzavand, P. Mousavi, “Dual-Band Circularly, Polarized Transmit-Array Unit-Cell At X and K Bands”, in *Proc. 10th Eur. Conf. Antennas Propag. (EuCAP)*, Davos, Switzerland, pp. 1-4, Apr. 2016.

[20] P. Naseri, S. A. Matos, J. R. Costa and C. A. Fernandes, “Phase-Delay Versus Phase-Rotation Cells for Circular Polatization Transmit Arrays – Application to Satellite Ka-Band Beam Steering”, *IEEE Trans. Antennas Propag.*, vol. 66, no. 3, pp. 1236-1247, Mar. 2015.

[21] A. Ebrahimi, W. Withayachumnankul, S. Al-Sarawi, D. Abbott, “Design of dual-band frequency selective surface dual band unit cells designs with miniaturized elements”, in *Proc. IEEE Int. Workshop Antenna Technol. (iWAT)*, Sydney, NSW, Australia, pp. 206-209, Mar. 2014.

[22] L. Zheng *et al.*, “Investigating the dual-passbands frequency selective surface with complementary structure”, in *Proc. PIERS*, Guangzhou, China, pp. 1494-1496, Aug. 2014.

[23] H. Hassani, J. S. Silva, S. Capdevila, M. García-Vigueras, J. R. Mosig, “Dual-Band Circularly Polarized Transmitarray Antenna for Satellite Communications at 20/30 GHz”, *IEEE Trans. Antennas Propag.*, vol. 67, no. 8, Aug. 2019.

[24] P. Naseri, S. A. Matos, J. R. Costa, C. A. Fernandes, N. J. G. Fonseca, “Dual-Band Dual Linear to Circular Polarization Converter in Transmission Mode – Application to K/Ka-Band Satellite Communications”, *IEEE Trans. Antennas Propag.*, vol. 66, no. 12, pp. 7128-7137, Dec. 2018.

[25] H. Hasani, J. S. Silva, J. R. Mosig, and M. García-Vigueras, “Dual-band 20/30 GHz circularly polarized transmitarray for SOTM applications”, in *Proc. 10th Eur. Conf. Antennas Propag. (EuCAP)*, Davos, Switzerland, pp. 1–3, Apr. 2016.

[26] S. A. Matos, J. R. Costa, P. Naseri, E. B. Lima, C. A. Fernandes, N. J. G. Fonseca, “Equivalent Dielectric Description of Transmit-arrays as an efficient and accurate method of analysis*”, 2020 14th European Conference on Antennas and Propagation*, DOI: 10.23919/EuCAP48036.2020.

[27] CST Microwave Studio – Computer Simulation Technology: http://www.cst.com, Oct. 2014.

[28] C. A. Fernandes, “KH3D_near – User’s manual”, Version 0.2h, Internal Report Instituto de Telecomunicações, Mar. 2018.

[29] R. F. Harrington, “Time-Harmonic Electromagnetic Fields”, Wiley-*IEEE Press*, 2001

[30] ABviewer: http://cadsofttools.com/products/abviewer/

[31] M. Ando, K. Sakurai, N. Goto, K. Arimura, Y. Ito, “A radial line slot antenna for 12 GHz satellite TV reception”, *IEEE Trans. Antennas and Propag.*, vol. AP-33, no. 12, pp. 1347-1353, Dec. 1985.

[32] J. Shao, F. Yang, R. Wang, Z. Xing, J. Yang, “A Dual Band and Dual Circular Polarization Radial Line Slot Antenna”, *2019 IEEE International Symposium on Antennas and Propagation and USNC-URSI Radio Science Meeting*, DOI: https://doi.org/10.1109/APUSNCURSINRSM.2019.8888488, Jul. 2019.

[33] M. Vera-Isasa, M. Sierra- Castañer, M. Sierra-Pérez, “Slot Antenna with a Tilted Beam for Satellite Reception”, *Microwave and Optical Technology Letters*, vol. 36, no. 5, Mar. 2003

Appendix A

Table 20 - Micro-parameters (in mm) for each dual-band PD cell

ID	a_1	a_2	a_3	l_1	l_2	l_3	$w_{in,1}$	$w_{in,2}$	$w_{in,3}$	w_{out}	$w_{a,1}$	$w_{a,2}$	$w_{a,3}$
0	2.70	2.65	2.60	2.10	1.85	1.85	0.1	0.1	0.1	0.1	0	0	0
1	2.60	2.65	2.60	2.10	1.85	1.35	0.1	0.1	0.1	0.1	0	0	0
2	2.60	2.60	2.60	2.05	1.80	1.80	0.1	0.1	0.1	0.1	0	0	0
3	2.55	2.55	2.60	2.10	1.80	1.80	0.3	0.15	0.3	0.1	0	0	0
4	2.50	2.40	2.60	2.00	1.75	1.45	0.1	0.1	0.1	0.1	0	0	0
5	2.50	2.40	2.60	2.00	1.45	1.55	0.1	0.1	0.1	0.1	0	0	0
6	2.50	2.40	2.60	2.00	1.65	1.45	0.1	0.1	0.1	0.1	0	0	0
7	2.45	2.40	2.55	2.05	1.05	1.60	0.2	0.2	0.1	0.1	0	0	0
8	2.40	2.30	2.50	2.00	1.55	1.50	0.2	0.2	0.1	0.1	0	0	0
9	2.40	2.20	2.45	2.00	1.00	1.70	0.2	0.2	0.1	0.1	0	0	0
10	2.40	2.35	2.50	1.95	1.20	1.65	0.2	0.2	0.1	0.1	0	0.1	0
11	2.70	2.55	2.45	2.10	1.85	1.50	0.1	0.1	0.1	0.1	0.1	0.1	0.1
12	2.70	2.45	2.45	2.10	1.85	1.50	0.1	0.1	0.1	0.1	0.1	0.1	0.1
13	2.65	2.25	2.40	2.05	1.80	1.80	0.1	0.1	0.1	0.1	0.1	0.1	0.1
14	2.50	2.20	2.00	2.05	1.75	1.60	0.1	0.1	0.1	0.1	0.1	0.1	0.1
15	2.45	2.15	2.00	2.00	1.75	1.60	0.1	0.1	0.1	0.1	0.1	0.1	0.1
16	2.60	2.60	2.60	1.95	1.60	1.20	0.7	0.5	0.1	0.1	0	0	0
17	2.60	2.50	2.60	1.95	1.40	1.20	0.7	0.5	0.1	0.1	0	0	0
18	2.50	2.45	2.60	2.10	1.85	1.85	0.1	0.1	0.1	0.1	0	0	0
19	2.55	2.40	2.55	2.10	1.85	1.80	0.1	0.1	0.1	0.1	0	0	0
20	2.50	2.20	2.55	2.10	1.80	1.75	0.1	0.1	0.1	0.1	0	0	0
21	2.50	2.20	2.50	2.10	1.75	1.75	0.1	0.1	0.1	0.1	0	0	0
22	2.45	2.20	2.60	2.05	1.75	1.55	0.1	0.1	0.1	0.1	0	0.1	0.1
23	2.45	2.20	2.55	2.05	1.75	1.55	0.1	0.1	0.1	0.1	0	0.1	0.1
24	2.40	2.15	2.50	2.00	1.75	1.55	0.1	0.1	0.1	0.1	0	0.1	0.1
25	2.40	2.15	2.45	2.00	1.75	1.00	0.1	0.1	0.1	0.1	0	0.1	0.1
26	2.40	2.10	2.35	2.00	1.70	1.45	0.1	0.1	0.1	0.1	0	0.1	0.1
27	2.50	2.10	2.45	2.00	1.65	1.35	0.1	0.1	0.1	0.1	0.1	0.1	0.1
28	2.40	2.05	2.45	2.00	1.65	1.35	0.1	0.1	0.1	0.1	0.1	0.1	0.1

Appendix B

Table 21 - Transmission amplitude, T, reflection amplitude, Γ, and wrapped transmission phase, ϕ, of every dual-band PD cell at $f_1 = 20\ GHz$ and $f_2 = 30\ GHz$

ID	$f_1 = 20\ GHz$			$f_2 = 30\ GHz$		
	$T\ [dB]$	$\Gamma\ [dB]$	ϕ [°]	$T[dB]$	$\Gamma\ [dB]$	ϕ[°]
0	-0.30	-41.61	286.6	-0.52	-13.36	5.4
1	-0.57	-13.92	320.5	-0.62	-12.43	33.5
2	-0.38	-14.64	356.8	-0.66	-9.44	94.1
3	-0.28	-17.22	20.5	-0.75	-8.51	133.5
4	-0.16	-20.90	53.9	-0.33	-13.60	160.6
5	-0.13	-25.80	61.0	-0.13	-27.00	226.2
6	-0.11	-32.90	65.1	-0.12	-42.60	199.2
7	-0.77	-8.27	91.7	-0.36	-13.22	246.3
8	-0.64	-8.92	117.3	-0.43	-12.20	266.2
9	-0.51	-9.80	130.2	-0.40	-19.17	286.6
10	-0.07	-22.45	158.7	-0.87	-9.46	331.5
11	-0.34	-12.89	193.1	-0.88	-9.49	57.8
12	-0.73	-8.48	221.0	-0.91	-9.33	57.9
13	-0.42	-10.85	251.2	-0.31	-14.41	123.8
14	-0.13	-17.70	295.5	-0.67	-9.65	182.4
15	-0.28	-12.87	305.7	-0.31	-14.83	210.2
16	-0.31	-18.36	352.4	-0.42	-11.12	257.4
17	-0.16	-27.31	29.2	-0.59	-9.93	302.6
18	-0.14	-35.20	48.3	-0.32	-29.70	10.6
19	-0.37	-12.05	72.2	-0.47	-15.52	20.7
20	-0.12	-19.47	94.8	-0.48	-11.99	71.8
21	-0.66	-8.80	110.0	-0.77	-8.91	92.8
22	-0.08	-44.30	161.2	-0.92	-7.88	157.8
23	-0.33	-12.21	174.1	-0.84	-8.37	158.2
24	-0.34	-11.75	188.9	-0.17	-30.56	185.9
25	-0.63	-9.05	199.3	-0.18	-42.86	199.0
26	-0.93	-7.31	206.3	-0.40	-13.17	240.6
27	-0.74	-8.39	267.2	-0.28	-16.33	264.3
28	-0.77	-8.30	274.9	-0.96	-8.82	307.4

Appendix C

The working principle of PR cells is achieving different phase shifts by rotating the metallic components by different angles. Dual-band Phase Shifting Surfaces require different phase distributions for each frequency. For this reason, dual-band PR cells are not very common when designing transmit arrays unless in some very special cases, such as polarization converters, where the phase distribution is spatially independent.

If the frequency quasi-independence property of inductive elements (rings, split rings, rectangular patches, etc) explained in section “Unit Cell Design” of Chapter 3 is extended to design dual-band PR cells with some elements affecting mainly one of the bands and the others having an impact over the other band, the dual-band obstacle may be surpassed: the up-link elements are rotated by the up-link angle and the down-link elements are rotated by the down-link angle.

While a 1-bit single-band phase description uses 2 configurations, 1-bit dual-band phase descriptions require 4 configurations as shown in Table 22.

Table 22 - Configurations of a 1-bit dual-band phase description

Configuration	$\boldsymbol{\phi_{f_1}}$ [°]	$\boldsymbol{\phi_{f_2}}$ [°]
A	0	0
B	0	180
C	180	0
D	180	180

PD cells present a symmetry regarding the $\hat{\boldsymbol{x}}$ and $\hat{\boldsymbol{y}}$ axes: the transmission coefficient for $\hat{\boldsymbol{x}}$-polarized incident waves is the same as the transmission coefficient for $\hat{\boldsymbol{y}}$-polarized incident waves. On the other hand, PR cells present an anti-symmetry regarding the $\hat{\boldsymbol{x}}$ and $\hat{\boldsymbol{y}}$ axes: the transmission coefficient for $\hat{\boldsymbol{x}}$-polarized incident waves is anti-symmetric to the transmission coefficient for $\hat{\boldsymbol{y}}$-polarized incident waves. This means, configuration D can be achieved using PR cells by rotating $90°$ configuration A, and the same is true for configurations B and C. Similarly, configuration B should be achieved by rotating $90°$ the f_2 elements of configuration A and the same is true for configurations C and D.

The most natural design resulting from this 1-bit dual-band phase description analysis involves two concentric elements that can rotate independently. It is interesting to point out that this is somewhat the rotation analogous of the dual-band PD cell proposed in Chapter 3: instead of varying the elements dimensions independently, we vary the elements rotation angle. The model for this PR design is shown in Figure 39, it has 3 layers, instead of 5: 2 split rings in each outer layer; 1 circular ring and 1 circular slot in the inner layer. The split rings with the smallest radius and the circular ring are the f_2 elements, while the split rings with the biggest radius and the circular slot are the f_1 elements. The dimensions and

widths of the elements in configurations A+D and B+C are not the same to improve the results. A valid unit cell must have $T < -1\ dB$ and a small phase error at both frequencies. Table 23 presents the results of model 1.

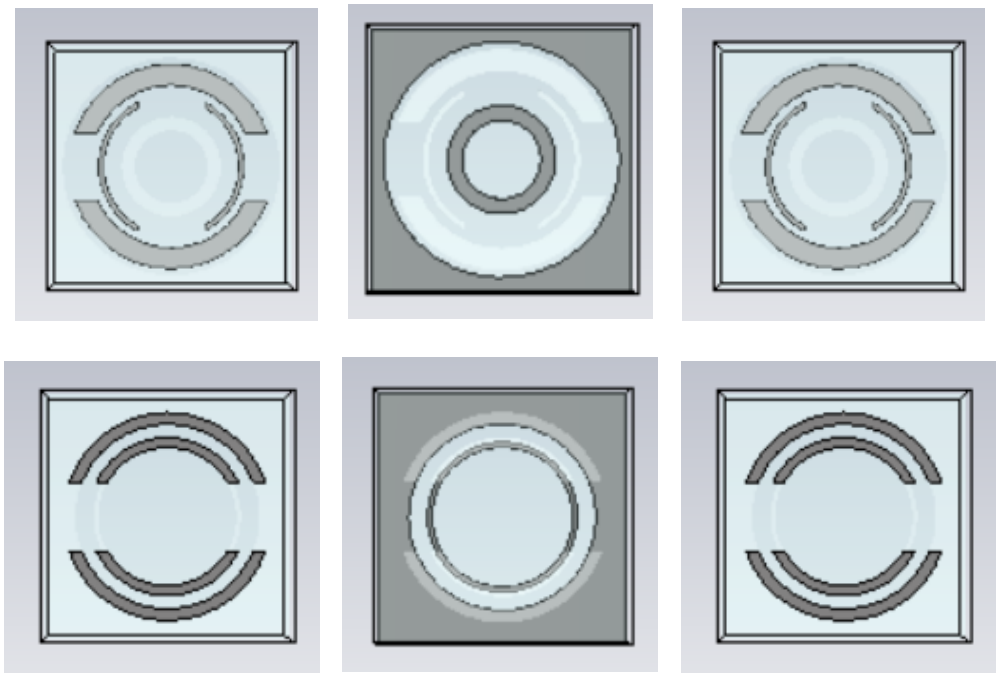

Figure 39 - PR dual-band unit cell's design: 3 metallic layers of configuration A (up); 3 metallic layers of configuration B (down). Besides the elements' dimensions and widths, the only difference is the 90° rotation of the smallest split rings

Table 23 - Dual-band PR 1-bit model results

Configuration	$f_1 = 20\ GHz$		$f_2 = 30\ GHz$	
	$T\ [dB]$	ϕ [°]	$T\ [dB]$	ϕ [°]
A	-0.2	0	-0.1	0
B	-0.9	0	-0.2	180
C	-2.3	112	-6.0	-49
D	0.0	97	-1.5	215

The cell design does not satisfy the transmission amplitude and phase criteria, so it is not a valid one.

Unfortunately, due to time constraints, it was only possible to begin to explore this idea and the dual-band 1-bit model does not satisfy the transmission amplitude and phase criteria. This Appendix is intended to present this cell design concept and the initial results, so that it may be possibly continued in the future.